UNIVERSITY OF TECHNOLOGY SYDNEY

DOCTORAL THESIS

Thiol-Mediated Synthesis of Transition Metal and Transition Metal Sulfide Nanowires

---

Author:
John SCOTT

Supervisor:
Prof. Milos TOTH

A thesis submitted in fulfillment of the requirements
for the degree of Doctor of Philosophy

in the

Materials and Technology for Energy Efficiency
School of Mathematical and Physical Sciences

February 26, 2019

Declaration of Authorship

I, John SCOTT, declare that this thesis titled, "Thiol-Mediated Synthesis of Transition Metal and Transition Metal Sulfide Nanowires" and the work presented in it are my own. I confirm that:

- This work was done wholly or mainly while in candidature for a research degree at this University.
- This research is supported by an Australian Government Research Training Program Scholarship.
- Where any part of this thesis has previously been submitted for a degree or any other qualification at this University or any other institution, this has been clearly stated.
- Where I have consulted the published work of others, this is always clearly attributed.
- Where I have quoted from the work of others, the source is always given. With the exception of such quotations, this thesis is entirely my own work.
- I have acknowledged all main sources of help.
- Where the thesis is based on work done by myself jointly with others, I have made clear exactly what was done by others and what I have contributed myself.

Signed: Production Note:
Signature removed prior to publication.

Date: Feburary 26, 2019

"Like sittin' on pins and needles, things fall apart, it's scientific"

David Byrne

University of Technology Sydney

Abstract

Faculty of Science
School of Mathematical and Physical Sciences

Doctor of Philosophy

Thiol-Mediated Synthesis of Transition Metal and Transition Metal Sulfide Nanowires

by John SCOTT

In this work, I discuss my investigation into the bottom-up synthesis of metal and metal sulfide nanowires supported by a capping reagent. Capping reagents are chemical species that alter the crystal growth kinetics. Through their deployment, the scalable synthesis of low-symmetry nanocrystals (such as nanowires) can be achieved. Here, I show the synthesis of metal (Co, Ni) and binary metal sulfide (Co_9S_8, Ni_3S_2) nanowires by heat-up thermolysis of simple molecular precursors. Detailed analysis of the precursors and the reaction steps leading to nanowire growth is provided. The unusual reaction conditions enable new insights through *in situ* characterisation using thermogravimetry with evolved gas analysis and field-emission scanning electron microscopy. This provides new understanding of the precursor conversion rates and identification of active chemical species that support 1D growth. To confirm the role ligand fragments play in shaping the crystal growth kinetics, substitution of the precursors was performed. It is further shown that anisotropic growth can selectively be tuned by deployment of the capping ligand species. Based on these new understandings, the high-yield synthesis of technologically important Co_9S_8 nanowires by chemical vapour deposition is presented.

Acknowledgements

I would like to express my deepest thanks to Professor Milos Toth. I am sincerely grateful for the knowledge and support you have provided during this work. I would also like to thank Associate Professor Charlene Lobo and Professor Igor Aharonovich. Each day I am part of a wonderful environment to learn and explore.

My sincerest thanks to Mr. Geoff McCredie, Mrs. Katie McBean and Mr. Mark Berkahn for your support over the course of my project. To Associate Professor Andrew McDonagh and Alexander Angeloski who have provided exceptional guidance and help with analysis of the precursor compounds and editing of manuscripts. To my fellow students, I would like to thank all of you for your friendship. A special thank you to Toby Shanley, Chris Elbadawi, Alexander Angeloski, Toan Tran and Noah Mendelson for allowing me to collaborate with you on your research projects. James Bishop and Aiden Martin for assistance with time-dependent SEM characterisation during nanowire growth. To James Bishop, Aiden Martin, Chris Elbadawi and Mehran Kianinia for all the work you have done in setting up the lab.

A special thanks to my family and my love Vanessa for the support you have showed me in my life. Lastly and most of all I would like to thank my mum Ellie. Your support, encouragement and love made this work possible.

Publications

Contributing Publications

- Solventless synthesis of Co_9S_8, Ni_3S_2, Co and Ni nanowires, **J. A. Scott**, A. Angeloski, I. Aharonovich, C. J. Lobo, A. McDonagh and M. Toth, *Nanoscale*, 2018 (submitted)
- Versatile method for template-free synthesis of single crystalline metal and metal alloy nanowires, **J. A. Scott**, D. Totonjian, A. A. Martin, T. T. Tran, J. Fang, M. Toth, A. M. McDonagh, I. Aharonovich, C. J. Lobo, *Nanoscale*, 2016, 8(5), 2804-2810.

Non-contributing Publications

- Engineering and Tuning of Quantum Emitters in Few-Layer Hexagonal Boron Nitride, N. Mendelson, Z.Q. Xu, T. T. Tran, M. Kianinia, **J. A. Scott**, C. Bradac, I. Aharonovich and M. Toth, *ACS Nano*, 2019
- Conversion of single crystals of a nickel(II) dithiocarbamate complex to nickel sulfide crystals, A. Angeloski, M. Cortie, **J. A. Scott**, D. Bordin, A. M. McDonagh, *Inorganica Chimica Acta*, 2019, 487, 228-233
- From Lead (II) Dithiocarbamate Precursors to a Fast Response PbS Positive Temperature Coefficient Thermistor, A. Angeloski, A. R. Gentle, **J. A. Scott**, M. B. Cortie, J. M. Hook, M. T. Westerhausen, M. Bhadbhade, A. T. Baker, A. M. McDonagh, *Inorganic Chemistry*, 2018, 57(4), 2123-2140.
- Electron beam microscope with improved imaging gas and method of use, T. Shanley, **J. A. Scott**, and M. Toth, U.S. Patent 9,633,816 (2017)
- Room-Temperature Single-Photon Emission from Oxidized Tungsten Disulfide Multilayers, T. T. Tran, S. Choi, **J. A. Scott**, Z.Q. Xu, C. Zheng, G. Seniutinas, A. Bendavid, M. S. Fuhrer, M. Toth, I. Aharonovich, *Advanced Optical Materials*, 2017, 5(5).
- Role of Gas Molecule Complexity in Environmental Electron Microscopy and Photoelectron Yield Spectroscopy, T. W. Shanley, F. Bonnie, **J. A. Scott**, M. Toth, *ACS Applied Materials & Interfaces*, 2016, 8(40), 21305-27310.

- Electron beam directed etching of hexagonal boron nitride, C. Elbadawi, T. T. Tran, M. Kolíbal, T. Šikola, **J. A. Scott**, Q. Cai, L. H. Li, T. Taniguchi, K. Watanabe, M. Toth, I. Aharonovich and C. Lobo, *Nanoscale*, 2016, 8(36), 16182-16186.

Contents

List of Figures

List of Tables

List of Abbreviations

TEM	**T**ransmission **E**lectron **M**icroscope
EDS	**E**nergy **D**ispersive (X-ray) **S**pectroscopy
NMR	**N**uclear **M**agnetic **R**esonance
SEM	**S**canning **E**lectron **M**icroscope
FESEM	**F**ield **E**mission **S**canning **E**lectron **M**icroscope
FTIR	**F**ourier-**T**ransform **I**nfra**R**ed (spectroscopy)
SAED	**S**elected **A**rea **E**lectron **D**iffraction
XRD	**X**-**R**ay **D**iffraction
UV-vis	**U**ltraviolet **V**isible **S**pectroscopy
DTG	**D**ifferential **T**hermal **G**ravimetric analysis

Dedicated to my mum…

Chapter 1

Introduction

1.1 Motivation

Technological demands require revolutionized approaches to nanofabrication. The integration of nanostructures into technology is not dependent on the properties they demonstrate but the challenges that exist in their synthesis and assembly. Nanofabrication methods must achieve the scalable formation of perfectly identical nanostructures assembled into predetermined locations with desired orientations. Bottom-up synthesis techniques including approaches that utilize capping reagents are able to meet many of these challenges. Capping reagents are chemical impurities that shape the energy landscape in which nanocrystals form, allowing control over critical features including size, shape and composition. However, much remains unknown about the forces and species that influence crystal growth. Current methods remain as a trial and error process with little predictive capacity. Further, only very basic shapes are able to be reproducibly grown. Low-symmetry structures such as one-dimensional materials offer greater potential in many applications, however present further complications for nanofabrication techniques. Mechanistic studies have been invaluable to furthering our understanding. Here, I examine the fundamental role precursor chemistry plays in anisotropic growth of nanocrystals on a number of relevant materials systems. It is my hope that through the new insights presented here, advancements can be made in the deployment of 1D materials into future technologies.

1.2 Nanomaterials

The unique behaviour of solid materials on the nanometer size scale presents unparalleled opportunity to meet many of the greatest challenges facing humanity. The potentials extend far beyond the miniaturization of existing technologies. Nanomaterials offer new and efficient means of harnessing energy from a variety of sustainable sources, early detection and treatment of disease and new technologies operating with greater speed and efficiency. Materials with at least 1-dimension between 1 - 100 nm are defined as *nanomaterials* (Figure 1.1).[56,244,112] Materials on this size scale: (1) show novel and size dependent properties, (2) interact with fundamental biological processes that occur at the cellular level and (3) have an extraordinarily high surface area-to-volume ratio.

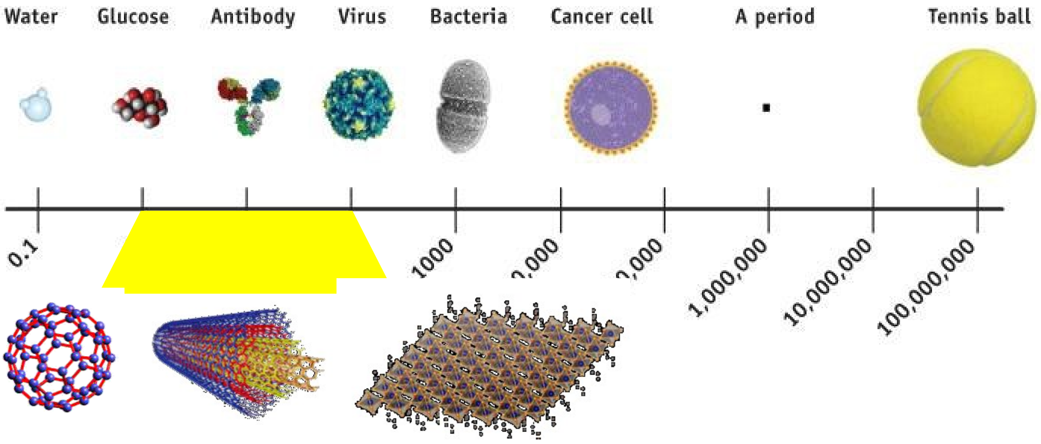

FIGURE 1.1: Illustration highlighting the size of nanomaterials on a size scale from a water molecule to a tennis ball.[[174]]

Confinement effects that occur on reduced length scales provide the most powerful means to manipulate the electronic, optical, magnetic and thermoelectric properties of a solid material.[246] The size dependent behaviour of nanostructures enables precise engineering of a material's properties (materials-by-design) to form new technologies based on manipulation of newly realized phenomenon. Secondly, dynamic interactions with biological entities (proteins, DNA, membranes, organelles, cells, tissues and organs) can be modulated by programming nanomaterials, the result of which holds great promise in delivering effective diagnostic, therapeutic, theragnostic and regenerative systems and/or devices.[23] Lastly, much interest in materials is only surface deep (examples include catalysis, hydrogen storage, energy storage and conversion, water desalination, drug delivery and beyond), thus it is self-evident that the higher available surface area (for a given volume), the greater the efficiency and performance. The surface area per unit volume of nanostructures is astounding when compared with its bulk and can be visualized by the illustration in Figure 1.2. The surface area of a single solid cube with dimensions 1 × 1 × 1 cm is 6 cm^2, whilst if made up of 1 × 1 × 1 nm cubes the surface area is 7 orders of magnitude greater. In summary, nanomaterials promise to revolutionize technology across every field, enabling engineering of a material's properties, the manipulation of quantum effects and the increase of a material's surface area over orders of magnitude.

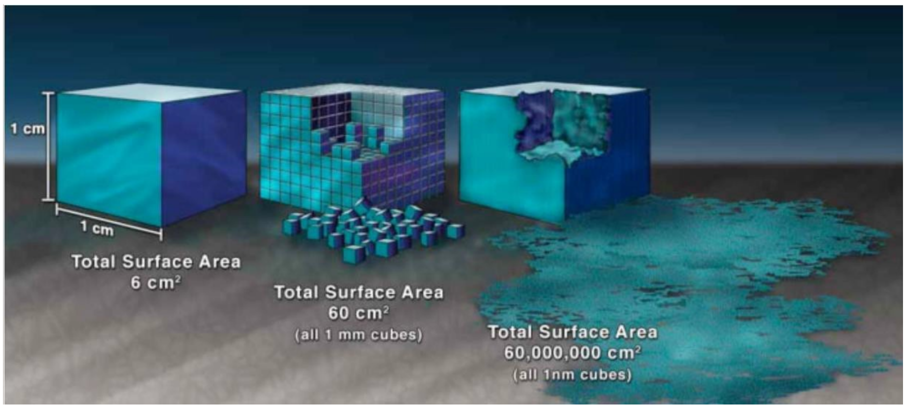

FIGURE 1.2: Illustration demonstrating increased surface area of nanostructured materials versus bulk.[94]

1.2.1 One-Dimensional Materials

Nanostructured materials are broadly classified by the number of dimensions contained to the 1 - 100 nm size scale. These include 0D, 1D and 2D materials (Figure 1.3a). Interesting and unique phenomenon arise in materials with reduced dimensionality. The physical properties of a material are altered through confinement effects of electrons, electromagnetic excitations or photons and phonons.[92] Quantization of electron energy levels due to constraint of their wave-functions occurs when the dimensions of a material are sufficiently small, defined by the Fermi wavelength or excitonic Bohr radius.[92] Lateral confinement of electron wave-functions while allowing free propagation along one dimension traditionally define 1D materials.[118] Figures 1.3b and c illustrate the discrete energy levels that occur in nanocrystals (compared with bulk and individual atoms) and how confinement effects in 2D, 1D and 0D materials shape the density of states. The illustration elegantly highlights the origin of novel properties on different size scales with different dimensions. The density of states can be thought of as the electron capacity of an energy level and the available energy levels in a system. Size dependent behavior can be exploited in 1D materials as the diameter is reduced beyond the phonon and electron mean free path, the Debye length, critical size of the magnetic domain, exciton diffusion length and others.[116,3,132]

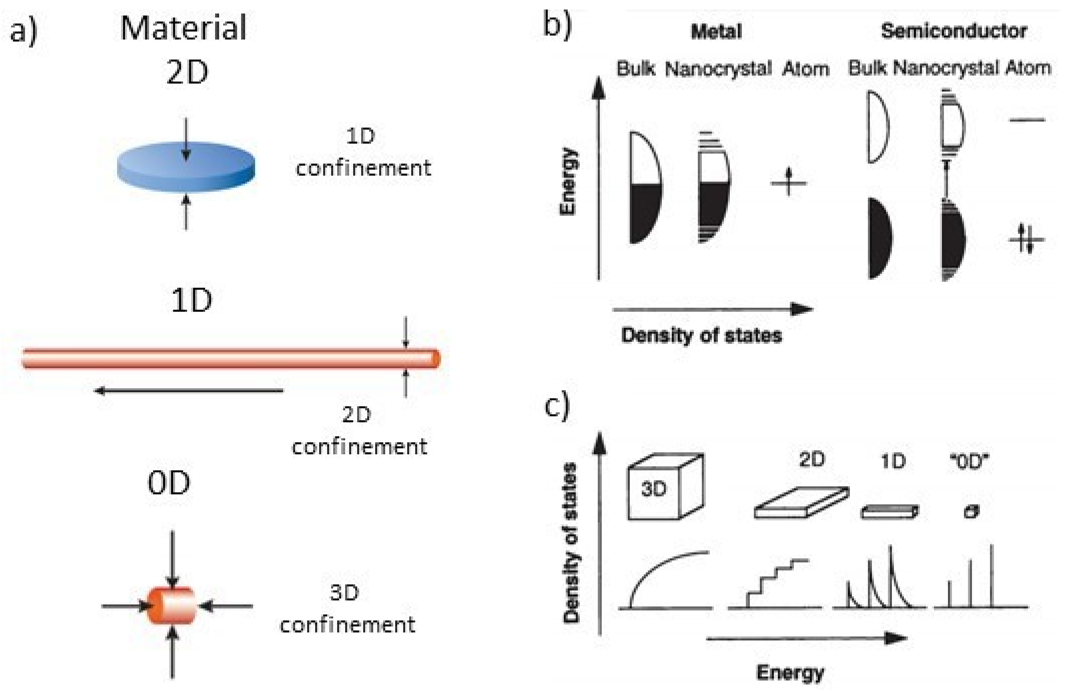

FIGURE 1.3: a) Schematic illustrating 2D, 1D and 0D materials.[[92]] Density of states for energy levels in metals and semiconductors for b) different size scales and c) dimensionality.[[3]]

Common shapes of 0D, 1D and 2D materials are shown in Figure 1.4. The distinct feature of 1D materials is that electron confinement occurs in 2-dimensions, or lateral confinement, while allowing electrons to propagate freely along the third dimension, which can span hundreds of nanometers to millimeters in length.[112,244,256] Structures with dimensions on the two length scales bridge the nanoscopic and macroscopic world. One-dimensional materials represent the smallest dimension for the efficient transport of particle and wave phenomenon including electrons, holes, excitons, ions, spin waves, surface polariton plasmons and phonons (to name a few).[24,153] These abilities fulfill many requirements as interconnects in electrically or optically driven devices. In addition 1D materials may also serve as active components within integrated devices, simultaneously providing two of the most important functions.[216] Applications of 1D materials can therefore be based on their shape, properties or a combination of both.

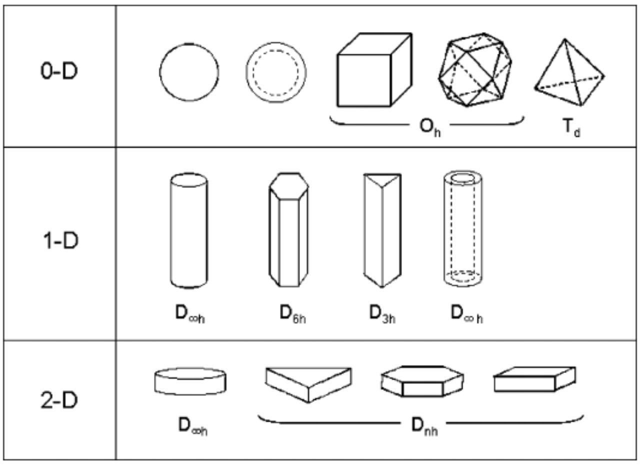

FIGURE 1.4: Common nanocrystal morphology of 0D, 1D and 2D materials.[[98]]

A general overview of many of the advantages that 1D materials provide for diverse applications - ranging from advanced energy storage and conversion to catalysis, electronics, sensing, optoelectronics and beyond - is discussed here.

Understanding the relationship between shape anisotropy and magnetism has uncovered exciting potential and the merging of electronics, photonics and magnetics which will impact future technologies. One-dimensional materials carry much promise in magnetic and spintronic based devices. The shape anisotropy of nanowires is well suited for storing digital information in both traditional hard disk drives and newly conceptualized memory devices including magnetic random access memory (MRAM) and racetrack memory (Figure 1.5a), based on control over individual magnetic domains in nanowires.[163,164,73,195,165]

Promising biomedical applications of 1D materials in therapeutics through drug delivery and magnetic hypothermia as well as diagnostics as MRI contrast agents and sensing has garnered much attention.[195] Figure 1.5b highlights one example in which a coupled nanoparticle-nanowire system is used as a multiplex DNA sensor based on surface enhanced Raman scattering of the hybrid system.[100]

The large surface area-to-volume ratio of nanowires is highly desirable

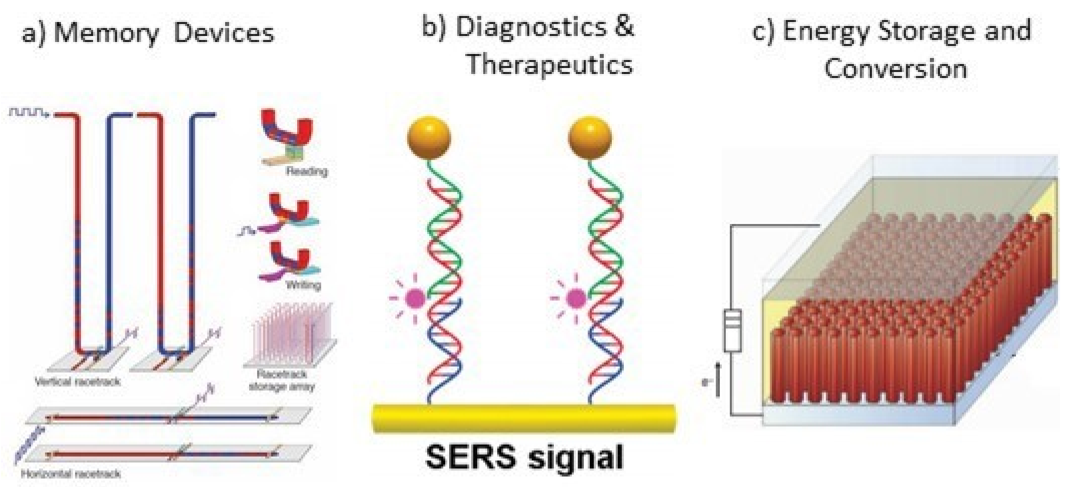

FIGURE 1.5: Nanowire-based devices including a) racetrack memory,[164] b) coupled nanowire-nanoparticle DNA sensor,[100] and c) nanowire dye-sensitized solar cell.[117]

for applications as active materials in catalysis and detectors as well as energy conversion and storage devices (Figure 1.5c). The relatively high concentration of specific, catalytically active, surface facets give nanowires enhanced selectivity and efficiency compared to nanoparticle catalysts.[37] Similarly these properties are important in highly sensitive and selective detectors for biological and chemical species as well as active components in gas-detectors.[39,233,230] In advanced energy storage and conversion applications, 1D materials have numerous benefits over competing morphologies. As summarized by Mai *et al.*[138] these include:

- efficient charge transport pathway
- short ion diffusion lengths
- high contact surface area between the electrode and electrolyte
- volume expansion tolerance
- can be synthesized directly on a metal or carbon surface in uniform arrays
- can be used to support complex and multifunctional architectures
- advantageous for *in situ* studies

Numerous electronic and optoelectronic applications exist including field effect transistors, photodetectors, waveguides, nonlinear optical converters, LEDs and microcavity lasers.[256] Nanowire field effect transistors enable gate-all-round topography (Figure 1.6) which can lead to improved efficiency and greater chip density.[87] Nanowires have been demonstrated to act as efficient waveguides through two-dimensional confinement showing low loss and tunable longitudinal surface plasmon resonance by engineering the aspect ratio.[183,46,58,129] The energy separation between the absorption and emission maxima (Stokes shift) and emission of linearly polarized light has also been demonstrated in elongated structures.[197]

FIGURE 1.6: Wrap-gate nanowire field-effect transistor.[203]

Nanowires offer greater versatility in their fabrication that is not available in planar form. The different material systems that have been synthesized in 1D form far exceeds those available in wafer form including heterostructures.[12,87] Fundamental challenges exist to the integration of compound semiconductors into Si-based technologies.[126] Nanowire heterostructures push beyond limitations of planar geometries including tolerance for lattice, thermal and polarity mismatches which can be accommodated by the narrow profile and the small surface area of side-wall facets.[55,139,92,219]

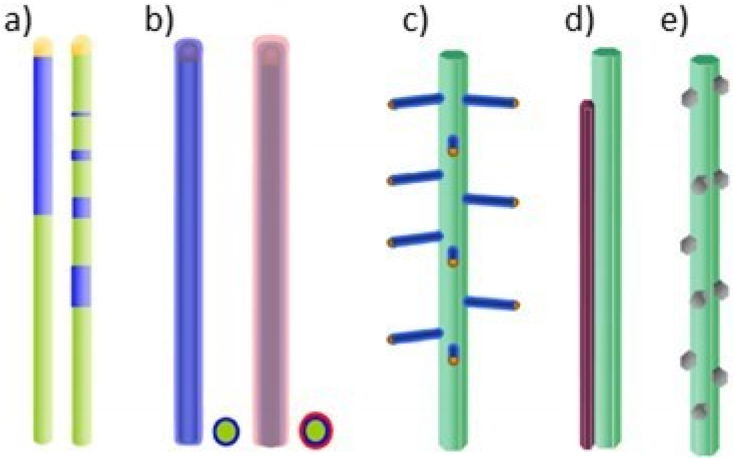

FIGURE 1.7: Examples of 1D heterostructure including: a) axial, b) radial, c) branched, d) aligned and e) integrated 0D and 1D structures.[12]

Nanowire heterostructures greatly expand the physical properties offering tremendous opportunity for nanoscale devices. The common integration of material systems in heterostructured nanowires is layered structures known as axial heterostructure and core/shell structures known as radial heterostructures (Figures 1.7a and b). This provides two degrees of freedom for the modulation of composition on the nanoscale. The longitudinal axis can serve in the extraction of charge carriers and photons to enable device integration.[92] In optoelectronic applications this has been used as a gain/absorption medium, optical cavity, and injection/extraction structure. Nanowires with a semiconducting core and metal shell act as optical antennas, significantly enhancing coupling between light and material. Core/shell nanowires have been shown to improve carrier mobility by isolating carriers from surface defects and impurities and enabling tuning of the carrier gas density.[92] As mentioned, the small cross-sectional area of nanowires enables elastic strain relaxation, reducing structural defects that are prevalent in lattice-mismatched materials. The development of fabrication techniques has seen axial heterostructured based devices for logic and sensing including nanowire resonant tunneling diodes (RTDs), nanowire single-electron transistors, tunneling field-effect transistors (TFET) and *p*-*n* diodes, as well as photodetectors, light-emitting diodes, lasers and photovoltaics.[16,210,187,17,92] The other examples of nanowire heterostructures shown in Figure 1.7 include branched, aligned and integrated 0D and 1D structures.

The novel and highly exciting physical properties of 1D materials make them promising candidates for new technologies. Benefits of 1D materials extend well beyond the convenience of their shape. They demonstrate unique behavior and link the quantum world with the macro. As such, much effort is dedicated to understanding these systems. Fundamental to this are nanofabrication strategies which enable the scalable formation of high-quality and homogeneous 1D nanocrystals.

1.2.2 Synthesis of Nanostructures

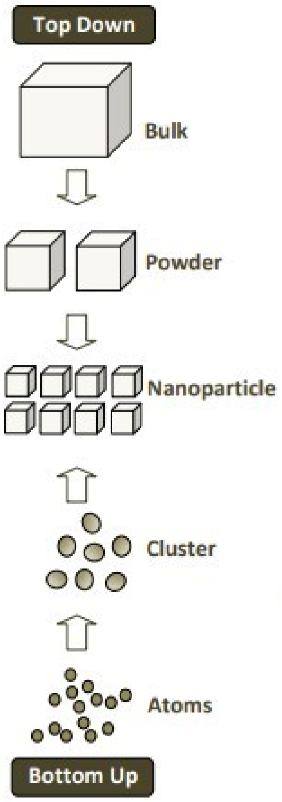

FIGURE 1.8: Schematic contrasting top-down and bottom-up paradigms.[179]

The manipulation of matter at the nanoscopic scale is fundamental to nanotechnology. The size-dependent properties of nanostructured materials place enormous demand on fabrication techniques, whereby variances of a single atom can change the properties of nanostructures.[135,197,166] Key areas of importance for large-scale, commercial implementation include scalable production of nanocrystals with identical size, shape and composition. Methods that also allow the controlled assembly of nanocrystals into predetermined locations with a given orientation are important for integration into hierarchical structures. While post-growth processing techniques may meet these challenges, fewer processing steps are intrinsically favored. Strategies to forming nanomaterials are broadly divided between bottom-up and top-down approaches (Figure 1.8). The processes involved in the creation of the nanostructure distinguish the two paradigms. Top-down approaches start from larger materials and selectively remove material until the desired morphology is achieved. By contrast bottom-up approaches utilize intrinsic forces of chemical species to form larger structures.

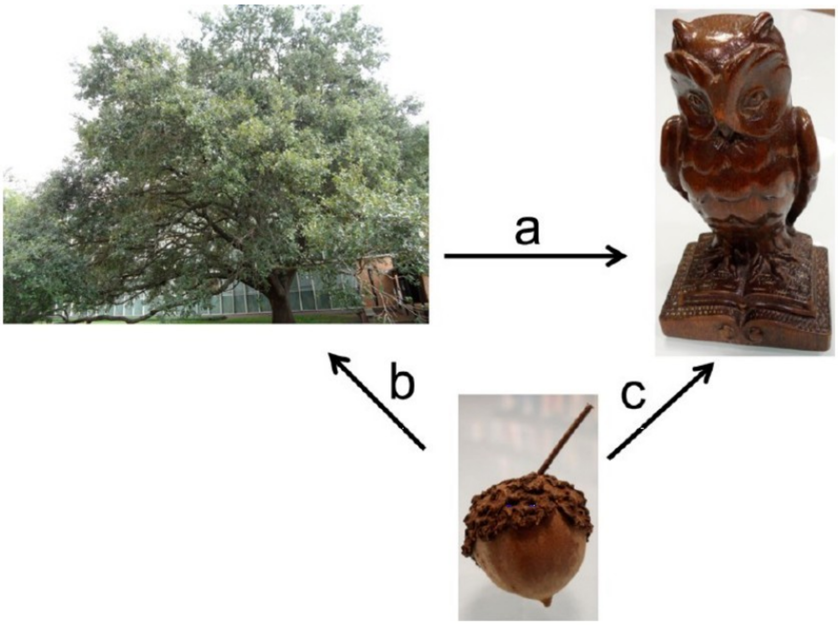

FIGURE 1.9: Acorn analogy of a) top-down and (b - c) bottom-up formation approaches.[[218]]

What characterizes top-down fabrication techniques is the removal of extraneous material using macroscopic tools to produce nanoscale structures of defined morphology. This is illustrated in Figure 1.9 in the path denoted by *a*; here a wooden owl statue is carved from the tree. Current fabrication methods for microelectronic systems in the semiconductor industry fall under this paradigm. Fabrication occurs in a serial process using beams of ion, electron, photon or atoms to sculpt matter from the macroscopic scale to nanoscopic.[160] Major advantages of top-down techniques include the complexity of shapes that can be formed and macroscale ordering of nanostructured materials. However as device features are scaled down into the sub-100-nm regime, technological and fundamental challenges exist that have shifted emphasis to bottom-up methods.[135,87]

Bottom-up methods of nanomaterial synthesis offer exciting potential to meet the challenges of resolution and scalability, hindering current manufacturing processes. Under this paradigm the formation of nanocrystals occur spontaneously from basic building blocks by self-governing forces.[272] This can be illustrated by the formation of a tree, denoted by the path *b* (or path *c* to form a statue) from the addition of smaller components, which is signified by the growth of an acorn. Atomic level control over material composition and structure is able to be achieved, far beyond the resolution limits of top-down processes. This has been exploited through *in situ* doping during nanocrystal synthesis, leading to novel material systems not achievable by top-down processes.[132] The major disadvantages of the techniques is that they are unable to achieve macroscopic ordering which is routine in top-down processes and that they are limited to basic shapes. Common bottom-up fabrication methods include atomic-layer deposition, sol-gel nanofabrication, molecular self-assembly, hot-injection and heat-up coprecipitation and vapor-liquid-solid growth.[15]

Undoubtedly future nanofabrication techniques will utilize forces operating over several length scales to achieve the growth of ordered structures of complex shapes with atomic level control.[160] Deeper understanding of the formation process of nanocrystals is fundamental to their deployment as it will not only enable the scalable fabrication of perfectly identical nanocrystals but will also enable new physics with increased complexity as synthesis approaches are pushed to their limits.

1.2.3 Strategies for the Formation of 1D Materials

Numerous strategies have been employed in the formation of anisotropic nanocrystals including 1D materials. A schematic outlining the various techniques is shown in Figure 1.10. To summarize, 1D growth can be achieved: (1) in intrinsically anisotropic crystal systems (Figure 1.10a), (2) through the use of a foreign catalyst particle (Figure 1.10b), (3) through the use of templates (Figure 1.10c), (4) through facet selective adhesion of ligand species (Figure 1.10d), (5) through orientated attachment of nanoparticles (Figure 1.10e) and by reducing the size of a larger structure (Figure 1.10f).

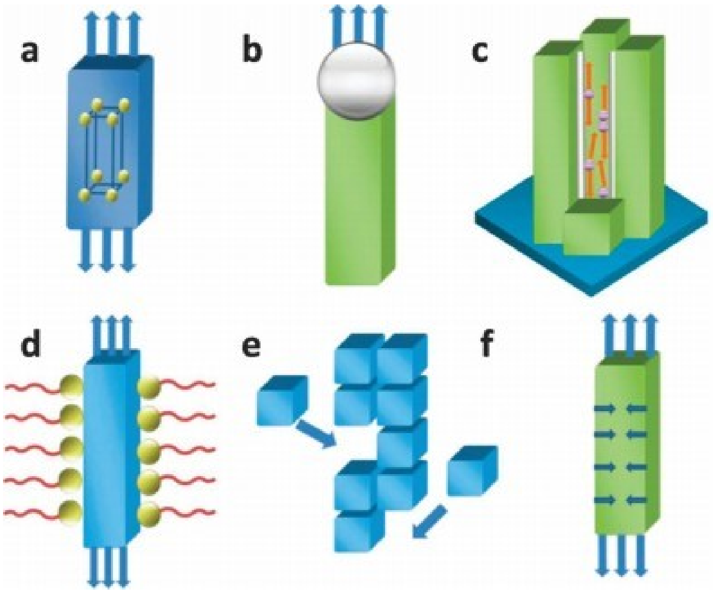

FIGURE 1.10: Schematic illustrating strategies for the formation of 1D materials. One-dimensional growth can occur a) as an intrinsic property of a crystal system, b) through the VLS mechanism, c) hard templating, d) capping reagent supported growth, e) oriented attachment of nanoparticles and f) by top-down techniques.[132]

Highly anisotropic bonding can be supported by the crystal habit. Examples in which 1D growth naturally occurs in crystals include poly(sulfur nitride), $LiMo_3Se_3$, Se and Te alloys and others.[202,199,141,244] These material systems all have a crystal structure composed of chain-like building blocks. Synthesis was demonstrated from both solution phase and vapor phase reactants to produce both semiconducting and metallic 1D materials including single-crystalline structures. Symmetry breaking growth may also be achieved by the use of a catalyst nanoparticle. The mechanism is known as the vapor-liquid-solid (VLS) mechanism, and analogues thereof (solution-liquid-solid, etc).[227] The use of templates as a scaffold has also proven to be a successful method of directing 1D growth of various materials. Templates may consist of step-edges on a solid surface, channels within a porous material, micelles or self-assembled mesoscale structures from organic surfactants, biological macromolecules or seed nanocrystals.[244] Template directed synthesis is generally considered a high throughput method that enables *in situ* doping, however commonly involves numerous steps, produces material of poor crystal quality and through the template removal may lead to surface roughening, damage or unintentional doping.[32] Capping reagents synthesis uses chemical species including surfactants, polymers and ions to modify crystal growth kinetics to support anisotropic growth.[206] The oriented attachment of 0D nanocrystals along specific surfaces is another means of achieving the formation of 1D materials which utilize localized forces.[34] Finally the selective removal of materials from a larger structure can be deployed as a means to form 1D materials. Examples include the formation of single-crystal Si nanowires by chemical etching.[265]

The focus of this study is nanowire growth supported by capping reagents. Capping reagent directed synthesis has proven to be one of the most powerful methods for the scalable formation of monodispersed 1D materials, with fine control over aspect ratio, crystal phase and composition. Further, it has been demonstrated on a broad range of material systems with different crystal structures and requires few processing steps. The VLS growth mechanism is arguably the most successful method to date especially in the synthesis of semiconductor nanowires. However, numerous hurdles exist which prevent its deployment, and will be discussed further in the next section.

1.2.4 VLS Growth

One of the most powerful techniques and most commonly used synthesis methods for carbon nanotubes and single crystalline nanowires of various functional inorganic materials is the vapor-liquid-solid (VLS) mechanism and analogues thereof.[271,89] Advantages of the mechanism include the formation of high quality, single-crystals in well-defined arrays (Figure 1.11a). In addition, it allows for controlled doping of nanowires and formation of nanowire heterostructures with close to atomically sharp interfaces.[228,239] Under this method, reactive species are supplied to the nanowire growth front via a liquid seed particle.[227,243] The metal seed particle offers incredible control over nanowire composition, morphology and crystallinity.[271]

Numerous shortcomings exist which have limited wider deployment of this technique including contamination by the metal catalyst. Diffusion of the catalyst into the nanowire is detrimental to performance and methods of removal typically involve damaging etchants. Examples of this include the widely used gold catalyst which has a high diffusivity in Si and acts as a deep level acceptor, which in addition to hurting performance creates heterogeneities between nanowires in a single growth.[87] *In situ* TEM studies show that diffusion of the Au catalyst particle determines the length, shape and sidewall properties of the Si nanowires, concluding that smooth and arbitrarily long nanowires cannot be grown without eliminating Au migration.[78] The high growth temperatures (> 600 °C) required for nanowire growth in

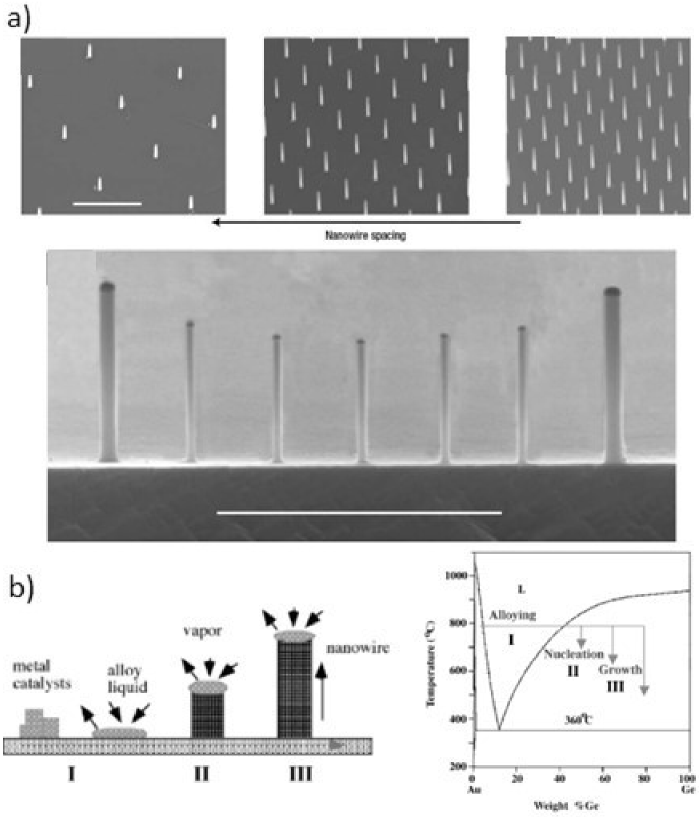

FIGURE 1.11: a) Ordered arrays of GaP nanowires with different spacings.[12] b) Schematic illustrating different stages of Ge nanowire growth from a Au metal seed and the associated phase diagrams.[243]

a number of material systems is typically incompatible with integration into hierarchical structures, thus placing a limit on the application range.[271] Also fundamental limitations of the mechanism including the formation of a low-melting eutectic droplet have prevented the growth of numerous material systems by this technique including metals (Figure 1.11b).[227,35,232]

1.3 Overview of Thesis

In this work I detail my investigation into the capping reagent supported synthesis of Co, Ni, Co_9S_8 and Ni_3S_2 nanowires using thiol containing precursor species. In Chapter 2 I provide a brief background on the applications and nanostructured synthesis methods of these material systems. In Chapter 3 I review nanocrystal formation by coprecipitation methods with particular attention to symmetry breaking synthesis using capping reagents. The thermodynamic forces and kinetic barriers that shape nanocrystal morphology are discussed as well as the current status of the field of nanocrystal synthesis. I then discuss the different home-built reactor systems I have used and how they enabled new insight into nanowire growth.

My results sections are broken down into two chapters. In Chapter 4 I discuss nanowire synthesis by solventless thermolysis, a variant of coprecipitation methods, using simple-molecular precursors based on the amino acid cysteine. The controlled growth of metal or metal sulfide phase nanowires is demonstrated by varying the mole ratio of precursor species (metal(II/III) bis-cysteinate to metal(II) acetate). Mechanistic understanding of the process is achieved by detailed characterization of the precursors and the reaction pathway that leads to 1D growth. This is achieved through *in situ* characterization during thermal decomposition. The characterization techniques employed to study thermolysis behavior are thermogravimetric analysis with gas chromatography-mass spectrometry (TGA-GC-MS) and field-emission scanning electron microscopy (FESEM). Growth anisotropy is attributed to the decomposition rates and volatilized ligand products of the metal(II/III) bis-cysteinate and acetate precursors. The study is extended to the complex cobalt(III) dithiocarbamate which is shown to produce Co_9S_8 crystals under identical annealing conditions.

In Chapter 5 I analyze the role of functional groups in the bis-cysteinate ligand and how they shape nanocrystal morphology and composition. This is achieved by substitution of precursor compounds. A recipe to achieve high-quality Co_9S_8 nanowire growth is devised through an understanding of essential function groups which include (1) a thiol source and (2) ammonia or amine source. The results strongly support the role of thiols as capping ligands that drive 1D growth. In addition annealing of specific precursor compound mixtures in a thiol environment produces narrower diameter distributions. Through the insight achieved, high yield nanowire growth is demonstrated using purely vapor-phase precursors. The growth technique enables a previously unreported method for Co_9S_8 nanowire synthesis which paves the way for a binder-free synthesis approach to cobalt sulfide nanowires on electrode materials for performance testing.

In the final chapter (Chapter 6) my results are summarized and the work's contribution to the field is discussed. Additionally, I outline possible future directions of this work.

Chapter 2

Application of Nanostructured Co, Ni, Co_9S_8 and Ni_3S_2 and 1D Synthesis Methods.

2.1 Preamble

In this chapter I discuss the importance of the material systems I have investigated and provide a comparison of the synthesis methods I have developed and other growth methods that have been demonstrated (for the same material systems).

2.2 Transition Metals and Transition Metal Sulfides

In addition to 1D morphology, the material systems investigated in this study (Co, Ni, Co_9S_8 and Ni_3S_2) are important due to their properties and earth abundance. Figure 3.1 highlights the relative abundance of elements in the Earth's upper crust. While the abundance of rare earth elements including Yb and Ce is comparable to common metals such as Ni, these elements are not found in rich, concentrated ore deposits which makes their extraction and processing costly.[79] Technologies based on abundant materials found in rich deposits offer relatively cheap raw material costs which are a dominant factor in manufacturing costs.[38,207] Co, Ni and S are readily available and cheap as they are Earth abundant and can be found in rich deposits.

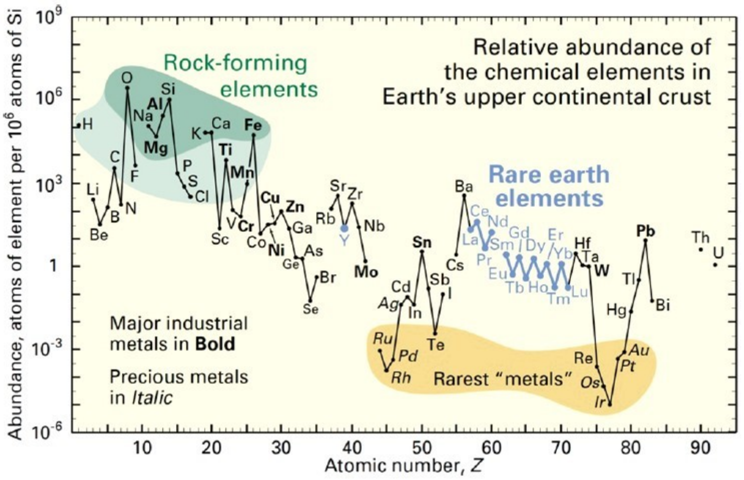

FIGURE 2.1: Abundance of chemical elements, shown as an atomic fraction of 10^6 Si atoms, with atomic number.[79]

Of all the elements in the periodic table, metals make up more than two thirds and present a wide array of starkly different properties. Investment into technology based on Earth abundant resources such as transition metals is important for low-cost deployment. Nanostructured Co and Ni have demonstrated important properties for applications in storing digital information, catalysis, spintronic based devices, sensing and biomedical applications such as therapeutics, diagnostics and separation, much of which is due to their magnetic properties.[213,231,242,198,75] The spin coupling between incomplete *d* shells in atoms such as Co, Fe and Ni gives rise to a net electron spin state known as ferromagnetic alignment.[262] Research into magnetism, particularly in symmetry breaking nanostructures (e.g. nanowires), has uncovered interesting behaviors and remains an area of intense focus.

As research has uncovered the behaviours of ferromagnetic materials, particularly in nanostructured materials, new technologies and applications have been conceptualized. Control over the spin degree of freedom of the electron has lead to the emergence of spin-based devices including spin FETs (field effect transistors), spin-LED (light emitting diode), spin RTD (resonant tunneling devices), high-speed optical switches and others. Ferromagnetic materials including Co and Ni are fundamentally important to many of these applications.[242] The emerging field of spintronics has seen the marriage of electronics, photonics and magnetism which promises to have substantial impact of future technologies.[242]

Research into transition metal sulfides (TMSs) has been driven by their physical and chemical properties, cost and Earth abundance.[113,182] The development of sustainable renewable energy sources remains a key challenge across many disciplines. At the heart of this is the development of advanced energy storage and conversion technologies. Promising candidates include next generation Li and Na ion batteries for portable and grid energy storage, and energy conversion devices such as electrocatalysts.[266] A key problem with electrocatalyst materials is that they are only active for a single reaction. Traditionally, only noble-metal-based materials including Pt, IrO_2 and RuO_2 have been shown to promote oxidative and reduction reactions.[6,155,26,5] Their deployment in large scale industrial applications is hindered through their scarcity, cost and poor stability.[6]

Nanostructured transition metal sulfides including Co_9S_8 and Ni_3S_2 have proven highly promising and stable electrocatalysts for important energy conversion reactions. The slow rates of anodic oxygen evolution reaction (OER) has been isolated as a key technical challenge preventing wider deployment. Huang *et al.* was able to show high catalytic activity and longterm stability toward both OER and HER in alkaline media using a doped Co_9S_8 nanoparticle catalyst.[90] The high catalytic activity of Co_9S_8 for ORR was predicted by Sidik *et al.* and is shown to be comparable to Pt.[192] Similarly Ni_3S_2 nanorods have been demonstrated to act as a high performance OER electrocatalyst.[269] In other transition metal chalcogenides nickel telluride ($NiTe_2$) nanowires were demonstrated to act as a better catalyst for hydrogen generation over Pt.[4] In battery applications transition metal chalcogenides (TMCs) such as FeS_2 have higher theoretical specific capacities for Li and Na ion batteries compared with traditionally used materials ($LiMo_2$ where M = Mn, Ni, Co).[123] Co_9S_8 has demonstrated high specific capacity/capacitance of lithium/sodium storage (in the range of ~300-800 mAh g^{-1}) which is greater than carbon/graphite materials currently used in these applications.[266,47,182]

Much of this behaviour is unique to TMCs with corresponding oxide phases showing diminished physiochemical properties. For example, sulfides show a diverse bonding structure, a wealth of 0D, 1D and 2D morphologies and complex valence states that exceed their respective oxide phases. TMCs demonstrate higher conductivity than their corresponding oxide phase, as well as better mechanical and thermal stability.[182] The faster charge transfer kinetics of TMCs make them more electrochemically reversible and give them a rich redox chemistry that contributes to their high specific capacity/capacitance and catalytic activity.[267,57]

2.3 Co and Ni Nanowires

Synthesis approaches to Co and Ni nanowires largely fall into two categories: template-assisted growth and capping reagent supported growth. Notably Co and Ni nanowires have not been demonstrated to grow by the VLS mechanisms. Applications as storage units in high density magnetic data storage devices has seen intense focus on the growth of dense arrays of Co and Ni nanowires. This has motivated research into electro-deposition with porous templates. Pioneering work by Whitney *et al.* and later Thurn-Albrecht *et al.* showed a route to high density cobalt and nickel nanowires with high coercivity by electro-deposition into porous polycarbonate membranes and block copolymer templates, respectively.[240,213] Since this discovery, work has sought to improve control over morphology, crystal phase and the crystallographic orientation (due to the magnetic anisotropy of the crystal).[234,149,214] To date, the formation of single-crystalline nanowires with controlled orientations have been demonstrated, however the major disadvantages of the growth technique include the multiple steps associated with the process, as well as surface roughening and contamination due to the template and its removal. Beyond data storage devices Co nanowire arrays can be used to apply mechanical forces to cells or to measure traction forces in cells.[198] Quite an interesting demonstration of template-assisted growth is the use of fibrillar biological molecules and biomolecular assemblies as a scaffold for the formation of 1D materials.[109,64] This has been exploited for a number of different material systems using different templates including DNA, proteins, peptides and viruses.[64,144,147] Knex *et al.* demonstrated the growth of 3 nm Co and Ni nanowires using the hollow structured tobacco mosiac virus as a template.[109]

Capping reagent supported Co nanowire synthesis has been demonstrated in a number of different studies. The profound influence of Alivositos on the field of nanocrystal synthesis is again highlighted by his work on cobalt. In this work HCP Co nanorods are synthesized by the injection of $Co_2(CO)_8$ into a heated bath containing the surfactants oleic acid and trioctylphosphine oxide (TOPO).[169] Similar work on the solution based synthesis of HCP Co nanowires was also shown by Dumestre *et al.*[50] Soumare *et al.* demonstrated the synthesis of HCP Co nanorods by heating cobalt(II) carboxlate salts in the presence of NaOH and 1,2-butanediol, a process later modified by Gandha *et al.* in which record high room-temperature coercivity was measured.[200,61] The nanowires are single-crystal with the c-axis (002) along the long axis of the wire.

Studies of note that do not fall into either of the above two categories include Co nanowire growth by epitaxial metal-organic CVD (MOCVD). In this work Kim *et al.* demonstrated the growth of single-crystalline Co nanowires on a *m*-cut sapphire substrate.[108] Characterization shows the nanowires to be pure phase FCC structures with identical orientation, however, the technique produced a low yield of Co nanowires. It is not clear what gives the nanowires their shape anisotropy in the study. In another example of epitaxial growth Liakakos *et al.* showed the growth of dense HCP nanowires with preferred c-axis orientation by solution phase epitaxial growth.[127] Ni nanowire arrays have also been grown by CVD on an amorphous SiO_2 surface.[25] The nanowires are single crystalline and growth is shown to occur in the (001) direction. Co nanowires have also been formed by focused electron beam induced deposition. The process involved the decomposition of a volatile cobalt precursor under a focused electron beam. The deposited material has a psuedo amorphous structure with high levels of contamination from associated ligand fragments. Subsequent annealing is able to both purify these deposits and improve their crystallinity.[140] Ni nanowire growth has also been reported by the reduction of nickel(II) in ethylene glycol using hydrazine hydrate (in the absence of any seed or surfactant).[111] The proposed mechanism is the orientated attachment of Ni nanoparticles.

2.4 Co_9S_8 Nanowires

The rich phase diagram of transition metal sulfides is never more evident than in the cobalt and nickel system. Binary cobalt sulfide phases include CoS, CoS_2, Co_2S_3, Co_3S_4, Co_4S_3, Co_9S_8.[172] As a result synthesis of nanocrystals with a pure Co-S phase remains challenging. Most 1D cobalt sulfide synthesis studies utilize an anion exchange reaction, which involves the sulfidation of a starting CoX nanocrystal.[253,143,168,28] Few studies have demonstrated the direct synthesis of Co_9S_8 nanocrystals including nanowires.[27,124,270,48,270,204] To the best of my knowledge the only reported technique for the direct synthesis of Co_9S_8 nanowires involves pyrolysis of a sulfur/thiol containing precursor over a Co/MgO catalyst as first reported by Du *et al.*[48] The method requires the use of a foreign catalyst and produces nanowires with a wide size distribution.

Chapter 3

Relevant Background Understanding

3.1 Preamble

In this chapter I discuss theory regarding bottom-up formation of nanocrystals with an emphasis on nanowires. In particular I focus on the reactions that take place and how capping ligands influence thermodynamic forces and kinetic barriers that drive nanocrystal shape and symmetry. Having examined the relevant background, I will discuss the experimental systems and methods I have employed in achieving mechanistic understand of the growth processes.

3.2 Crystallization

Crystallization is a process by which individual constituents are arranged into ordered 3D arrays. The process involves a phase transition from high free energy in the reactant state to low free energy in an ordered lattice. The physical and energy landscape for the incorporation of a chemical species into a crystal lattice is shown in Figures 3.1a and b (respectively). The energy landscape in Figure 3.1b provides an illustration of the thermodynamic driving forces and the kinetic barriers during crystal growth. Equilibrium morphology and phase are determined by the shapes and depths of minima and the kinetics by the maxima. Understanding the energy landscape is critical to the formation of high-quality nanocrystals of varying morphology and composition.

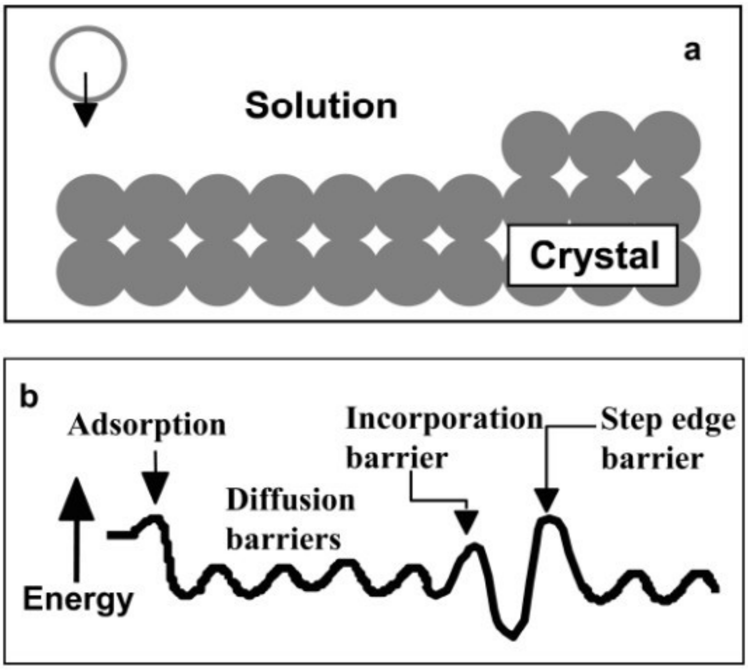

FIGURE 3.1: Schematic of the physical (a) and energy (b) landscape during crystallization from a starting molecule.[[43]]

3.3 Solution Phase Synthesis of Nanocrystals

3.3.1 Background

Solution phase techniques provide one of the most powerful means to synthesize monodispersed nanocrystals with control over size, composition and shape.[197,258] Solution-grown colloidal nanocrystals posses an inorganic core that is stabilized by a chemical species attached to their surface, known as a *capping reagent*. In one of the earliest examples of colloidal synthesis Faraday demonstrated the formation of Au nanocrystals by the reduction of gold chloride.[59] Work that followed by Henglein and Brus expanded to CdS colloidal nanocrystals by a method known as hot-injection synthesis.[83,180] Following this, seminal work by Murray *et al.* on CdE (E = S, Se, Te) nanocrystal synthesis was reported.[150] To date, the material systems and morphologies reproducibly grown are numerous. As commercial applications based on these materials are on the cusp of being realized, demands on synthesis procedures have shifted to include production of large quantities of monodispersed nanocrystals.[258,175] This has promoted research into solution-based techniques. However, due to a lack of fundamental understanding, much of the work involved in syntheses remains an art and not a science.

3.3.2 Nucleation and Growth

The crystal habit of nuclei determines many of the properties of the forming crystal structure including composition, concentration, morphology and polymorphism.[223] Nucleation (homogeneous growth) involves a phase transition from the parent phase (precursor) to the daughter phase (nucleated crystal) via an intermediate species known as *monomer*.[158,223,156] Figure 3.2 illustrates the processes involved in nanocrystal growth. Thermally stimulated dissociation of a precursor species (P) to form monomer (M) is a first order transition with a rate defined by k_f. If we simply consider a precipitation reaction in a closed system, nucleation occurs when monomer concentration is raised above a critical level known as *supersaturation*.[51] Monomer can then aggregate to form nucei; the rate is given by $k_{1,p}$. Monomer can also be incorporated into a growing crystal (heterogeneous growth). Heterogeneous growth is a competitive process governed by the rate of dissolution of monomer and incorporation of monomer shown as k_d and k_g respectively.

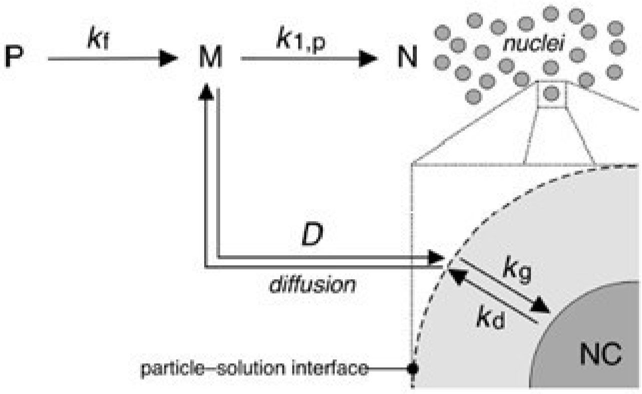

FIGURE 3.2: a) Schematic showing the processes involved with nanocrystal nucleation and growth.[[51]]

In 1950 LaMer provided the first argument for the nucleation of nanocrystals based on free monomer concentration (supersaturation) in solution, the foundation of which was thermodynamic understanding of free energy change published by Gibbs in 1876 and 1878.[67,68] Under supersaturated conditions, the solute chemical potential is greater than that of the molecules in the crystal.[159,223] Classical nucleation theory proposed that spontaneous and random aggregation of monomer occurs from liquid or solution form which assemble into nascent crystals.[67,188] The large fraction of active surface atoms in the aggregate is intrinsically unstable, therefore formation of a stable nucleus was believed to occur on a short time scale and overcome an energy barrier. Based on the high free energy of monomer aggregates and nuclei, structures below the critical radius (r_{crit}) were re-dissolved and monomers were re-supplied in the solution phase. Growth of stable nuclei occurs through monomer-by-monomer attachment. The relationship between the change in the chemical potential and creation of a new surface is given by:

$$\Delta G(n) = -n\Delta\mu + 4\pi r^2\gamma \tag{3.1}$$

Where G is the Gibbs free energy, the change in the chemical potential is given by $\Delta\mu$ for the number of constituents (*n*), and the surface free energy per unit area (γ) for a sphere with radius r. The surface free energy is positive and proceeds to destabilize the nucleus. Formation of stable nuclei occurs by the addition of monomer to a metastable nuclei. The reaction is given by:

$$M + M_n \underset{\mathrm{k}_{-1,n}}{\overset{\mathrm{k}_{1,n}}{\rightleftharpoons}} M_{n+1} \tag{3.2}$$

The equilibrium constant ($\mathrm{K}_{1,n}$) for the reaction is:

$$\mathrm{K}_{1,n} = \frac{\mathrm{k}_{1,n}}{\mathrm{k}_{-1,n}} = \frac{[M_{n+1}]}{[M][M_n]} \tag{3.3}$$

The standard change in free energy for the reaction shown in 3.2 is given by $\Delta G^0_{1,n} = -k_B T \ln K_{1,n}$. The condensation of monomer onto an infinitely large surface M_∞ is expressed as $\Delta G^0_{1,\infty} = -k_B T \ln K_{1,\infty}$. The sum of the surface and volume free energy changes for a particle upon addition of a monomer is the difference in the Gibbs free energy between the addition of a monomer to an infinitely large particle and that of a particle with a finite number of units.[52] This is expressed as $\Delta G^0_{1,n} - \Delta G^0_{1,\infty} = \Delta G^{vol}_{1,n} + \Delta G^{surf}_{1,n}$ which gives:

$$-k_B T \ln(K_{1,n}/K_{1,\infty}) = \Delta G^{vol}_{1,n} + \Delta G^{surf}_{1,n} \tag{3.4}$$

Thus the equilibrium constant is the product of the equilibrium constant for the condensation reaction of a monomer on a infinitely large surface and the Gibbs free energy barrier to the addition of a monomer to a particle with *n* units:

$$\mathrm{K}_{1,n} = K_{1,\infty} e^{\frac{-(\Delta \mathrm{G}_{1,n}{}^{\mathrm{N}})}{k_B T_V}} \tag{3.5}$$

$\mathrm{T_V}$ is the nucleus temperature, $\mathrm{k_B}$ is the Boltzmann constant and $\Delta \mathrm{G}_{1,n}{}^{\mathrm{N}}$ is the Gibbs free energy for adsorption to a nucleus with n units. Formation of a stable nuclei is contingent on n > p (i.e. greater than the critical radius).

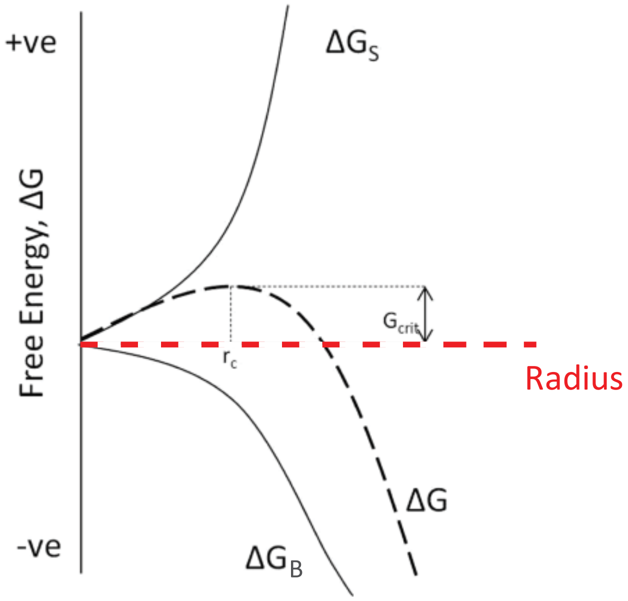

FIGURE 3.3: Diagram illustration free energy of nanocrystal nucleation (adapted from [209]).

The competition between bulk (ΔG_B) and surface (ΔG_S) free energy contributions to nuclei stability is shown in Figure 3.3 for an arbitrary system. Above the critical radius size (r$_c$) bulk contributions begin to dominate to stabilize the structure. The barrier to forming a stable nuclei is represented by G_{crit} which is overcome once the nascent crystal reaches a critical radius (r_c). Gibbs-Thomson first described the relationship between solubility and particle radius. The total free energy is given by:

$$\Delta G = \Delta G_S + \Delta G_B \tag{3.6}$$

The free energy of the surface and bulk are given by ΔG_S and ΔG_B respectively. Here the contribution from the surface energy (ΔG_S) enhances the free energy of the system according to:

$$\Delta G_S = 4\pi r^2 \gamma \tag{3.7}$$

Where r is the radius of a spherical nuclei and γ is the surface energy. Bulk contributions to the total free energy of the system (denoted by ΔG_B) may be expressed as:

$$\Delta G_B = \frac{4\pi r^3}{3} \Delta G_v \tag{3.8}$$

The Gibbs free energy per each unit volume (ΔG_v) is given by $\Delta G_v = -\frac{RT}{V_m}\ln(S)$; R is the gas constant, T is temperature, S is the level of supersaturation ($S = [M]/[M_\infty]$) and V_m is the molar volume of the monomer. Thus the total Gibbs free energy of the system (ΔG) is:

$$\Delta G = 4\pi r^2\gamma - \frac{4\pi r^3 RT\ln(S)}{3V_m} \tag{3.9}$$

The relationship describes the total free energy of the system (ΔG) for a spherical particle with radius r and surface energy γ.

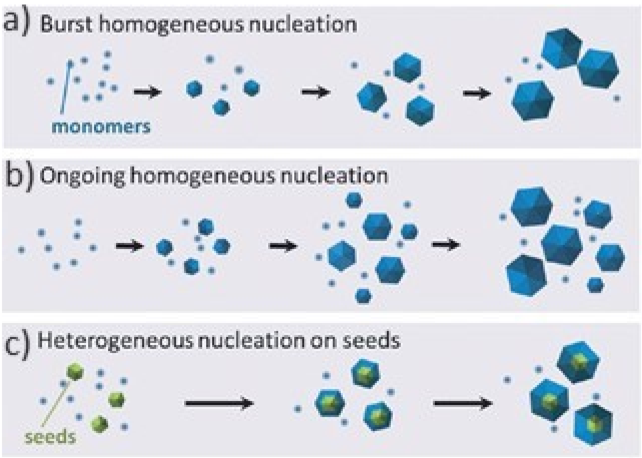

FIGURE 3.4: Nanocrystal size distribution under differing nucleation conditions including: a) burst nucleation, b) slow nucleation and c) seed mediated conditions).[236]

Monodipersed nanocrystal growth occurs in conditions in which nucleation is fast (Figure 3.4a). Monomer depletion due to rapid nucleation leads to a cessation in nucleation where the remaining monomers are consumed by growing nanocrystals. Conditions in which nucleation is slow leads to polydispersed nanocrystals (Figure 3.4b). This is due to the slow decrease in the supersaturation in the solution where sufficient monomers reside to nucleate new crystallites on a longer time scale. An alternative method using seed nanocrystals can enable control over nucleation (Figure 3.4c). The use of a crystal seed to support growth bypasses the high energy barrier involved in homogeneous nucleation by providing a base for molecular attachment.[188,101] Seed-mediated growth allows for precise control of growth kinetics to form nanocrystals with predetermined morphology and crystal phase.[245]

Classical nucleation theory still forms the basis of our understanding and successfully describes various phenomena such as the condensation of water droplets from vapour.[85] The direct formation of nuclei from small aggregates is shown by the diagonal arrow in Figure 3.5a (as described by classical

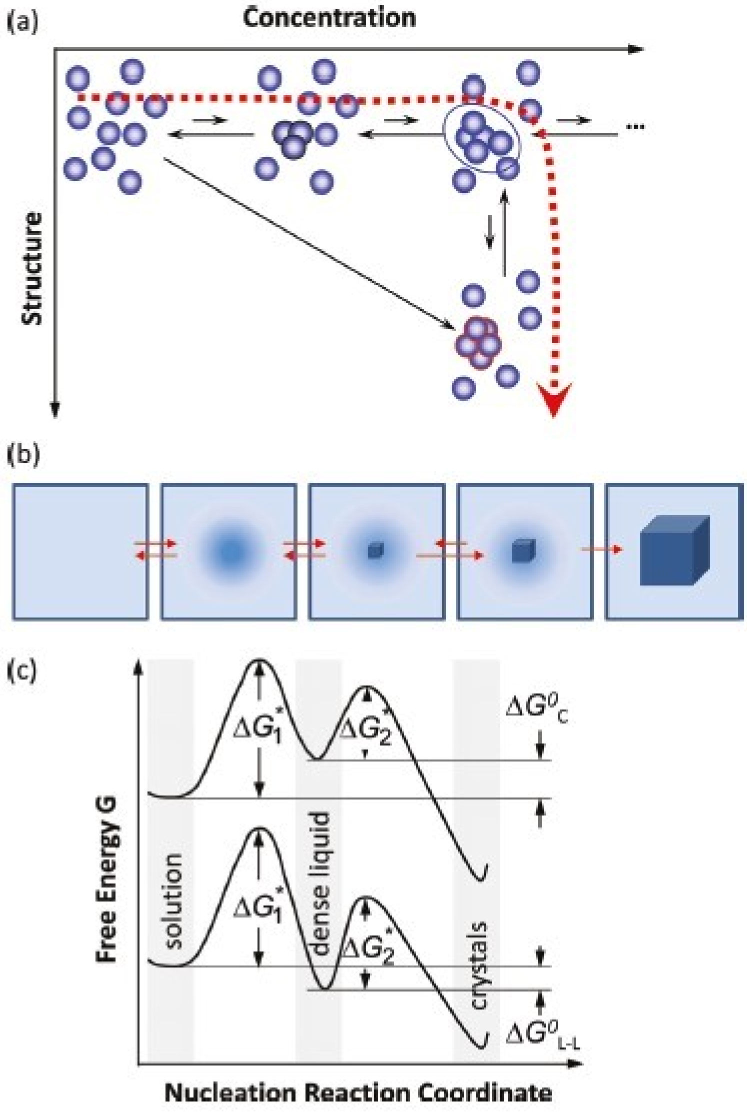

FIGURE 3.5: a) Monomer concentration and b) schematic illustration during monomer aggregation and nanocrystal. c) Free energy diagram for two-step nucleation.[223]

theory). However for more complex systems, it breaks down completely, predicting nucleation rates that are 10 orders of magnitude slower than experimentally measured rates for lysozyme and ice.[54,134,224,185] Experimentally supported proposal of the two-step nucleation process was presented by ten Wolde and Fenkel which built in greater complexities and dynamics of chemical species in a supersaturated solution.[241] Non-classical nucleation models have emerged with widespread agreement in an additional step that precedes nucleation.[222,43] A schematic and free energy diagram for two-step nucleation theory is shown in Figure 3.5. Figure 3.5a illustrates the monomer concentration during the stages of nucleation and growth. Figure 3.5b shows a schematic of the processes preceding nanocrystal growth which include formation of a supersaturated solution, monomer aggregates and cluster formation, homogeneous growth and heterogeneous growth. Experimental observations have also shown the formation of nuclei inside suspended metastable clusters several hundred nanometers in size, contrary to classical growth theory.[223]

3.3.3 Thermodynmics and Kinetics

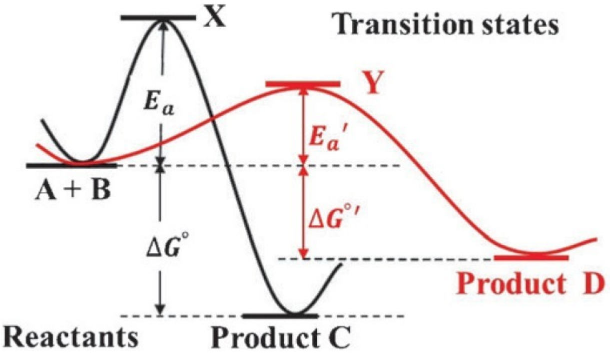

FIGURE 3.6: Energy landscape for the formation of products under thermodynamic and kinetic control.[[236]]

Systematic control during crystal growth hinges on an understanding of the thermodynamic and kinetic processes. If we consider the reaction between reactants A and B, product C or product D can form depending on whether the reaction is thermodynamically or kinetically controlled (Figure 3.6). A product can form because it is the most stable state or because the pathway to its formation has the lowest associated energy barriers.[236] For a thermodynamically controlled reaction, reactants A and B form Product C and the equilibrium constant (K) is exponentially dependent on the driving force ΔG^o (Equation 3.10). Here, the most stable state is reached, which may follow several intermediate product states. If the reaction is kinetically controlled, product D forms. The reaction is significantly faster as the rate constant is exponentially dependent on the activation energy (Equation 3.11).

$$K = e^{-\frac{\Delta G}{RT}} \tag{3.10}$$

$$k_1 = Ae^{-\frac{E_a}{RT}} \tag{3.11}$$

In practice, discerning whether a particular nanocrystal synthesis procedure is thermodynamically or kinetically controlled can remain challenging.

Means of studying this in chemistry cannot be adapted to nanocrystal growth owing to the heightened complexity. Unlike a typical chemical reaction multiple concurrent processes are occurring during nanocrystal synthesis. For small metallic clusters (>100 atoms), calorimetry and computer simulations can determine the relative stability of the initial, intermediate and product states.[236] Detailed thermodynamic and kinetic analyses have been reported on systems of this scale.[9,11,10] For larger systems, new methods are required, concentrating on dominant factors and major trends.[191,236] The reaction conditions can be optimized to maximize the nanocrystal yield under thermodynamically and kinetically controlled synthesis procedures. Under thermodynamical control, yield may be optimized by increasing the temperature and time to allow the reaction to approach equilibrium, while under kinetic control the temperature should be enough to enable the reaction to proceed and the product should be isolated as quickly as possible. The influence of competitive reactions and reverse reactions must me minimized.

3.3.4 Equilibrium Nanocrystal Shape

Minimization of the total interfacial free energy drives a waterdroplet to form spherical shapes, (surface-free energy is for a surface in vacuum). This can be simply illustrated by considering the forces acting on a molecule in a water droplet and on the droplet surface (Figure 3.7). The strong hydrogen bonding between molecules and the weak interactions with air cause a net force on surface molecules towards the center of the droplet driven by the maximization of favorable bonding interactions. The stronger the bond interaction the greater the force to reduce the surface area. The same forces drive the equilibrium shape of nanocrystals. In contrast to molecules in a water droplet, the energy landscape becomes complicated by packing efficiency of surface atoms, charge distribution and capping ligands.

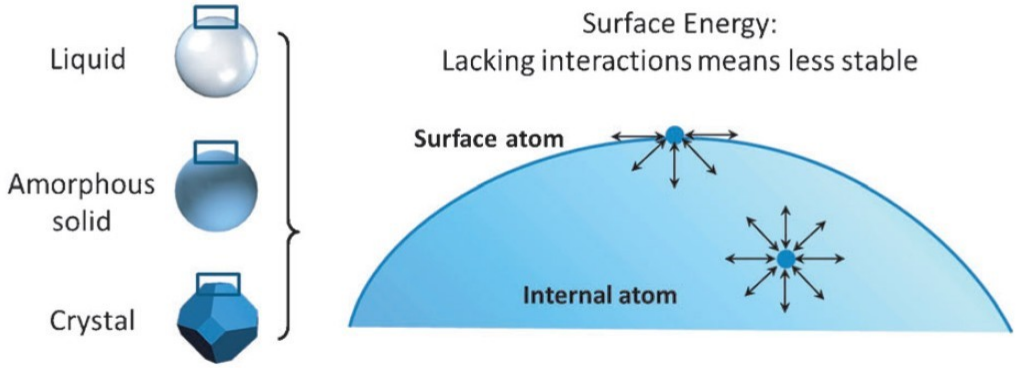

FIGURE 3.7: Illustration of net forces acting on surface atoms and atoms in the bulk in a water droplet.[236]

The shape of inorganic nanocrystals is governed by a combination of energetic and kinetic factors.[22,33] For single domain nanocrystals the energy landscape is dominated by the relative surface energy of different crystal facets, surface charge and capping ligands; it is therefore challenging to determine if the formation of a nanocrystal is thermodynamically or kinetically controlled.

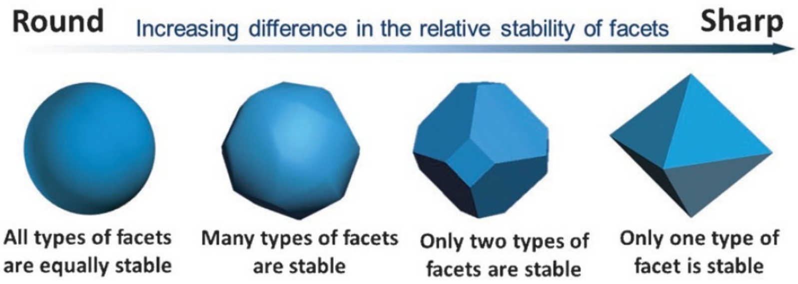

FIGURE 3.8: Equilibrium shape of nanocrystals due to surface free energy contributions.[236]

The controlling forces in a single-domain nanocrystal seek to minimize the total surface free energy, which is the sum of the products of the surface free energy (γ) for a facet and its surface area (A) $\Delta G = \sum \gamma_i A_i$. An approximation of the most stable product, for a given volume, can be calculated based on the thermodynamics using Wulff construction.[84,246] Bond interactions govern the stability of a facet. The surface energy of major facets in a FCC crystal in increasing order is: $\gamma_{(111)} < \gamma_{(100)} < \gamma_{(110)}$.[237,264] High-energy facets contain low-coordinated atoms, therefore low energy barriers associated with incorporation of chemical species. The exponential dependence of the growth rate on the surface energy leads to the disappearance of high energy facets as they become flanked by slow forming, low energy facets.[258]

This explains why surface coverage of nanocrystals tends to be dominated by low-index facets.[171,221] A system in which only one facet is preferred produces a polyhedron with sharp edges and corners, examples include octahedra with (111) facets or cubes with (100) facets.[236] Equilibrium shape is rarely achieved in nanocrystals.[43] Commonly, nanocrystals appear with truncated edges and corners on account of the small energy difference between facets.[236] Defects, charge distribution (in ionic crystals) and capping surfactants also shape the energetics of crystal formation. Until now single element nanocrystals were discussed, however in ionic crystals such as NaCl equilibrium shape is strongly influenced by charge distribution. The result is the stability of (100) facets in NaCl owing to their neutral charge.

3.3.5 Capping Ligands

Molecular species with relatively strong binding affinity to nanocrystal facets are known as capping reagents.[70] This includes surfactants, polymers, monotomic ions (e.g. Cl^-, Br^-, I^-) and small gas molecules (e.g. CO, O_2, H_2S). These species act as chemical impurities that lower the interfacial energy through absorption to a surface.[43,258] Their deployment has enabled (1) stabilization of nanocrystals, particularly on the size scale in which the interfacial free energy dominates, (2) morphology control or the selective formation of facets and (3) to drive anisotropic growth in nanocrystals. They may be added independently of growth precursors or formed during precursor decomposition. Stabilization of a surface by the interfacial energy change can be used to precisely modulate the growth rates of different sets of facets, thus achieving a thermodynamic means of shape control.[246] Figure 3.9 shows the rich morphologies of monodomain Ag nanocrystals formed under different reaction conditions with different capping reagents. The results show that at smaller sizes Ag nanocrystals form a Wulff polyhedral profile (to minimize surface energy), the addition of polyvinylpyrrolidone (PVP) during growth results in stabilization of {100} facets which drive the formation of cuboctahedrons (Figure 3.9a) and perfect nanocubes (Figure 3.9b).[246] In the presence of Br^- anisotropic growth can be achieved resulting in Ag nanorods (see Figure 3.9e).

The energy with which ligands bind to a facet can vary by an order of magnitude depending on the surface. An example is citric acid to Ag {111} and {100} surfaces which is 13.8 and 3.7 kcal/mol respectively.[103] Change in the interfacial energy has also been shown to lead to the stabilization of

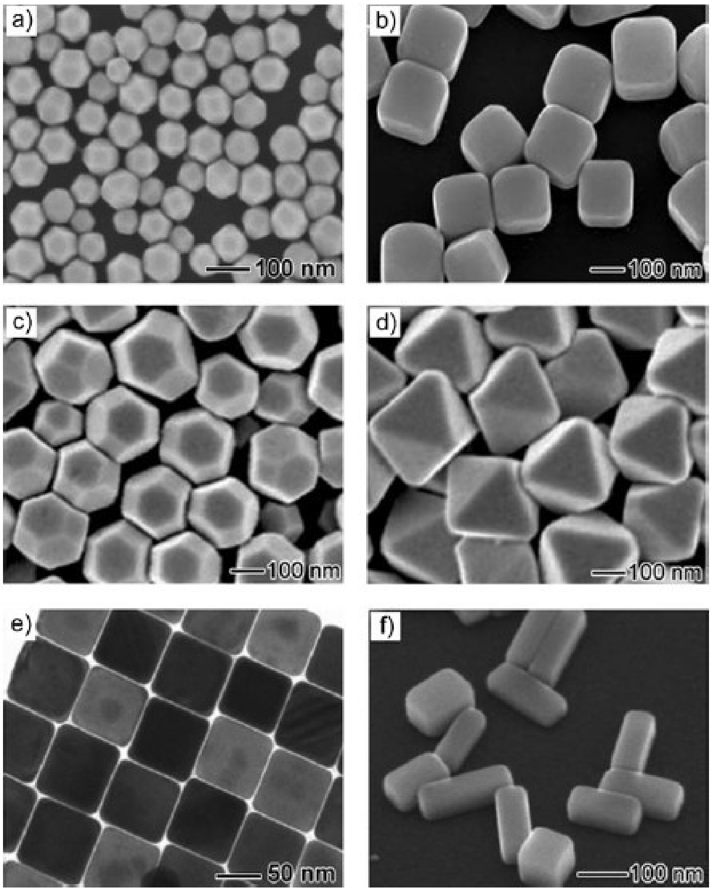

FIGURE 3.9: Electron microscopy images of monodomain Ag nanocrystals prepared under different reaction conditions with different capping reagents.[246]

high index facets. This is evidenced by the formation of Au trisoctahedral nanocrystals with high index {221} facets using hexadecyltrimethylammonium chloride.[137]

Figure 3.10a shows the nanocrystal morphology with different relative concentrations of oleic acid to oleyamine. Equilibrium crystal shape is shown in Figure 3.10b based on surface coverage and binding energy of oleic acid on {100} and {111} facets of a PbSe nanocrystal. The studies highlight the important relationship between the crystal habit with ligand concentration and binding energy. The equilibrium shape is computed based on the change in the surface energy using density functional calculations and compared with experimental results.[125,13] The dependence on surface coverage with oleic acid binding affinity results in considerably higher surface coverage on the reconstructed $\mathrm{PbSe}_{\{111\}}$ facets when compared with $\mathrm{PbSe}_{\{100\}}$ facets. Therefore low concentrations of oleic acid results in high surface coverage of $\mathrm{PbSe}_{\{111\}}$ surfaces leading to their stabilization and negligible coverage on $\mathrm{PbSe}_{\{100\}}$ surfaces. The result is an octhedral equilibrium core shape. High concentrations of oleic acid produces a relative change in interfacial energy ($PbSe_{\{111\}} < PbSe_{\{100\}}$) which results in the formation of cube nanocrystals. The crystal habits for conditions between the two extremes are also included.

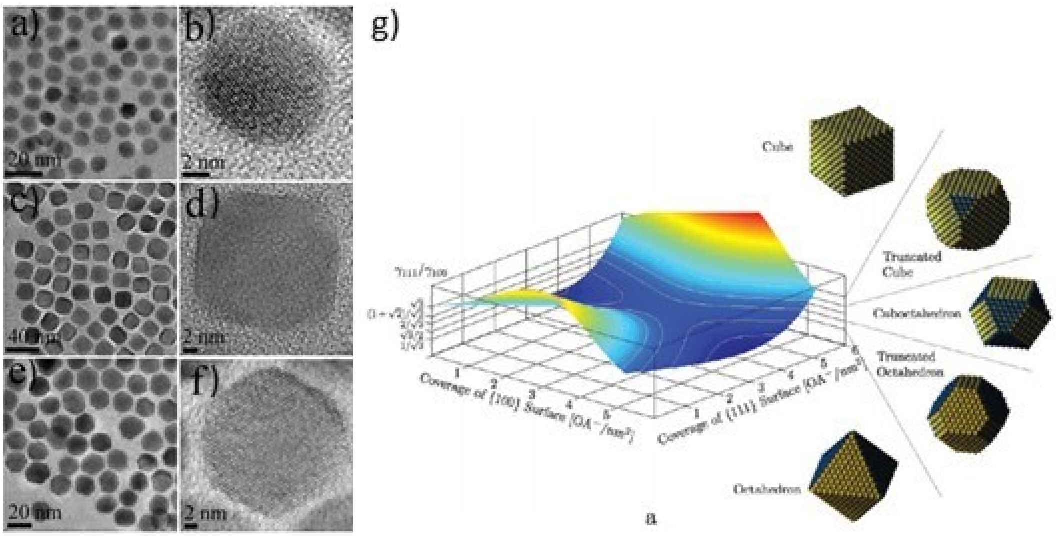

FIGURE 3.10: TEM and HRTEM images of PbSe nanocrystals with different crystal habits including (a and b) spherical, (c and d) cubic and (e and f) cuboctahedral .[125] g) Change in equilibrium shape based on surface coverage of {100} and {111} facets and the corresponding ligand affinity.[13]

Stability of a terminating ligand depends on (1) the affinity for a surface or the chemical bonding at the surface site (2) the interactions with neighboring ligands and (3) the surrounding chemical environment (i.e. solvent effects).[167] Typical surfactants have electron-donating atoms to allow coordination to electron-poor metal surface atoms.[258] Binding of ligands during nucleation and growth is a dynamic process, in which adsorption and desorption is ongoing.[98] Selective deployment of capping ligands thus forms a powerful tool for shape engineering of nanocrystals. Relative control is determined by the ligand-surface bond type and strength and ligand-ligand interactions. Despite its wide use and importance, a full understanding of the mechanism in which capping ligands shape nanocrystal morphology is still elusive.

3.3.6 Symmetry Breaking Growth

Low symmetry structures, such as nanowires, that evolve from high symmetry nuclei requires a symmetry breaking event.[229] Understanding the mechanism by which symmetry breaking growth occurs has proven challenging, and the role of chemical species complex. The high surface area of anisotropic shapes make them likely metastable and by definition their formation is kinetically governed.[258] Mechanistic studies of capping reagents have uncovered behavior beyond simple passivation of a family of planes. In many studies, capping ligands work in conjunction with defects or catalysts to promote 1D growth. Considering the equilibrium shape of a monodomain FCC nucleus, equal passivation of any family of facets inhibits any symmetry breaking growth. For example the equilibrium shape of a monodomain FCC crystal forms a truncated octahedron bound by 6 {100} and 8 {111} facets (Figure 3.11). If growth is terminated on all {111} facets due to the presence of a capping ligand, the resulting morphology is a symmetry conserving octahedron bound by equivalent {111} facets.[225] Thus in many examples of symmetry breaking growth there is a gap in explaining the inequivalent growth rates of equivalent facets from symmetrical nuclei.[236] Understanding of how surfactants support 1D growth is an active area of research.

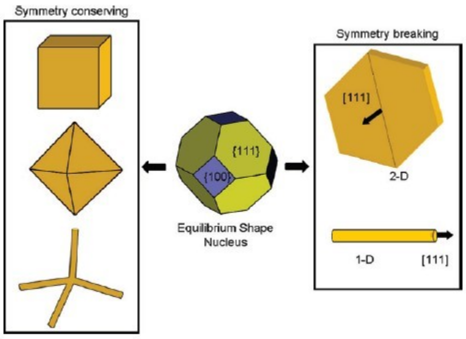

FIGURE 3.11: Schematic illustration the resulting morphology based on symmetry conserving and symmetry breaking growth from the equilibrium crystal habit of a monodomain FCC crystal nucleus.[[225]]

The relative simplicity (when compared with other methods), the high quality of the product and the ability to be scaled up to produce grams of material has driven extensive research into solution-based syntheses of metal (Au, Ag, Pd and Cu) nanowires.[173] Widespread belief was that the oxidation of the reducing agent produced electrons to reduce the metal cation in the presence of a capping agent to direct growth. The complex effects are highlighted in a study on 1D growth of monodomain Pd nanocrystals. Here, the authors propose that 1D growth is induced by localized oxidative etching in the presence of bromide. Under this mechanism the starting nucleated seed is a monodomain cube contained by {100} facets formed via the presence of a chemisorbed bromide layer.[250] Localized oxidative etching on a single face occurs with the assistance of water, making the site active for the addition of Pd atoms. The addition of adatoms out-competes dissolution by etching and the net effect is anisotropic growth to form a nanobar enclosed by {100} facets (Figure 3.12).[250,247] An octagonal nanorod bound by {100} and {110} facets is formed if the seed crystal is cuboctahedral in shape.[250] Experimental work to test this theory was conducted by adding citric acid to block oxidative etching, the resulting morphology was nanocrystals with reduced aspect ratio suggesting that oxidative etching drives anisotropic growth.[250,251] The authors support this argument by noting that in similar studies oxidative etching can occur on a single surface when equivalent facets are present. The cited studies include corrosion of a single face on a Pd nanocube that is surface terminated by PVP and all sides are equivalent {100} facets, similarity localized etching of a surface on a Au nanocube during galvanic replacement reaction with $HAuCl_4$ the cube has six equivalent $Ag_{\{100\}}$ facets. [248,205] Selective oxidation was also reported on the tips of single crystal Au nanorods formed by {100} facets which was not apparent on the side {100} facets.[220] This study on anisotropic growth in Pd is one of the very few in which a mechanism is proposed and evidenced.

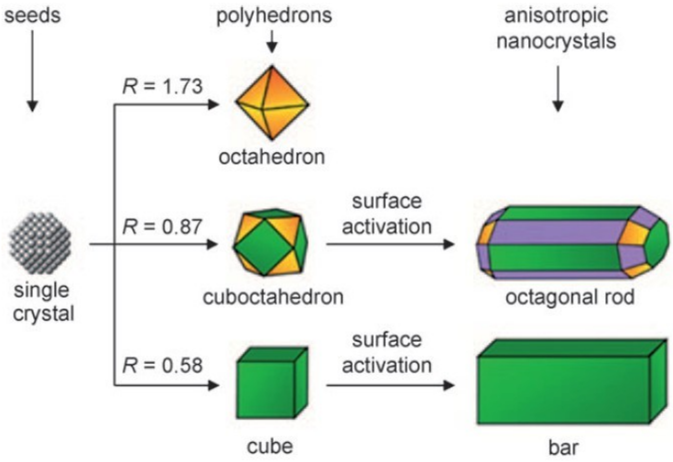

FIGURE 3.12: Seed evolution of a monodomain nanocrystal. R is the ratio of the growth rates along the <100> and <111> directions.[[246]]

The commonly held belief is that functional amine groups facilitate 1D growth of five-fold twinned Cu nanowires by facet specific termination (capping reagent mechanism). Capping agents used in syntheses studies include ethylenediamine (EDA), hexadycylamine (HDA) and octadecylamine (ODA).[107,133,146,254] Prevailing theory has been that the capping ligand preferentially adsorbed to side-wall {100} facets, promoting incorporation of metal atoms onto {111} facets at the end of the growing nanowire. However, mechanistic studies based on electrochemical measurements of single crystal Cu(111) and Cu(100) showed that EDA increased the reduction rate of Cu(OH)$_2^-$ on a {111} facet relative to {100}.[107] The results prove that EDA does not act to inhibit growth on side-wall {100} facets, rather it promotes the reduction of Cu(OH)$_2^-$ on {111} end facets which restricts the formation of Co oxide. Cu oxide preferentially formed on nanowire side ({100}) facets, acting to inhibit radial growth. Figure 3.13 shows the reduction efficiency of Cu(111) and Cu(100) single-crystals as a function of time, and a schematic illustrating the mechanism by which anisotropic growth occurs.

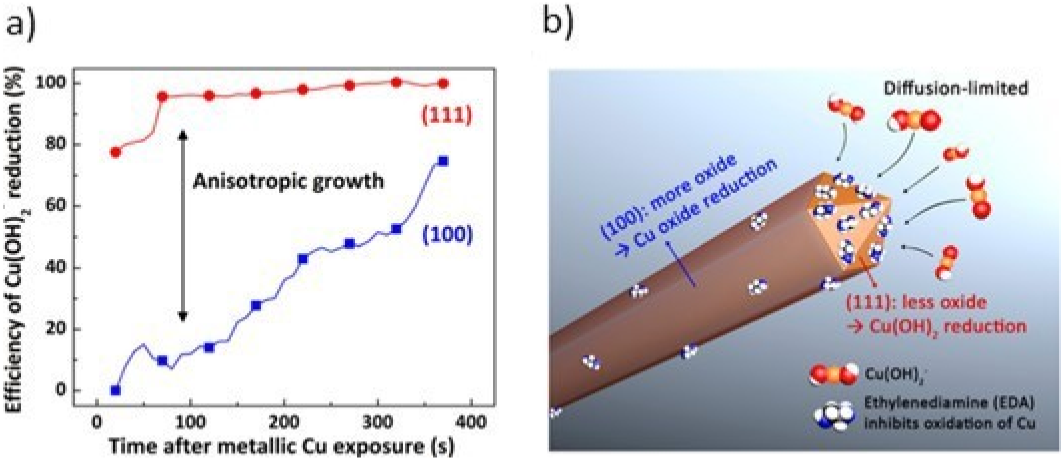

FIGURE 3.13: a) Electrochemical measurements showing the different efficiencies of Cu oxide reduction between the (111) and (100) planes. b) Schematic representation of the diffusion-limited process.[107]

The use of capping reagents to achieve symmetry breaking growth is largely studied in wet-chemical synthesis techniques, however more recently has been noted to play an important role in vapor based techniques including the VLS mechanism.[196,257] In the first example ligand fragments, liberated upon Au catalyzed growth of Ge nanowires, chemisorb to stabilize nanowire side-wall facets.[196] Under low surface coverage conditions of the ligand fragments, radial growth leads to tapering. Operando infrared (IR) spectroscopy measurements confirm the presence of chemisorbed H through ν(Ge – H) absorption bands during growth. The relative surface coverage is critical to stable axial growth (Figure 3.14a). The terminated hydrogen fragments are generated through the dissociative adsorption of the nanowire growth precursor Ge_2H_6. In the second example sulfur vapour is introduced during the growth of Au catalyzed GaSb nanowires. Stabilization of the nanowire surface is shown to occur through the formation of S-Sb bonds on the nanowire surface which acts to prevent unintentional radial growth.[257] Figure 3.14b shows the formation of tapered nanowires in the absence of sulfur vapor (top), and the uniform diameter in the presence of sulfur along the entire length of the nanowire exceeding 10 μm in length. Important consequences of this work is the improved transport properties of nanowires. Morphological imperfections including surface roughness and tapering act to scatter carriers affecting the overall performance. Yang *et al.* showed that the peak hole mobility improved by an order of magnitude (20 to 200 cm^2/V.s) by eliminating radial growth of nanowires with the introduction of a capping ligand.[257]

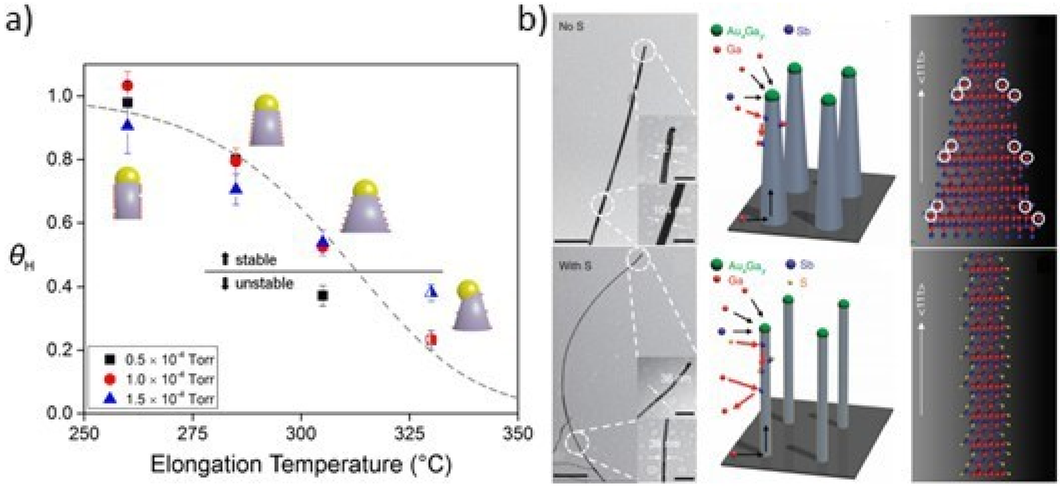

FIGURE 3.14: a) Resulting nanowire morphology with precursor partial pressure and temperature.[107] b) TEM and schematic images illustrating nanowire morphology in the (top) absence of sulfur and (bottom) presence of sulfur.[257]

3.3.7 Defects and Anisotropic Growth

Defects in crystals highlight the important relationship between crystal habit and the resulting nanocrystal morphology. This is arguably most evident in the growth of low symmetry materials such as nanowires and nanoplates. Amongst the types of defects (point, linear, and planar) planar defects including twin defects and stacking faults are most influential in determining morphology.[70]

In solution-based syntheses, the rate at which monomer is generated has been shown to shape the crystal habit of the seed. Studies of Pd show that monodomain seeds are formed when monomer generation is comparatively fast. Whilst conditions which lend itself to slower generation of monomer

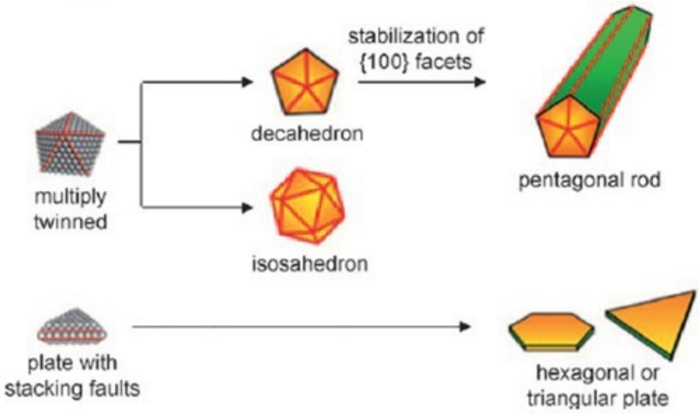

FIGURE 3.15: Anisotropic growth from crystal nuclei with common defects: five-fold twin boundary and stacking faults.[[246]]

produce multiple twinned seeds.[247] The rate can be controlled by the reaction temperature and strength of the reducing agent, mild reducing agents such as citric acid or ascorbic acid promote the formation of twinned seeds.[247] The extra strain energy (in twinned nanocrystals) is compensated for by maximizing the surface coverage with {111} facets to achieve the lowest surface energy.[2] The crystal habit of twinned seeds produces twinned nanowires (Figure 3.15). In the case of Pd pentagonal twinned nanorods anisotropic growth occurs through stabilization of {100} planes by bromide and preferential axial growth to minimize the strain energy.[249] Planar defects known as stacking faults are common defects found in FCC metals owing to the low energy barrier to their formation under slow reaction conditions.[65] These defects form parallel to the (111) surface and play an important role in the formation and growth of plate-like nanodisks (Figure 3.15).[65]

3.3.8 Nanocrystal Growth Using Vapor-Phase Precursors

Nanocrystal growth using vapor-phase reactants shares many similarities with solution based such as similar basic chemical reactions involved with precursor conversion. The process includes transport of precursor species, pyrolysis, nucleation and growth. Volatile precursor species are carried to a locally or globally heated substrate, pyrolysis of the precusor species leaves reactive chemical species for crystal growth. Then through homogeneous or heterogeneous addition nucleation and growth occurs. Typically growth by chemical vapor deposition occurs at high temperatures and involves the use of a catalyst and/or capping ligands.

3.4 Experimental Set-Up

High vacuum annealing work was performed using a home built reaction chamber (Figure 3.16). The chamber and gas delivery lines are assembled from purpose-built, ultrahigh vacuum parts all with 'metal-on-metal' seals using copper and stainless steel gaskets. Samples are mounted directly onto a stainless steel stage and held in place using a stainless steel clip. A replica substrate is also mounted onto the stage with a K-type thermocouple clipped to the surface. The commercial heater consists of a pyrolytic graphite resistance heating element housed within pyrolytic boron nitride (PN/PGN), is capable of annealing experiments at temperatures greater than 1500°C (in a non-oxidising environment) and is ultra-high vacuum compatible. The system is pumped with an Edwards x10 series scroll pump and turbo molecular pump (TMP). The pumps are oil free to eliminate the back diffusion of contaminants. A capacitance manometer (10 Torr Baratron) is used for low pressure measurements and an ion gauge pump (IGP) for high vacuum pressure recording. A shut-off valve isolates the IGP from the system during venting or low pressure experimental work. The temperature and pressure are recorded by an in-house constructed labview program. Dedicated heating lines hold the chamber and gas delivery lines at 60°C to reduce the residence time of adsorbates enabling more efficient exhausting of contaminants including water and hydrocarbons.

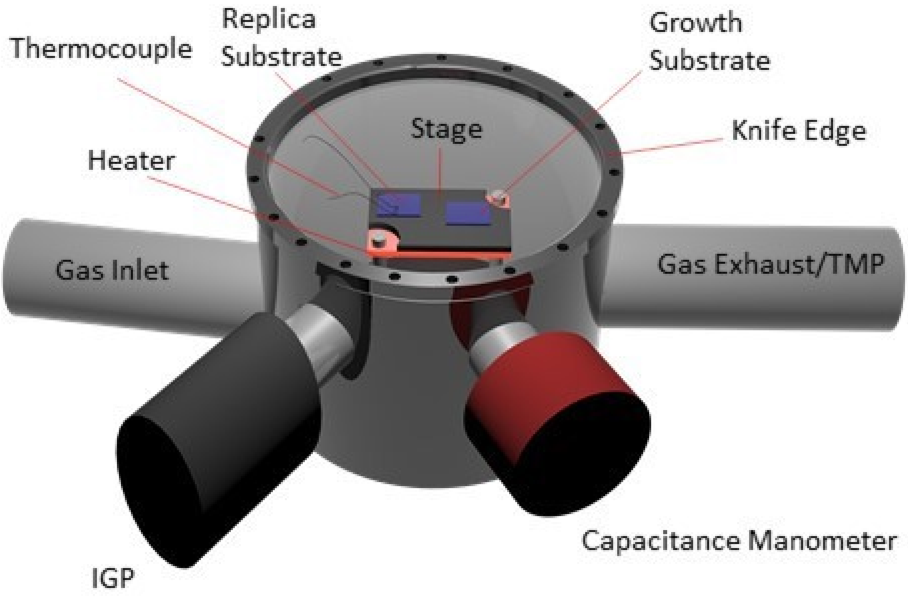

FIGURE 3.16: Schematic illustrating high vacuum annealing chamber.

The system is dedicated to annealing work in high vacuum or volatile gas environment, no vapour phase organic or organometallic precursor species are introduced into the chamber. The default status of the system is a high vacuum under continuous pumping and heated to 60 ^{o}C with externally wrapped heating lines. The system is vented with a dedicated N_2 line, the chamber is held in a super-atmospheric N_2 pressure during sample loading/unloading to reduce introduction of contaminants. During a typical annealing experiment the chamber is vented and the sample is mounted on the heater. The chamber is pumped to base pressure (1 x 10^{-7} mbar) and the sample is heated by manually adjusting a dedicated power supply. Pressure and temperature are monitored in real-time.

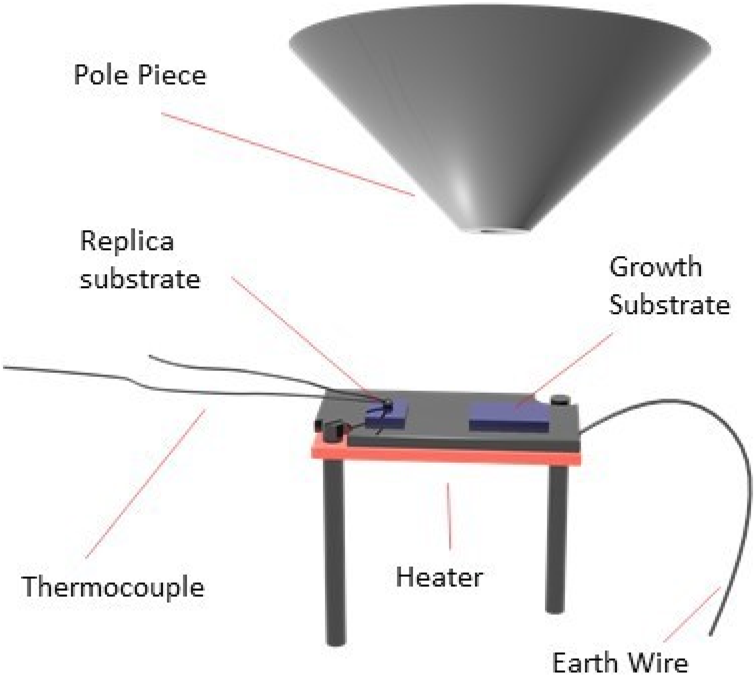

FIGURE 3.17: Schematic illustrating stage configuration for *in situ* SEM characterization during nanowire growth.

In situ FESEM characterization was conducted on a Nova nanoSEM Sirion column. The thermal field emission source and in-lens secondary electron (SE) detector give excellent high-resolution imaging. A custom built stage that allows for heating is shown in Figure 3.17. Here an identical PG/PBN resistive heater is used with a replica substrate to measure the temperature. A ground wire attached to the stage allows for imaging as the stage is mounted on an electrically insulating material. The stage set-up allows for thermolysis of precursor species and SEM characterization during growth which is discussed in Chapter 4.

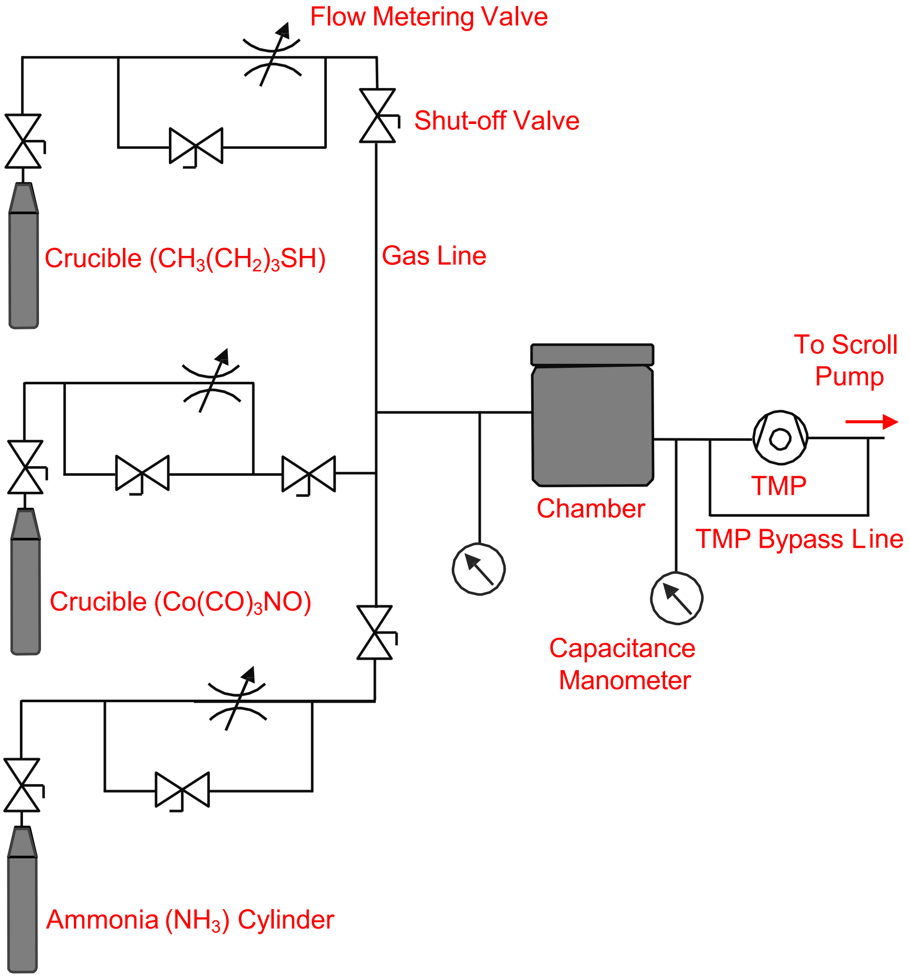

FIGURE 3.18: Schematic illustrating cold-wall CVD and precursor delivery systems.

Annealing work in a vapor environment was performed on 2 systems: a cold-wall and hot-wall chemical vapor deposition (CVD) system. The cold-wall CVD chamber is an identical replica of the high-vacuum annealing system (Figure 3.16). The major difference being that the system is used for chemical vapor deposition experimental work and as a result requires additional procedures to reduce contamination. Before a sample is loaded the chamber is heated to 600 °C for 1 hour under continuous pumping with the TMP to remove residual containments. A full diagram of the cold-wall CVD and gas delivery systems is shown in Figure 3.18. The system was used for two-step annealing experimental work using both ammonia and butanethiol vapor as well as CVD work using the precursors cobalt tricarbonyl nitrosyl and butanethiol (Chapter 5). The gas delivery lines are stainless steel flexible hosing all with metal-on-metal seals between joining components and maintained at 60 °C. Precursors for CVD work (including butanethiol and cobalt tricarbonyl nitrosyl) are loaded under inert (N_2 atmosphere) into a stainless steel crucible and sealed using a shutoff valve with metal-on-metal sealed connectors. The crucible is mounted onto the gas delivery lines and undergoes freeze-pump-thaw cycles to remove residual N_2 and volatile chemical impurities.

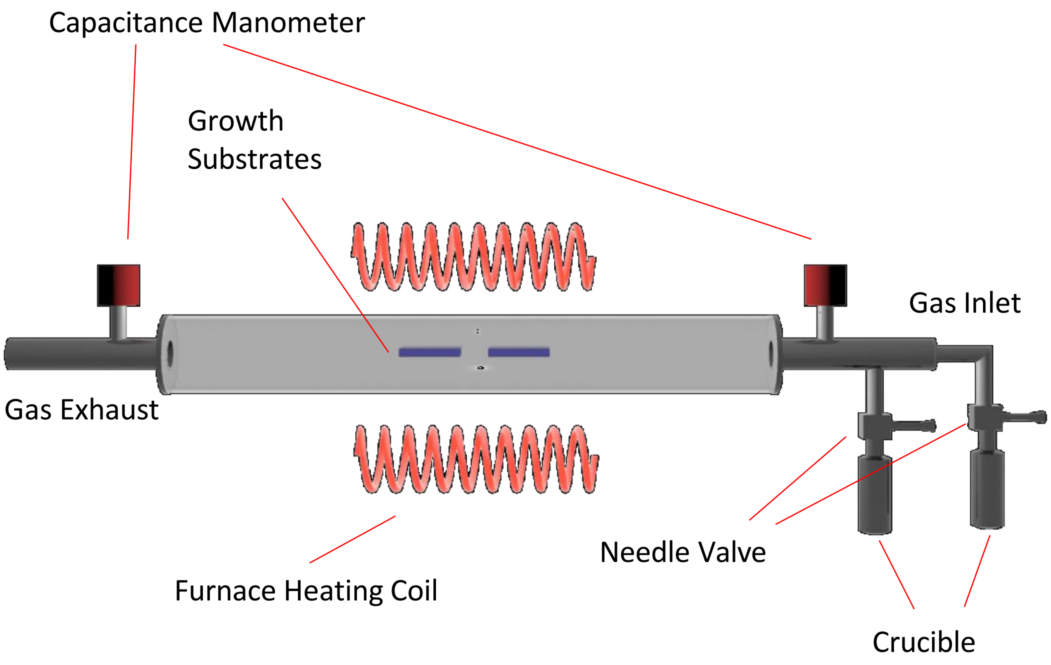

FIGURE 3.19: Schematic illustrating hot-wall CVD and precursor delivery systems.

Sulfur is well known to corrode stainless steel at elevated temperatures.[217,102] Owing to the many stainless steel components in the cold-wall CVD chamber much of the experimental work using sulfur containing vapor phase precursors was conducted using a hot-wall CVD system (Figure 3.19). In this system the reaction occurs in a quartz tube which is resistant to sulfur corrosion enabling experimental work at higher temperatures under increased butanethiol pressures for longer reaction times. Here a furnace heats a section of quartz tube in which the substrates are housed and precursors are flowed over the substrate(s). Pressure is measured using 2 capacitance manometers (range 0.01 - 10 Torr) located at the gas inlet and exhaust of the quartz tube.
The system is pumped using a Edwards x10 series scroll pump. Before each experiment the furnace is heated to 1000 °C and purged with 1000 sccm Ar for 30 minutes. Precursors are stored in stainless steel crucibles, their partial pressure is controlled by regulating their flow rate using needle valves. The precursor delivery system is configured in an identical manner to the cold-wall CVD precursor delivery system (shown in Figure 3.18). The heating

rate is programmable and the feedback temperature was correlated independently using a thermocouple during a typical growth.

Chapter 4

Synthesis of Co_9S_8, Ni_3S_2, Co and Ni Nanowires by Solventless Thermolysis of Cysteine-Based Precursors

4.1 Abstract

The synthesis of Co_9S_8, Ni_3S_2, Co and Ni nanowires by solventless thermolysis of simple-molecular precursors based on the amino acid cysteine is reported. Nanowires are realized by thermolysis of a mixture of metal(II) acetate and cysteine in vacuum. The simple precursor system enables the nanowire phase to be tuned from pure metal (Co or Ni) to metal sulfide (Co_9S_8, Ni_3S_2) by varying the relative concentration of the metal(II) acetate. The growth environment enables new insight through *in situ* characterization during thermolysis using field-emission scanning electron microscopy (FESEM) and thermogravimetric analysis with gas chromatography-mass spectrometry (TGA-GC-MS). FESEM reveals the temperature at which nanowire growth occurs and suggests that adatoms are incorporated into the base of the growing nanowire. TGA-GC-MS reveals the rates of precursor decomposition and identity of the volatilized ligand fragments during heat-up and at the nanowire growth temperature. Our findings provide new understanding into precursor chemistry that supports anisotropic growth in nanocrystals by heat-up synthesis.

4.2 Introduction

Colloidal synthesis by hot-injection and heat-up coprecipitation techniques are powerful methods for achieving monodisperse nanocrystals with controllable size, morphology and composition.[83,151,161,150,180,97] An understanding of the precursor conversion reactions is crucial to expanding the scope of these techniques to new material systems and morphologies.[97,263,82,181,177] To date, few reports have examined the reactivity of precursors that influences anisotropic growth highlighting the need for *in situ* characterization.[181,209,74] Characterization of the reactions during nanocrystal growth can be challenging because of the speed at which transformations occur as well as solvent effects.[60,110,95] *In situ* characterization studies have utilized mostly UV-vis absorbance and nuclear magnetic resonance spectroscopies in the solution state, although these techniques can suffer due to lack of sensitivity (in NMR), the generation of optically transparent species, anomalous extinction due to scattering, and temperature dependent optical properties of nanocrystals.[53,170,131,157,77,201,99,260]

Solventless thermolysis is a versatile sub-set of coprecipitation techniques that enables crystal growth under straightforward conditions, and has been used to synthesize high quality copper, nickel and bismuth sulfide nanocrystals of various morphologies with narrow size distributions.[194,115,66,193] Only a few direct bottom-up syntheses have been reported for Co_9S_8 nanocrystals including nanowires.[27,48] Rather, most reported techniques utilize a multi-step method whereby a metal oxide structure is first formed and the sulfide phase produced by exchange of the oxygen atoms for sulfur.[27,270,253,29] The morphology is determined by the intermediate Co_xO_y nanocrystal followed by anion exchange ($Co_xO_y + RS \rightarrow Co_wS_z$), typically causing hollowing of the nanostructure by the Kirkendall effect.[258,29,128]

In this chapter an examination of the growth precursors used in a high vacuum thermolysis technique that yields nanowires of Co_9S_8, Ni_3S_2, Co and Ni is provided. Metal(II/III) bis-cysteinate and metal(II) acetate (where metal = cobalt or nickel) were used to examine the influence of their relative concentrations on the resultant nanowire phase. *In situ* characterization of the thermolysis behavior of the precursors was examined using FESEM and TGA-GC-MS. The results reveal (in both precursor systems) a single-step mass loss event to yield M_xS_y species followed by a slow loss of sulfur species at nanowire growth temperature. The results are compared with cobalt(III) dithiocarbamate, which demonstrates similar decomposition behavior and produces Co_9S_8 nanocrystals under identical growth conditions.

Sulfur species are known capping ligands that can support anisotropic crystal growth and provide control over the resultant crystal morphology.[193,257,252] Capping ligands are typically either added to growth precursors, or generated *in situ* as reaction by-products during nanocrystal growth. The latter approach, employed here, is advantageous due to the ability to eliminate side reactions, greater precursor air stability (relative to metal alkyls), and ease of manipulation.[176,1,130] Our results constitute a new approach for the selective fabrication of high quality Co_9S_8, Ni_3S_2, Co and Ni nanowires. The material systems and 1D morphology have compelling applications in spintronics,[152] optoelectronics,[86] advanced energy storage and conversion[31,80] and catalysis.[88,30] Moreover, our findings provide insight into the precursor conversion rates and byproducts that support anisotropic crystal growth by solventless thermolysis.

4.3 Results and Discussion

4.3.1 Phase Controlled Synthesis of Co_9S_8 and Co Nanowires

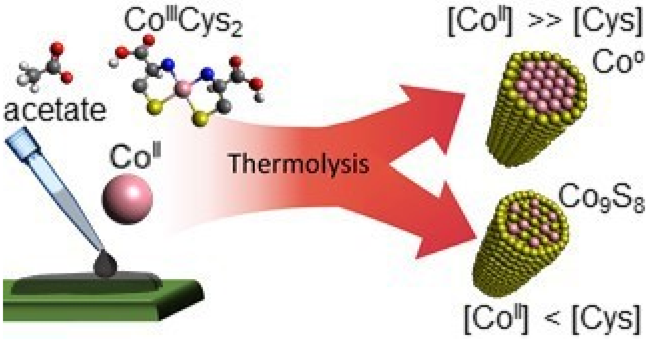

FIGURE 4.1: Schematic illustrating the precursors used in nanowire synthesis: Co^{II} acetate and Co^{III} bis-cysteinate, and the substrate preparation procedure. Following dropcasting and drying of the cobalt-complex solution; nanowire growth of the Co^0 and/or Co_9S_8 phase is achieve by annealing in high vacuum. Nanowire phase is determined by the Co^{II}:Cys mole ratio.

Commercially available cobalt(II) acetate tetrahydrate (Co^{II}) and L-cysteine (Cys) were employed as metal and sulfur sources for the growth of Co and Co_9S_8 nanowires. In a typical growth procedure, a solution containing the precursor compounds is dropcast onto a clean silicon substrate with a native oxide layer (Figure 4.1). After air-drying, the specimen is loaded into a high-vacuum annealing chamber and evacuated to a pressure of 2 x 10^{-7} mbar.

Precipitation of nanocrystals was not observed after dropcasting and drying of the precursor mixture. The sample was heated to a growth temperature at a rate of 2 – 3 °C/sec, and annealed before cooling to room temperature. The range of annealing temperatures for Co_9S_8/Co nanowire growth was 470 - 590 °C, and the total annealing time at this temperature was 1 hour (a typical plot of the temperature measured as a function of time during heat-up and growth is shown in Appendix A Figure A.1. The cysteine concentration in the precursor solution was kept constant at 9.0 ± 0.5 mM and the amount of cobalt(II) acetate was varied to achieve 0.5 - 13.0 (Co^{II}:Cys) mole ratios. We show that the nanowire phase can be tuned between pure cobalt (Co^0) and cobalt sulfide (Co_9S_8) by adjusting the relative concentration of the cobalt(III) bis-cysteinate complex and cobalt(II) acetate, which is achieved by varying the mole ratios of the cobalt(II) acetate and S (cysteine) reagents. Table 4.1 shows the precursor solutions with 0.9, 4.9 and 9.7 (Co^{II}:Cys) mole ratios and the respective pH and starting reagent masses (cobalt(II) acetate and cysteine).

TABLE 4.1: Co^{II}:Cys mole ratios, pH and reagent mass of nanowire precursor solutions.

Co^{II} : Cys		Mass (mg)	
Mole Ratio	pH	Co^{II} acetate	Cysteine
0.9	4.8	100	50
4.9	5.4	500	50
9.7	5.7	1000	50

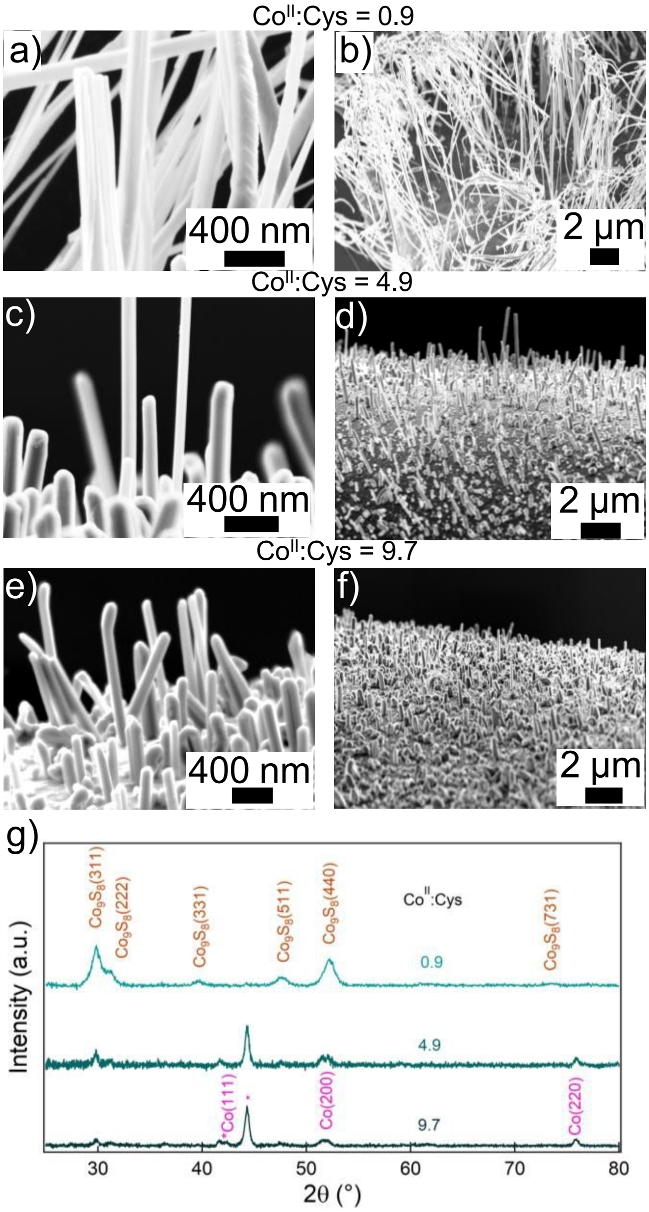

FIGURE 4.2: SEM images of Co_9S_8 and Co nanostructures grown from 0.9 (a and b), 4.9 (c and d) and 9.7 (e and f) (Co^{II}:Cys) mole ratio solutions. g) X-ray diffraction patterns of growth products from the three solutions.

Data obtained using nanowires from thermolysis of 0.9, 4.9 and 9.7 (Co^{II}:Cys) solutions at 590 $_{o}C$ are shown in Figure 4.2. Figure 4.2a and b show typical morphology of nanowires grown from a 0.9 (Co^{II}:Cys) solution, with the X-ray diffraction pattern (Figure 4.2g) matching face-centered cubic (FCC) Co_9S_8 (PDF 04-004-4525). Minor peak intensities were indexed to FCC Co^{o} (PDF 00-015-0806). The nanowires have a broad diameter distribution with a mean of 125 nm based on an analysis of 82 structures (Appendix A Figure A.2a). The variation in length was considerable with a number of nanowires extending over 20 μm with an aspect ratio > 400, the average was 5.4 μm (Appendix A Figure A.2b).

Nanowire morphologies from 4.9 and 9.7 solutions are shown in Figures 4.2c-d, and Figures 4.2e-f respectively. Characterization by X-ray powder diffraction shows the dominant phase to be FCC Co (PDF 00-015-0806) with a minor presence of FCC Co_9S_8 (Figure 4.2g). Nanowires and nanorods grown from a 4.9 mole ratio solution have a mean diameter of 130 nm based on an analysis of 47 structures (Appendix A Figure A.2a), with an average length of 1.6 μm (Appendix A Figure A.2b). X-ray diffraction patterns show the variation in abundance of FCC Co_9S_8 to FCC Co^O as the Co^{II}:Cys mole ratio is varied from 0.9 to 9.7 (Figure 4.2g). Interestingly thermolysis of a precursor solution containing cobalt(III) bis-cysteinate and cobalt(II) chloride (under identical precursor ratios to a 4.9 precursor solution) did not produce nanowires (under identical annealing conditions). Characterization of the thermolysis product is shown in Appendix A Figure A.3 and suggests the acetate counter anion is fundamentally important to nanowire growth possibly due to its role as a reducing agent, the oxidation product being carbon dioxide.

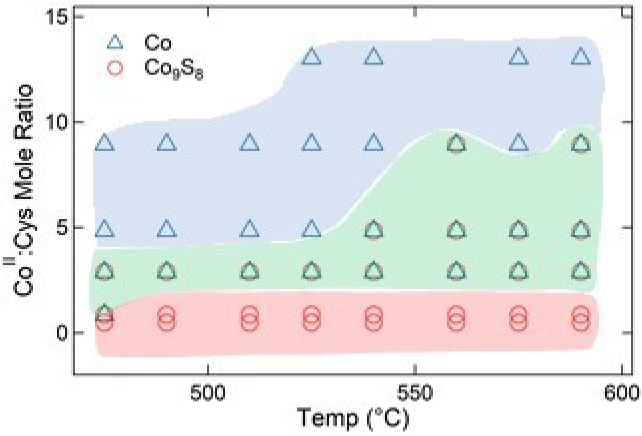

FIGURE 4.3: Nanowire phase table for Co and Co_9S_8 based on the Co^{II}:Cys mole fraction and annealing temperature. The highlighted blue region indicates the Co nanowire growth zone, the red region indicates Co_9S_8 nanowires and orange indicates nanowires of both phases.

A nanowire phase diagram (Figure 4.3) was constructed from thermolysis experiments of 0.5 - 13.0 (Co^{II}:Cys) precursor solutions at growth temperatures ranging from 470 - 590 °C. The phase was determined from a sample of individual nanowires characterized by energy dispersive X-ray spectroscopy (EDS). The blue highlighted region indicates that only cobalt nanowires were present, and the red Co_9S_8. The green region indicates that nanowires of both phases were present. Mole ratios lower than 0.9 (Co^{II}:Cys) produced Co_9S_8 nanowires in the temperature range studied; solutions with mole ratios between 2.89 - 4.85 produced relatively high yields of both phases, and solutions with a mole ratio greater than 9.0 resulted in almost exclusively FCC Co nanowires. In the mixed-phase region, Co nanowires typically have much lower aspect ratios than Co_9S_8.

4.3.2 Phase Determination by EDS

The nanowire phase (Co_9S_8 or Co) could be readily identified by EDS using the ratio of Co Lα and S Kα (Co/S) peak intensities. A comparative study of Co_9S_8 and Co nanowires analyzed directly on the growth substrate with nanowires transferred to minimize background contributions (Figures 4.4 and 4.5) strongly supports the phase determination technique. The results confirm the relative peak intensity is due to the nanowire composition and not background. To minimize background contributions nanowires were transferred onto a holey carbon TEM grid and housed on a specialized elevated Al stub holder inside the SEM. SEM, TEM and SAED characterization of nanowires from 0.5 and 9.0 (Co^{II}:Cys) solutions following annealing at the lower and upper temperature extremes further support phase determination by EDS analysis and suggest in the examined temperature window, both respective phases (FCC Co_9S_8 and FCC Co) remained unchanged. SEM, TEM and SAED characterization of nanowires grown from a 0.5 (Co^{II}:Cys) precursor solution annealed at the lower (490 °C) and upper (590 °C) temperatures are shown in Appendix A Figure A.4 and confirm FCC Co_9S_8 phase. Nanowire density at 470 °C annealing temperature was too low to successfully transferred to a TEM grid and was concluded to be the approximate temperature threshold to nanowire growth. Characterization of 1D materials from the 9.0 (Co^{II}:Cys) solution at both temperature extremes (470 and 590 °C) support the assignment to the Co FCC phase (Appendix A Figure A.5).

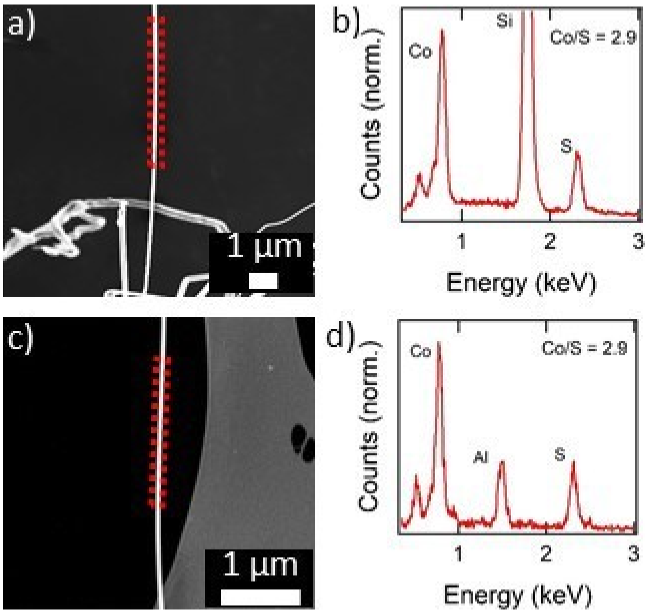

FIGURE 4.4: a) SEM image of a Co_9S_8 nanowire on the growth substrate with a red box indicating the EDS scan region. b) EDS spectrum taken from the nanowire in a) normalized to the Co Lα maximum. c) SEM image of a Co_9S_8 nanowire on a Cu TEM grid with holy carbon membrane. d) Normalized EDS spectrum of Co_9S_8 nanowire in c).

TABLE 4.2: Elemental composition of Co_9S_8 nanowires as determined from quantitative EDS

	Atomic %	
Figure	Co	S
4.4a	56	44
4.4c	58	52

Here the EDS spectral analysis to determine the nanowire phase is discussed. Figure 4.4a shows a Co_9S_8 nanowire grown by thermolysis of a 0.9 (Co^{II}:Cys) mole ratio solution on a Si substrate. The red box indicates the scan region. The EDS spectrum from the nanowire in Figure 4.4a is shown in 4.4b. The spectrum was normalized to the Co Lα peak and the Co Lα and S Kα peaks were fitted with a Guassian function to determine the relative intensity. The peak ratio (Co/S) for the Co_9S_8 nanowire was < 3. Figure 4.4c shows a Co_9S_8 nanowire transferred onto a TEM grid with a holey carbon membrane. The EDS analysis was done on a raised Al TEM grid holder to minimize background contributions. The peak ratio (Co/S) was shown to be approximately equivalent to the Co_9S_8 nanowire measured on the growth substrate. Elemental composition (atomic %) based on the EDS spectrum in Figure 4.4 are shown in Table 4.2.

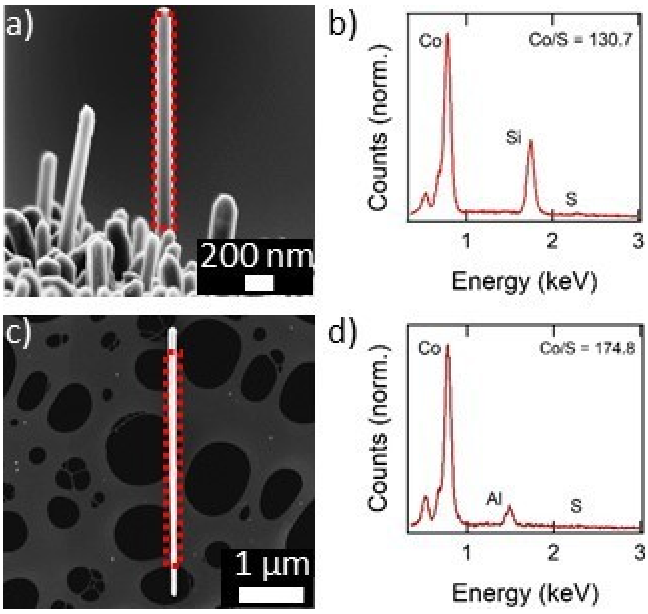

FIGURE 4.5: a) SEM image of a Co nanowire on the growth substrate with a red box indicating the EDS scan region. b) EDS spectrum taken from the nanowire in a) normalized to the Co Lα maximum. c) SEM image of a Co nanowire on a Cu TEM grid with holy carbon membrane. d) Normalized EDS spectrum of Co nanowire in c).

Figure 4.5a shows a Co nanowire grown by thermolysis of a 9.0 (Co^{II}:Cys) mole ratio solution and the scan region the EDS spectrum was collected (red box). Figure 4.5b shows the EDS spectrum taken from the nanowire in Figure 4.5a. The spectrum was normalized to the Co Lα peak and fit with a Guassian function. The peak ratio (Co/S) was calculated to be > 100 for the nanowire in Figure 4.5a and for the nanowire transferred onto a TEM grid in Figure 4.5c. The peak intensities in the EDS spectra are in good agreement and significantly different from the sulfide phase. Atomic percentage based on quantitative EDS for the spectra shown in Figure 4.5a and c are shown in Table 4.3.

TABLE 4.3: Elemental composition by quantitative EDS

	Atomic %	
Figure	Co	S
4.5a	97	3
4.5c	99	1

4.3.3 Nanowire Characterization and Growth Direction

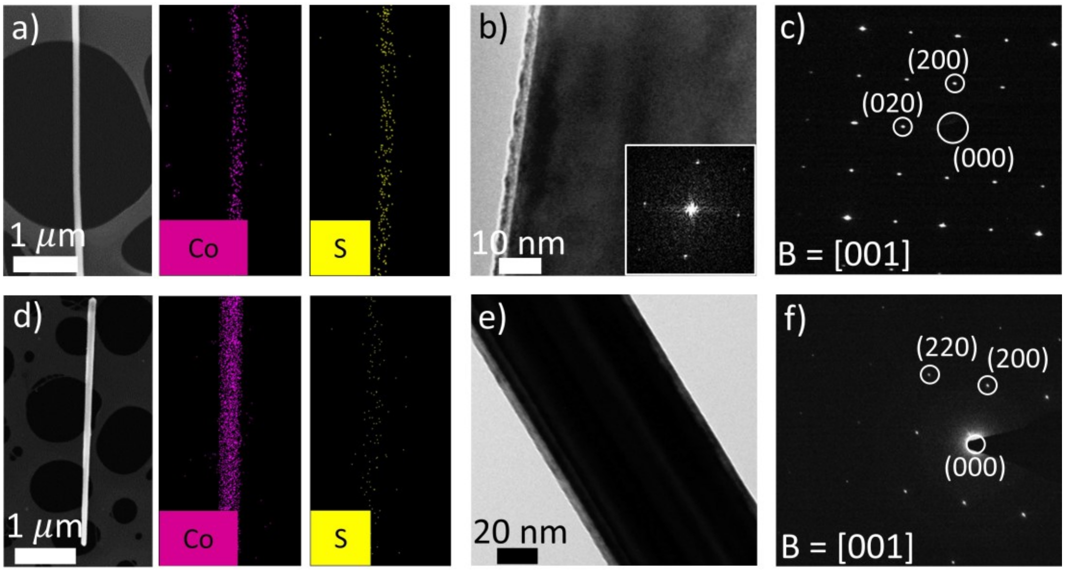

FIGURE 4.6: a) SEM image of a Co_9S_8 nanowire on a Cu TEM grid with a holey carbon membrane with cobalt and sulfur elemental maps using EDS. b) Lattice fringe resolved TEM image of a 60 nm Co_9S_8 nanowire with FFT (inset). c) SAED pattern from nanowire in b) resolved along the [001] zone axis. d) SEM image with cobalt and sulfur elemental maps of a Co nanowire. e) TEM image of a 80 nm diameter nanowire with f) SAED resolved along the [001] zone axis.

Characterization of isolated Co_9S_8 and Co nanowires from starting 0.9 and 4.9 (Co^{II}:Cys) mole ratio solutions (respectively) is shown in Figure 4.6. The nanowires are high quality, single crystal structures with smooth surfaces and negligible presence of structural defects such as stacking faults. A Co_9S_8 nanowire transferred onto a Cu TEM grid with a supportive carbon membrane is shown in the SEM image in Figure 4.6a. The TEM grid was housed on an elevated Al TEM grid holder sitting on the SEM stage to minimize background contributions to the X-ray signal. Compositional analysis by EDS confirmed the presence of both Co and S in the 100 nm diameter nanowire (Figure 4.6a). TEM characterization of a 60 nm Co_9S_8 nanowire and the corresponding FFT is shown in Figure 4.6b. The nanowire is shown to have a well-defined, smooth edge with the presence of a 3 - 4 nm capping layer surrounding the nanowire. The selected area electron diffraction (SAED) pattern of the same nanowire is shown in Figure 4.6c. Characterization by SAED shows the nanowire to be single-crystal. The SAED pattern was indexed as the FCC $Fm\bar{3}m$ space group using the Co_9S_8 parameters. The zone axis is [001] (Figure 4.6c). The {200} plane spacing was measured to be 4.8 Å in agreement with Co_9S_8 ($d_{\{200\}}$ = 4.964 Å). The nanowire growth direction was determined to be <100> by the FFT and the shape factor induced streaking of the SAED pattern.[44]

SEM characterization of a 100 nm diameter Co nanowire, along with EDS elemental mapping of Co and S is shown in Figure 4.6d. The S signal shows much lower relative counts (compared with the Co_9S_8 nanowire) and is attributed to the capping layer surrounding the Co nanowire. This 3 - 4 nm layer can be seen in the high resolution TEM image (Figure 4.6e) of a 80 nm diameter Co nanowire. The SAED pattern (Figure 4.6f) taken from the nanowire in Figure 4.6e was resolved along the [001] zone axis, and the {200} plane spacing was measured to be 1.72 Å in agreement with FCC Co ($d_{\{200\}}$ = 1.772 Å). Nanowire growth was determined to be in the <110> direction. Growth direction was determined by the shape factor induced streaking of the diffraction intensity spots and correlated by the shadow imaging technique demonstrated in Figure 4.7.

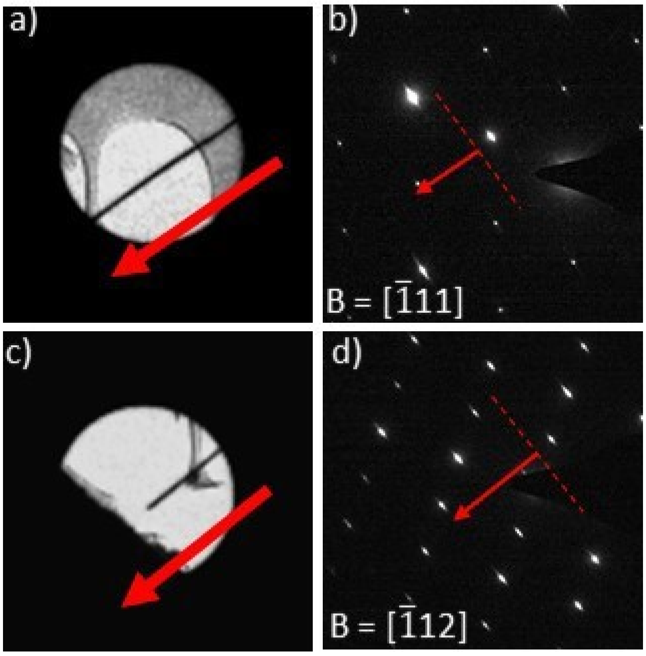

FIGURE 4.7: a) Shadow image of a Co_9S_8 nanowire captured in diffraction mode. b) SAED pattern from nanowire in a) captured with the same camera length. c) Shadow image of a second Co_9S_8 nanowire captured in diffraction mode with the corresponding d) SAED pattern.

The nanowire growth direction can be determined using TEM and SAED characterization.[44] Magnetic lenses cause a rotation between the analyzed object and its image due to the Lorentz force.[142] This also has the effect of generating a rotation between the recorded bright field image and the SAED pattern due to the different optical modes.[44] Therefore the nanowire growth direction cannot simply be inferred by overlaying the SAED pattern with the brightfield image without understanding the rotation between the two images. By aligning the nanowire growth direction perpendicular to the electron beam axis the sharp edge of the nanowire induces a streaking in the diffraction intensity spots along a direction perpendicular to the nanowire growth axis.[44] From this the nanowire growth direction can be determined. We confirm this result by comparing the SAED pattern with the shadow image of the nanowire recorded in diffraction mode (under identical camera lengths). Figure 4.7a shows the recorded shadow image captured in diffraction mode of a Co_9S_8 nanowire (diameter = 70 nm) and Figure 4.7b shows the corresponding SAED pattern of the nanowire. The nanowire growth axis, as highlighted by the red arrow, was determined by the streaking effect and confirmed by comparing with the shadow image. Identical characterization was done on a second nanowire and a different zone axis ([-112]) as shown in Figures 4.7c and d. The nanowire growth axis is again shown to be perpendicular to the elongation in the diffraction intensity spots, justifying the technique used to deduce the growth axis.

4.3.4 Direct Observation of Nanowire Growth by FESEM

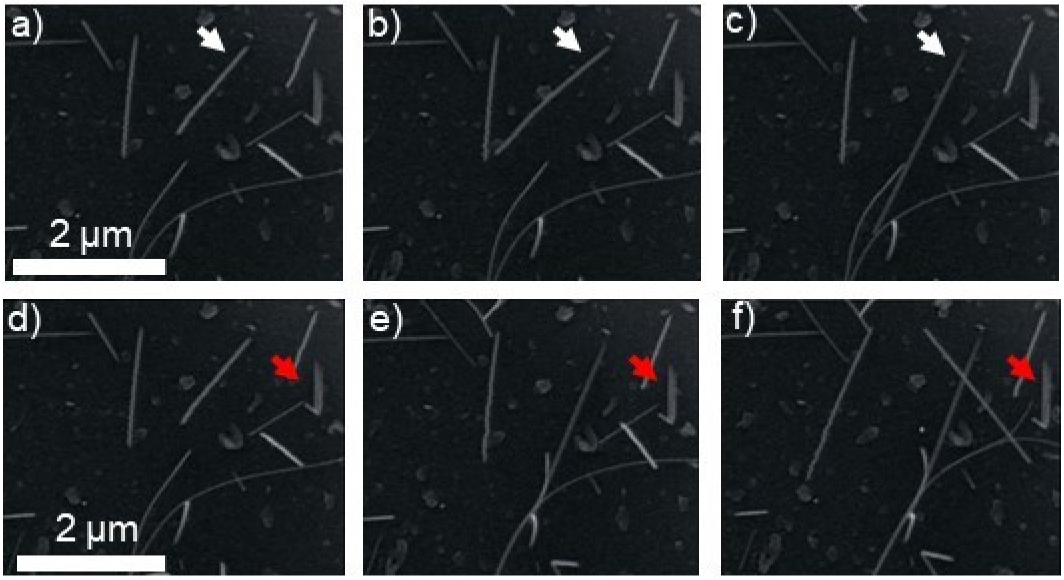

FIGURE 4.8: Time-dependent nanowire evolution during growth using FESEM characterization. a) - c) Growth sequence of an isolated nanowire (indicated by the white arrow). Images were captured over a 95 second period. d) – f) Growth sequence of a second Co_9S_8 nanowire with a disfigured tip (indicated by a red arrow). Images were captured over a 10 minute period.

Real-time characterization during nanocrystal growth by electron microscopy techniques (SEM and TEM) has led to significant breakthroughs in fundamental understanding. Advances include observation of multistep nucleation pathways, measured nanowire growth kinetics, observation of layer-by layer growth in nanowires and morphological changes owing to catalyst migration (VLS growth).[134,91,104,239,78] However slow progress has been made as typical reaction conditions are inherently incompatible with high resolution imaging conditions (i.e. wet environments, elevated pressures, and high temperatures). Electron microscopy studies of nanocrystal growth by solventless thermolysis overcome many of the challenges presented with growth from solution or vapor phase precursors. Time-dependent FESEM characterization during nanowire growth was achieved using a home-built, custom stage and is shown in Figure 4.8. Growth was achieved using a 0.9 (Co^{II}:Cys) precursor solution and the substrate preparation procedure outlined in the experimental section. FESEM characterization was performed at a stabilized temperature (540 °C) under high vacuum (9 x 10^{-6} mbar). Both pressure and temperature were monitored and recorded during annealing. The high temperatures required for growth resulted in significant thermal drift which requires constant stage corrections. Images were captured at a constant magnification. The growth sequence of the two nanowires are shown in Figure 4.8a – c and Figures 4.8d – f respectively. Nanowires are shown to grow directly from the residual precursor film at the stabilized growth temperature. The result confirms nanowire growth at a stabilized temperature and not during cool down (or only during heat-up). Based on the characterization of the nanowire in Figures 4.8d – f the unique shape of the tip supports the proposal that adatoms are incorporated into the nanowire below the film surface. Analogous to a base-driven growth mechanism. A time-dependent sequence is shown in Appendix Aa Figure A.6 to support this conclusion (captured under identical conditions).

4.3.5 Ni and Ni_3S_2 Nanowire Growth and Characterization

FIGURE 4.9: Schematic illustrating the precursors used in nanowire synthesis: Ni^{II} acetate and Ni^{II} bis-cysteinate, and the substrate preparation procure. H_2O_2 was added to the Ni^{II} acetate and Ni^{II} bis-cysteinate precursor solution to achieve Ni_3S_2 nanowire growth. Following dropcasting and drying of the nickel-complex solution; nanowire growth of the Ni^0 and/or Ni_3S_2 phase is achieve by annealing in high vacuum.

Similar to the Co_9S_8/Co system precursor solutions for the growth of Ni_3S_2 and Ni nanowires were prepared using commercially available nickel(II) acetate tetrahydrate and L-cysteine. Following dropcasting and drying (Figure 4.9), precursor compounds were annealed in high vacuum (10^{-7} mbar) for 5 hours at 415 ± 10 °C. The annealing profile including the heating rate (2 - 3 °C/sec) is shown in Appendix A Figure A.1. The cysteine concentration in the precursor solution was kept constant at 9.0 ± 0.5 mM and the amount of nickel(II) acetate was varied to achieve 1.0, 3.9 and 4.9 (Ni^{II}:Cys) mole ratio solutions. Precursor species for the growth of nickel nanowires are evidenced to be nickel(II) acetate and nickel(II) bis-cysteinate. Oxidation of the precursor solution was required for nanowire growth of the Ni_3S_2 phase. To achieve this 30% w/w H_2O_2 was added to a 1.0 (Ni^{II}:Cys) precursor solution. Table 4.4 shows the precursor solutions with 1.0, 3.9 and 4.9 (Ni^{II}:Cys) mole ratios and the respective pH and starting reagent masses (nickel(II) acetate and cysteine).

TABLE 4.4: Ni^{II}:Cys mole ratios, pH and reagent mass of nanowire precursor solutions.

Ni^{II} : Cys		Mass (mg)	
Mole Ratio	pH	Ni^{II} acetate	Cysteine
1.0	4.5	100	50
3.9	5.0	400	50
4.9	5.0	500	50

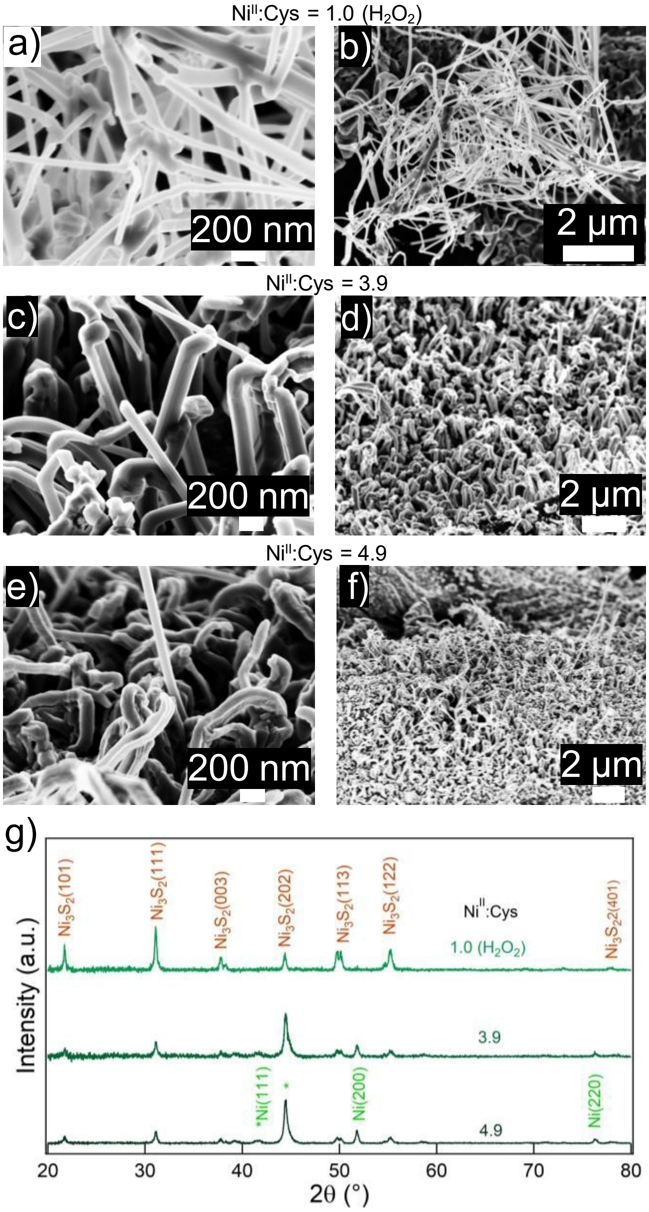

FIGURE 4.10: SEM images of Ni_3S_2 and Ni nanostructures grown from starting 1.0 (a and b), 3.9 (c and d) and 4.9 (e and f) (Ni^{II}:Cys) mole ratio solutions. g) Powder X-ray diffraction patterns of the nanostructures.

Figures 4.10a and b show SEM images of nanowires grown by thermolysis of a 1.0 (Ni^{II}:Cys) mole ratio solution. X-ray diffraction characterization confirms the rhombohedral Ni_3S_2 (PDF 04-008-8458) phase (Figure 4.10g). Ni_3S_2 nanowires were obtained only after an oxidant was added to the precursor solution, here we added 30% w/w H_2O_2. The resultant nanowires and nanorods had an average diameter of 66 nm based on an analysis of 59 structures (Appendix A Figure A.7). Nanostructures grown from a 3.9 (Ni^{II}:Cys) solution are shown in Figures 4.10c and d, the resultant nanowires have an average diameter of 100 nm based on an analysis of 32 structures (Appendix A Figure A.6). The dominant phase is shown to be FCC Ni^0 (PDF 04-010-6148) with minor presence of Ni_3S_2 (Figure 4.10g). Thermolysis of the 4.9 (Ni^{II}:Cys) solution resulted in nanostructures of the lowest aspect ratio (Figures 4.10e and f), XRD confirmed the dominant phase is FCC Ni^{o} with negligible presence of Ni_3S_2 (Figure 4.10g). The presence of Ni_3S_2 is attributed to atmospheric oxidation of the dropcast and dried precursor solution.

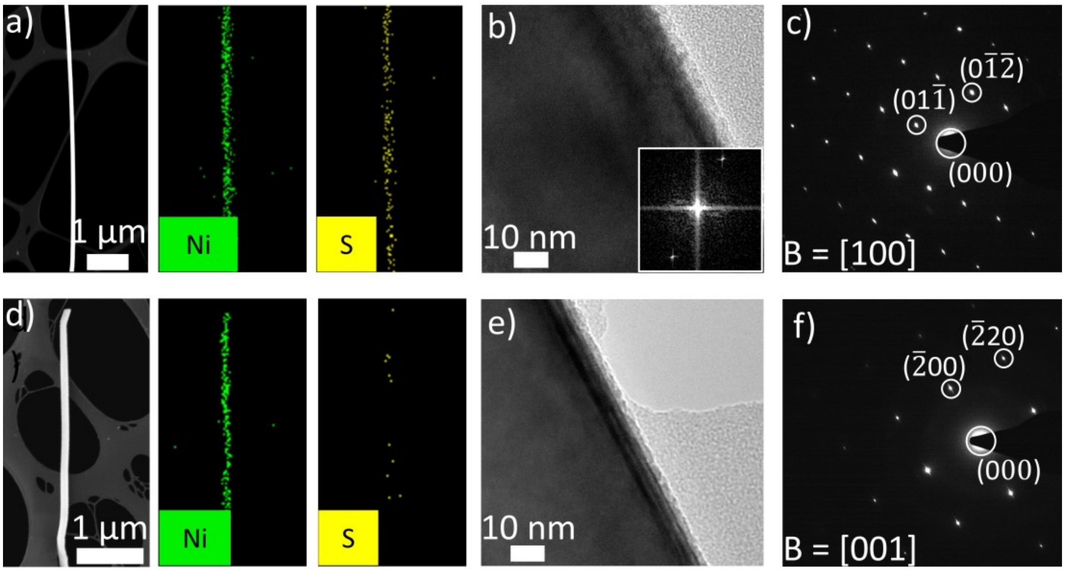

FIGURE 4.11: a) SEM image of a Ni_3S_2 nanowire on a supportive holey carbon membrane with nickel and sulfur elemental maps using EDS. b) Lattice fringe resolved TEM image of a 80 nm Ni_3S_2 nanowire with FFT (inset). c) SAED pattern of nanowire in b) resolved along the [100] zone axis. d) SEM image of an isolated Ni nanowire (100 nm in diameter) with Ni and S elemental maps shown in green and yellow (respectively). e) TEM image of a 110 nm diameter nanowire with f) SAED resolved along the [001] zone axis.

SEM characterization of a Ni_3S_2 nanowire transferred onto a Cu TEM grid with a holey carbon membrane is shown in Figure 4.11a. The elemental maps using EDS confirm high concentrations of both Ni and S (shown in green and yellow respectively). Figure 4.11b shows a TEM image of an isolated Ni_3S_2 nanowire approximately 80 nm in diameter. The lattice fringe resolved image shows the nanowire to be single-crystal with a capping layer. A FFT of the nanowire lattice is shown in the inset. The SAED pattern can be indexed as the rhombohedral R32 space group using the Ni_3S_2 parameters (Figure 4.11c). The zone axis is [100], and the {110} plane spacing was measured to be 3.95 Å which is in good agreement with theoretical values for rhombohedral Ni_3S_2 ($d_{\{110\}}$ = 4.081 Å). A SEM image and elemental EDS maps for Ni and

S are shown in Figure 4.11d for a 110 nm diameter Ni nanowire. HRTEM (Figure 4.11e) and SAED (Figure 4.11f) show the nanowire to be single-crystal FCC cubic; the lattice spacings of the {200} planes (3.35 Å) were in agreement with FCC Ni ($d_{\{200\}}$ = 3.524 Å). The presence of a thin capping layer is also observed.

4.3.6 Precursor Characterization

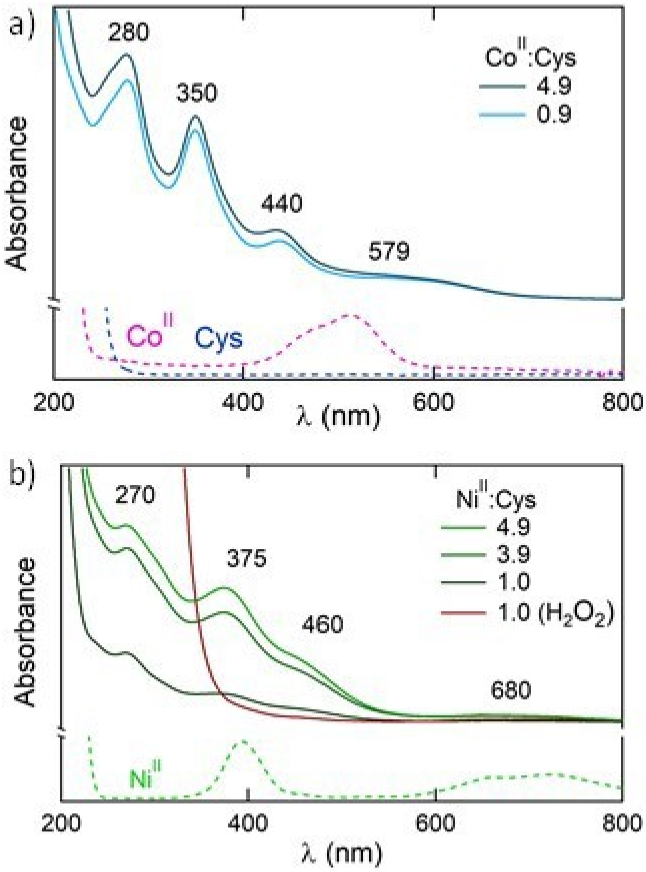

FIGURE 4.12: a) UV-vis absorbance spectra for 0.9 and 4.9 (Co^{II}:Cys) mole ratio solutions. Reference Co^{II} acetate (4.3 mM) and cysteine (8.8 mM) aqueous solutions are also included. b) UV-vis absorbance spectra for 1.0, 3.9 and 4.9 (Ni^{II}:Cys) mole ratio solutions including aqueous Ni^{II} acetate (40.2 mM).

Addition of cysteine to cobalt(II) salts forms a cobalt(III) bis-cysteinate complex.[154] The UV-vis absorbance spectra of the 0.9 and 4.9 (Co^{II}:Cys) precursor solutions (Figure 4.12a) show identical absorbance bands to the isolated complex (Appendix A Figure A.8a); the multiple band at 515 nm due to the cobalt(II) acetate is not observed as it is of low intensity (ϵ = 4.6 $M^{-1}cm^{-1}$) and obscured by the precursor complex. The identical absorbance maximum in each of the precursor solutions indicates that the inner coordination sphere of the cobalt complex remains unchanged with varying Co^{II}:Cys ratios. Characterization of the isolated cobalt-cysteine complex by UV-vis absorbance (Appendix A Figure A.8a) and FTIR (Figure 4.14) confirms octahedral coordination geometry with cysteine acting as a bidentate ligand via S- and N-donors to the Co^{III} center (see Appendix A for further discussion).[121,162,154] High-resolution mass spectrometry of the isolated cobalt complex shows an isotope distribution pattern with a maximum intensity at m/z = 298.9580. Modelling of this distribution produces an excellent fit for a molecular formula of $[CoC_6H_{12}N_2O_4S_2]^+$, with a mass deviation of 5ppm, confirming that the solution-state inner coordination sphere of the nanowire precursor contains one Co^{III} and two cysteine units (cobalt(III) bis-cysteinate). The oxidation of cobalt(II) (in cobalt acetate) to cobalt(III) in the complex is attributed to exposure of the solution to atmospheric oxygen; the associated color change can be slowed by degassing using N_2 (Figure 4.13).

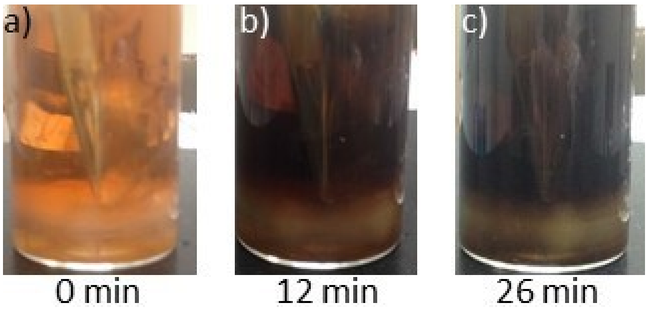

FIGURE 4.13: Optical images of the color change of a 4.9 Co^{II}:Cys solution under constant degassing by bubbling of N_2. a) Image taken immediately after the Co^{II} acetate solution was mixed into the cysteine solution, b) 12 minutes after continuous bubbling with N_2 and c) 26 minutes after continuous bubbling.

By mixing a cobalt(II) acetate (67 mM) aqueous solution into a constantly degassing aqueous solution of cysteine (21 mM) the change in solution color upon exposure to atmosphere is demonstrated. Both cobalt(II) acetate and cysteine had been degassed prior to mixing by bubbling N_2 for 30 minutes. The color change is shown in Figure 4.13. Immediately after mixing the solution color was orange/red (Figure 4.13a) then through continued exposure to atmosphere the solution color turned to dark green/brown (Figure 4.13c). Studies on the oxidation of cobalt-cysteine complexes have reported a similar color change on exposure to atmosphere.[189,154,18]

UV-vis absorbance spectra for the 1.0, 3.9 and 4.9 Ni^{II}:Cys precursor solutions confirm the square planar d8 nickel(II) complexes in all solutions, and are in agreement with the solid state structure of $Ni^{II}Cys_2$ (Figure 4.12b).[7]

The nickel(II) acetate bands expected at 395 (ϵ = 5.0 $M^{-1}cm^{-1}$), and 724 nm (ϵ = 2.0 $M^{-1}cm^{-1}$) due to $Ni(H_2O)_6{}^{2+}$ were not observed in the nanowire precursor solutions due to their low intensity. The precursor product in the 1.0 (Ni^{II}:Cys) mole ratio solution could not be unambiguously identified following the addition of H_2O_2. The FTIR spectrum of the isolated nickel-cysteine product (Figure 4.14) shows bands similar to those of the $[Co^{III}Cys_2(H_2O)_2]$ spectrum (see Appendix A for further discussion).

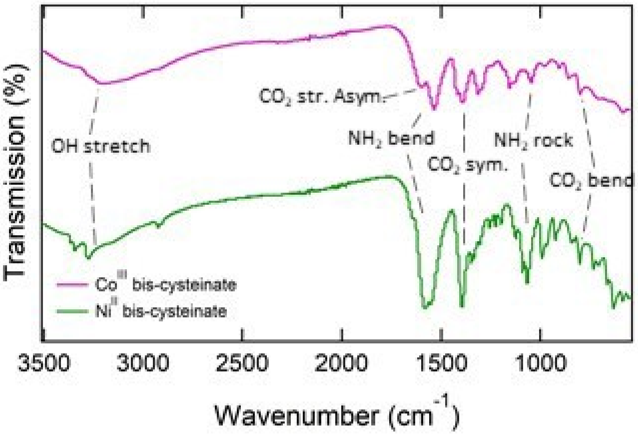

FIGURE 4.14: FTIR spectrum of isolated Co^{III} bis-cysteinate (top) and Ni^{II} bis-cysteinate (bottom).

4.3.7 Precursor Reactivity and Decomposition Products

Thermogravimetric analysis (TGA) of the isolated precursor compound cobalt(III) bis-cysteinate ($[Co^{III}Cys_2(H_2O)_2]$) and a mixture containing cobalt(III) bis-cysteinate and cobalt(II) acetate is shown in Figure 4.15. Importantly, cobalt(II) acetate does not cause a temperature change in the major mass loss event. The compound mixture was prepared by mixing isolated cobalt(III) bis-cysteinate with cobalt(II) acetate tetrahydrate in a 1:1 mole ratio, which is an equivalent precursor ratio to the 0.9 (Co^{II}:Cys) mole ratio solution. Side-by-side comparison of the mass loss during thermogravimetric analysis for $[Co^{III}Cys_2(H_2O)_2]$ and $[Co^{III}Cys_2(H_2O)_2]/[Co^{II}OAc_2(H_2O)_4]$ TGA analysis is shown in Figure 4.15. The inset shows the mass loss curves normalized at 220 °C.

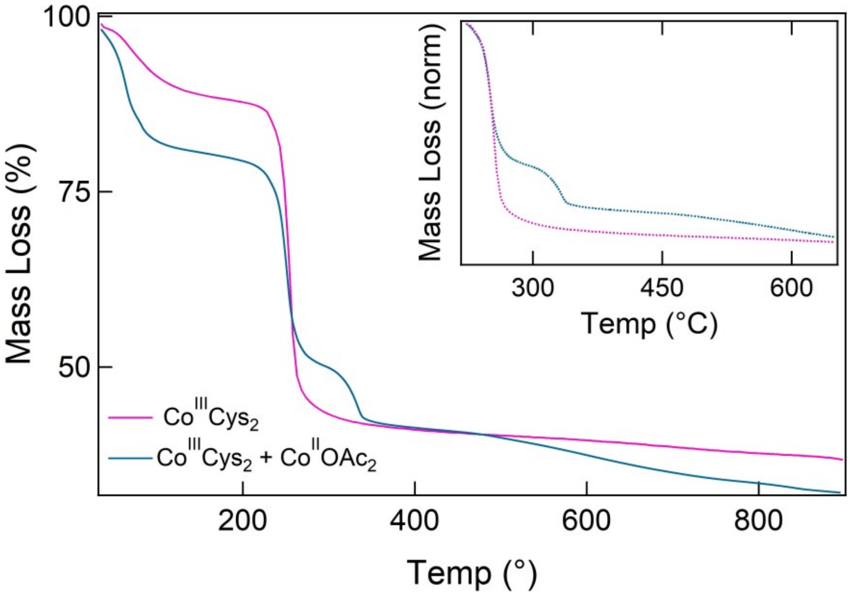

FIGURE 4.15: TG analysis of [Co^{III}Cys$_2$(H$_2$O)$_2$] and [Co^{III}Cys$_2$(H$_2$O)$_2$] + [Co^{II}OAc$_2$(H$_2$O)$_4$] precursor compounds. Normalized TG curve of both compounds at 220 °C (Inset).

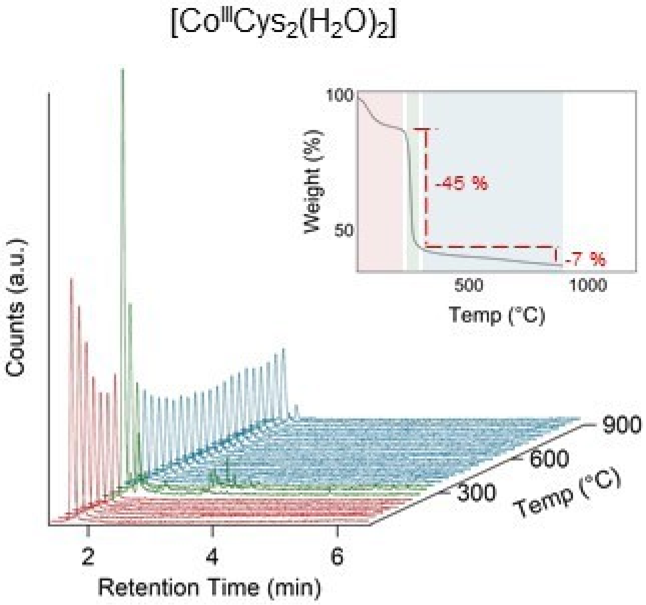

FIGURE 4.16: Total ion chromatographs taken every 30 °C between 30 – 900 °C, the heating rate was 3 °C/min for [Co^{III}Cys$_2$(H$_2$O)$_2$]. (inset) Thermogravimetric data for the isolated [Co^{III}Cys$_2$(H$_2$O)$_2$].

No nanowire growth was observed upon decomposition of only metal(II) acetate, in agreement with prior reports.[238,145,93,72,42] Therefore the decomposition rates and reaction-steps of the metal-cysteine complex were examined. TGA-GC-MS of the isolated [Co^{III}Cys$_2$(H$_2$O)$_2$] complex (Figure 4.16), shows that the coordinated cysteine is thermally stable to 180 °C before the onset of ligand decomposition, which occurs in a three-step process. The first process occurs between 30 to 180°C (DTGmax = 68 °C), with a mass loss of 10.2% attributed to the loss of coordinated water (Calc: 8.4%) and some residual moisture to produce anhydrous cobalt(III) bis-cysteinate. The temperature resolved extracted ion chromatographs for m/z = 18 (Figure 4.21a) are in excellent agreement with the thermogravimetry, showing water present only between 30 and 180 °C with local maxima at 60 and 90 °C attributed to unbound water and coordinated water, respectively.

The next process occurs between 180 to 240 °C (DTGmax = 233 °C), with a mass loss of 5.3% attributed to the loss of carbon dioxide from the acetate anion (Calc: 10.3%). The mass discrepancy is due to an overlap between two thermal events; the loss of CO_2 from acetate and the loss of cysteine ligand moieties. The temperature resolved extracted ion chromatographs for m/z = 44 (Figure 4.21c) are in excellent agreement with the thermogravimetry, showing carbon dioxide being present only between 180 and 240 °C with maximum abundance at 240 °C, correlating to the DTGmax of the acetate decomposition. The TGA suggests that after acetate decomposition, the charged $[Co(Cys)_2]^+$ species is produced as an intermediate, which spontaneously dissociates in the 240 to 300 °C range with a mass loss of 39.6% (DTGmax = 256 °C) to yield an unknown mixture of Co_xS_y. There is no further loss of volatile species attributed to decomposition of the Co(Cys) complex beyond 300 °C (Figure 4.16).

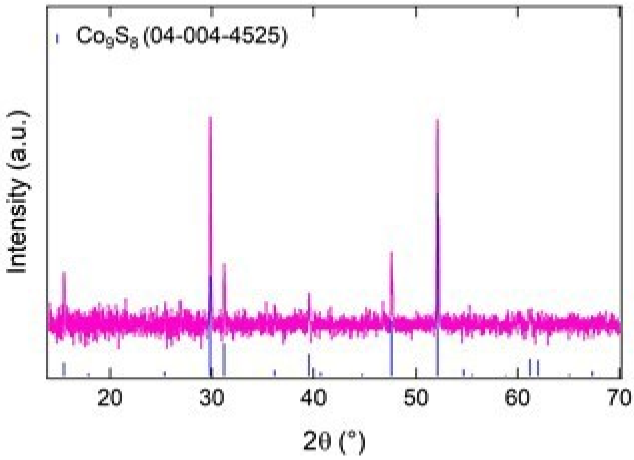

FIGURE 4.17: Powder X-ray diffraction pattern of Co^{III} bis-cysteinate TGA-GC-MS residue after heating to 900 °C.

The final process involves the steady loss of sulfur between 300 to 900 °C from the intermediate Co_xS_y residue remaining after 300 °C, to yield a final product of Co_9S_8 as determined by powder XRD of the TGA residue (Figure 4.17). The loss of sulfur is observed as sulfur dioxide due to gas phase reactions between sulfur and residual oxygen, and is the only volatile species produced beyond 300 °C (Figure 4.16 and Figure 4.21e).

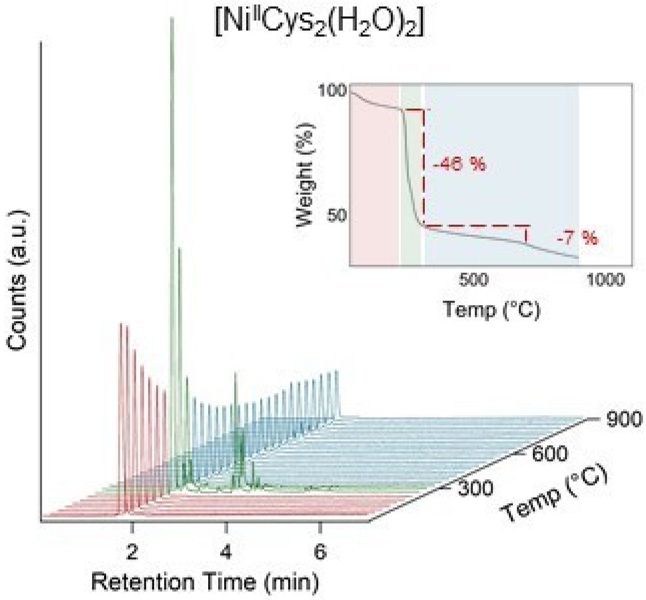

FIGURE 4.18: Total ion chromatographs taken every 30 ^{o}C between 30 – 900 ^{o}C, the heating rate was 3 ^{o}C/min for $[Ni^{II}Cys_2(H_2O)_2]$. (inset) Thermogravimetric data for the isolated $[Ni^{II}Cys_2(H_2O)_2]$.

TGA-GC-MS of nickel(II) bis-cysteinate (Figure 4.18) reveals similar thermal behavior to that of cobalt(III) bis-cysteinate. The complex is thermally stable to 180 ^{o}C before the onset of ligand decomposition which occurs in a two-step process. In contrast to the decomposition of cobalt(III) bis-cysteinate, there is no other mass loss due to carbon dioxide, which is attributed to the lack of acetate anions within the neutral nickel(II) bis-cysteinate complex. Between 220 and 290 ^{o}C the approximate 45% mass loss event is attributed to decarboxylation of the cysteine ligands followed by N- and S-containing heterocyclic species to form intermediate Ni_xS_y residue. Finally, there is a loss of sulfur above 300 ^{o}C (Figure 4.21f) to yield a final product of non-stoichiometric $Ni_3S_{1.783}$ as determined using XRD, Figure 4.19. A side-by-side comparison of the temperature resolved extracted ion chromatographs for m/z = 18, 44 and 64 are shown in Figure 4.21 for cobalt and nickel-cysteine complexes ($[Co^{III}Cys_2(H_2O)_2]$ and $[Ni^{II}Cys_2(H_2O)_2]$).

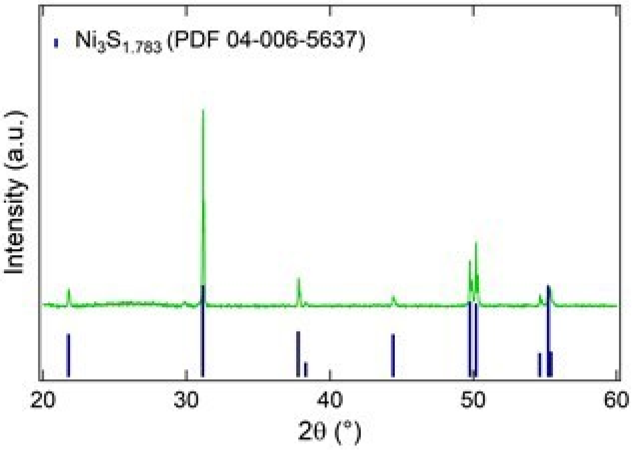

FIGURE 4.19: Powder X-ray diffraction pattern of Ni^{II} bis-cysteinate TGA-GC-MS residue after heating to 900 °C.

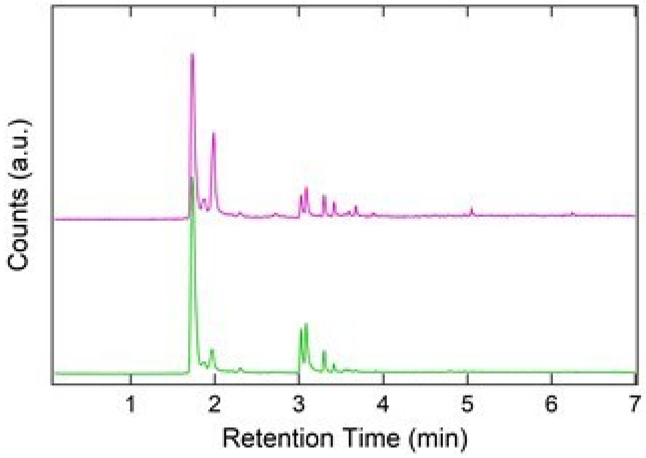

FIGURE 4.20: Gas chromatograms of the thermolysis products at 270 °C for Co^{III} bis-cysteinate (top) and Ni^{II} bis-cysteinate (bottom).

Total ion chromatographs of the volatile species for both $[Co^{III}Cys_2(H_2O)_2]$ and $[Ni^{II}Cys_2(H_2O)_2]$ shortly following the main decomposition step show a mixture of sulfurous and nitrogenous heterocyclic species, water and carbon dioxide (Figure 4.20). Of these species, thiophene (Rt = 2:301 min), 2-methyl-thiazole (Rt = 3:020 min), 2-methyl-pyridine (Rt = 3:092 min), 3-acetamido-pyrrolidine (Rt = 3:292 min) and 2-methyl-2-thiazole were unambiguously assigned. The presence of these species is in agreement with the literature for thermal decomposition of cysteine at temperatures above 200 °C.[255] The absence of ammonia, and presence of heterocyclic nitrogenous compounds in the chromatographs strongly suggests that there was no cleavage of the C-N bond within the cysteine moieties. The presence of these heterocyclic species can be explained by intra-molecular civilization of intermediate immonium ions formed by cleavage of the CH – C = O bond within the cysteine ligand.[114,184] Similarly, the presence of CO_2 and water is attributed to the decarboxylation of the amide moiety in the cysteine ligands. It can be inferred that a very similar thermal decomposition process is occurring during the thermolysis of these two precursors, given the similarity of the volatile species produced.

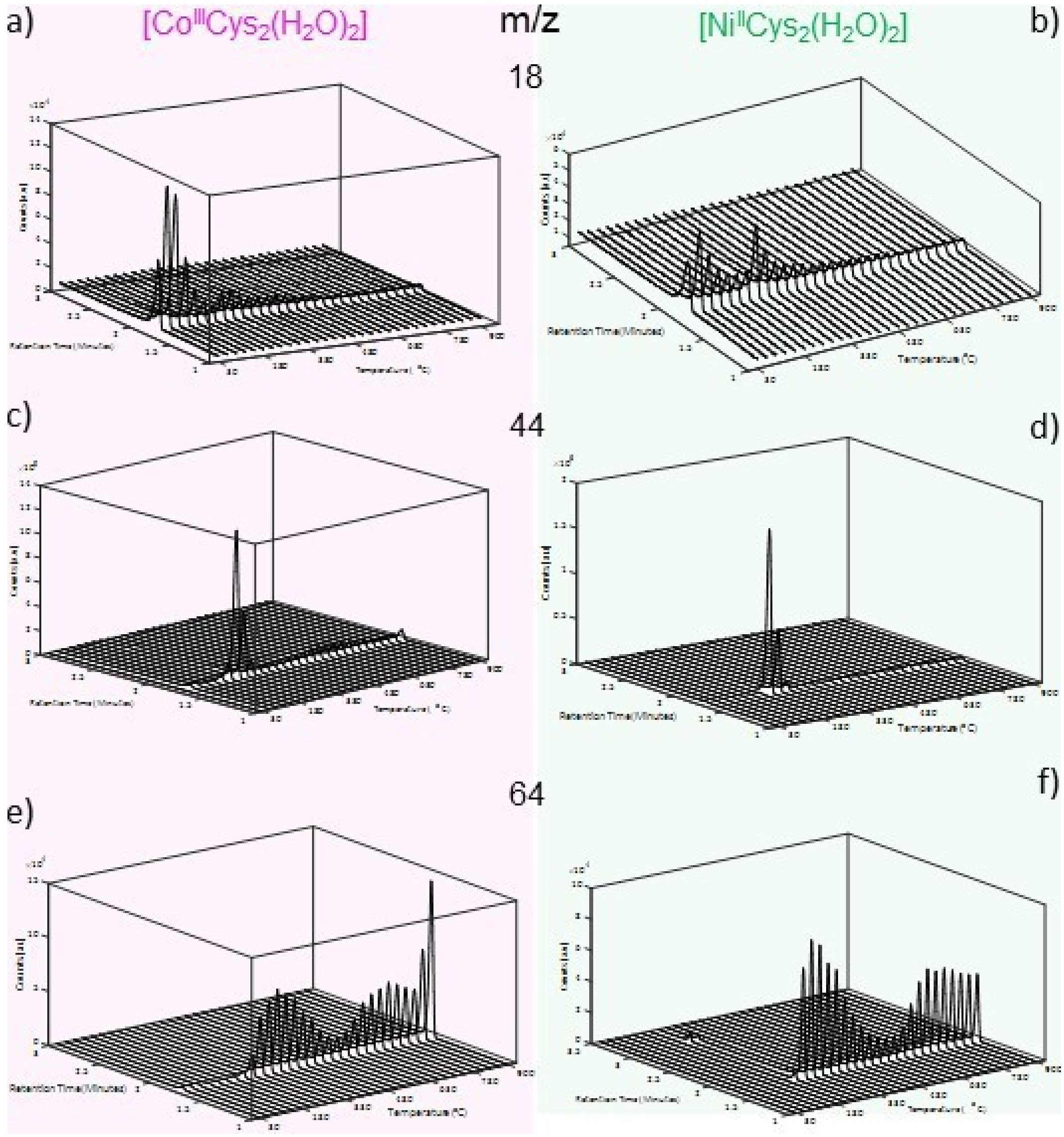

FIGURE 4.21: Extracted ion chromatographs for cobalt(III) bis-cysteinate and nickel(II) bis-cysteinate for m/z = 18 (a and b), m/z = 44 (c and d) and m/z = 64 (e and f).

4.3.8 Thermolysis Study of cobalt(III) dithiocarbamate

Thermolysis of a mixture containing the cobalt(III) complex: cobalt(III) dithiocarbamate ($[Co^{III}DIP]$) and cobalt(II) acetate under identical conditions forms nanocrystalline Co_9S_8. Examination of the two complexes (cobalt(III) dithiocarbamate and cobalt(III) bis-cysteinate) provides insight into the role of precursor chemistry in determining nanocrystal composition, morphology and concentration. TGA and DSC show cobalt(III) dithiocarbamate experiences similar decomposition steps including rapid mass loss at $\sim$ 300 °C followed by steady mass loss in the temperature range 300 - 900 °C. TGA-GC-MS characterization of the precursor compound mixture containing cobalt(III) dithiocarbamate and cobalt(II) acetate further shows the slow generation of carbon dioxide, sulfur dioxide and isopropyl isothiocyanate following the main mass loss step. This is in contrast to the precursor compound mixture containing cobalt(III) bis-cysteinate and cobalt(II) acetate which only shows the loss of carbon dioxide and sulfur dioxide (between 300 - 900 °C). Only Co and S remain following the main mass loss step of cobalt(III) bis-cysteinate, whilst in the cobalt(III) dithiocarbamate the remaining moiety contains organic material, S and N. The existence of which provides an added energy barrier to the generation of available monomer. The slow rate of precursor disassociation to generate available monomer is known to produce large nanocrystals through Ostwald Ripening with a broad size distribution.[51]

A 4mM cobalt(III) dithiocarbamate precursor solution was prepared. To that sufficient cobalt(II) acetate was added to yield a cobalt(III) dithiocarbamate/cobalt(II) acetate mole ratio equivalent to cobalt(III) bis-cysteinate to cobalt(II) acetate in a 1.0 (Co^{II}:Cys) mole ratio solution. Cobalt(III) dithiocarbamate was prepared according to the procedure outlined by Thorn *et al.*[212,81] The $[Co^{III}DIP]/[Co^{II}(OAc)_2(H_2O)_4]$ solution was dropcast and dried onto a heated Si substrate and loaded into the high vacuum annealing chamber. The substrate preparation and annealing procedure was identical to the Co_9S_8 nanowire work. Following annealing at 575 °C in high vacuum for 1 hour the substrate was cooled and removed for characterization.

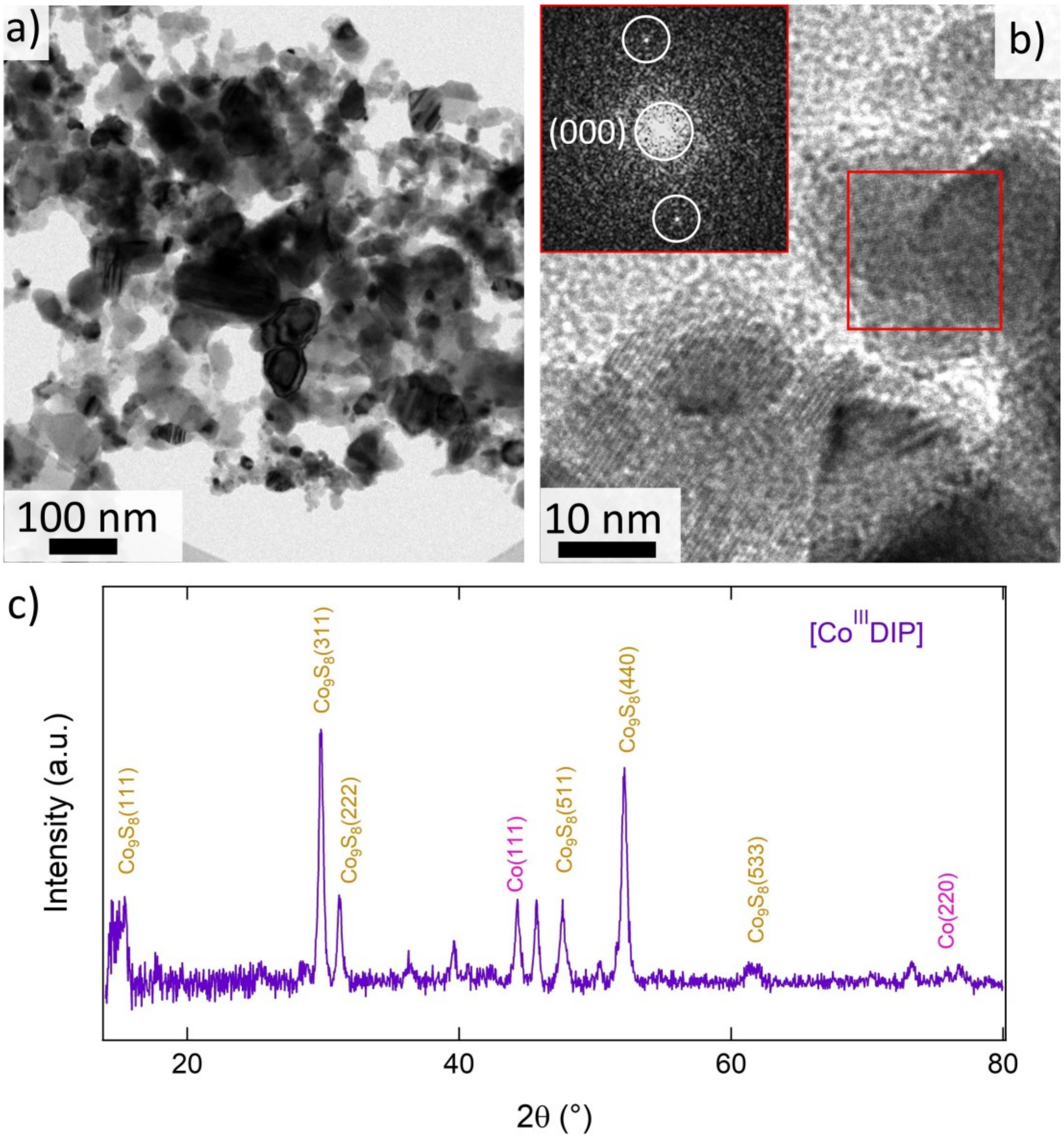

FIGURE 4.22: a) TEM image of the thermolysis product from a [Co^{III}DIP]/[Co^{II}(OAc)$_2$(H$_2$O)$_4$] precursor solution. b) High-resolution TEM image with FFT (inset). c) XRD analysis of growth substrate.

Characterization of the thermolysis product from the [Co^{III}DIP]/[Co^{II}(OAc)$_2$(H$_2$O)$_4$] precursor solution produced Co_9S_8 nanocrystals. TEM characterization of the product shows irregular shaped nanocrystals with a polydispersed size distribution. Typical nanocrystal morphology is shown in Figure 4.22a. A lattice fringe resolved image of a ~ 20 nm nanocrystal with the corresponding FFT is shown in Figure 4.22b. The plane spacing is determined to be 3.2 Å which is in agreement with the {220} plane spacing ($Co_9S_{8\{220\}}$ = 3.51 Å). Characterization by XRD showed the dominant phase to be FCC Co_9S_8 with minor peak intensities indexed to FCC Co. The results showed that both precursor solutions produce the same crystal phase

(Co_9S_8) with different morphologies, however nanowire growth was only observed from the solution containing $[Co^{III}Cys_2(H_2O)_2]$.

TGA and differential thermal gravimetric analysis (DTG) characterization of the isolated $[Co^{III}DIP]$ and $[Co^{III}Cys_2(H_2O)_2]$ was performed under inert (N_2) environment at a heating rate of 3 ^oC per minute, the results are shown in Figure 4.23. $[Co^{III}DIP]$ is shown to undergo similar thermal decomposition behavior to $[Co^{III}Cys_2(H_2O)_2]$. The absence of bound water species in $Co^{III}DIP$ is reflected in the mass loss curve by only a subtle change in the temperature region 30 - 200 ^oC which may by attributed to residual water. The ligands remain stable until $\approx$ 279 ^oC before the onset of ligand decomposition. Two distinct thermal events are shown to occur (based on the DTG curve) resulting in a $\approx$ 52% mass loss. This constitutes the major mass loss event during decomposition, following this step gradual mass loss occurs. By contrast $[Co^{III}Cys_2(H_2O)_2]$ shows a single decomposition peak extracted from the DTG curve with a peak rate of mass loss at 260 ^oC (for the examined heating rate).

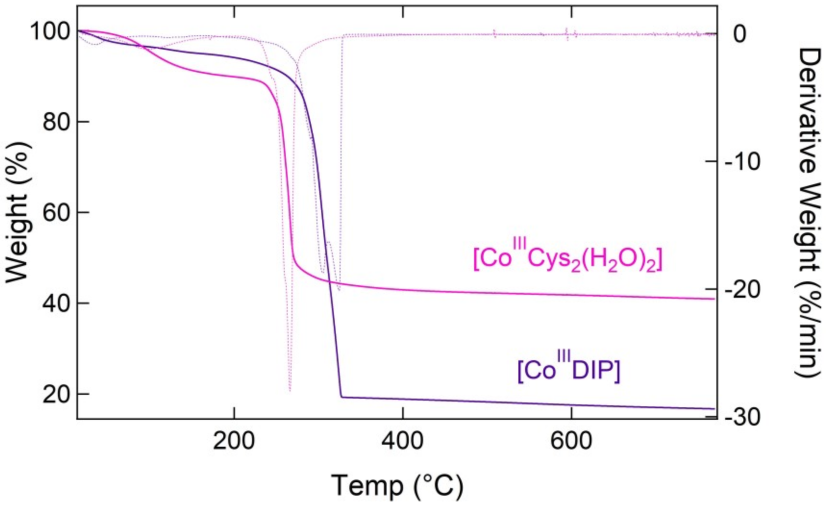

FIGURE 4.23: TGA/DTG curves of $[Co^{III}Cys_2(H_2O)_2]$ and $[Co^{III}DIP]$. The TGA/DTG was measured in a temperature range from 30 to 900 °C in a N_2 atmosphere, the heating rate was 3 °C/min.

Analysis of the volatile decomposition products using gas phase chromatography during thermolysis of cobalt(III) dithiocarbamate provides evidence to the different reaction steps preceding Co_9S_8 nanocrystal formation. TGA-GC-MS was performed on a 1:1 ratio of cobalt(III) dithiocarbamate to cobalt(II) acetate and cobalt(III) bis-cysteinate to cobalt(II) acetate. The thermal decomposition behavior of the different compound mixtures is shown in Figures 4.24 and 4.25.

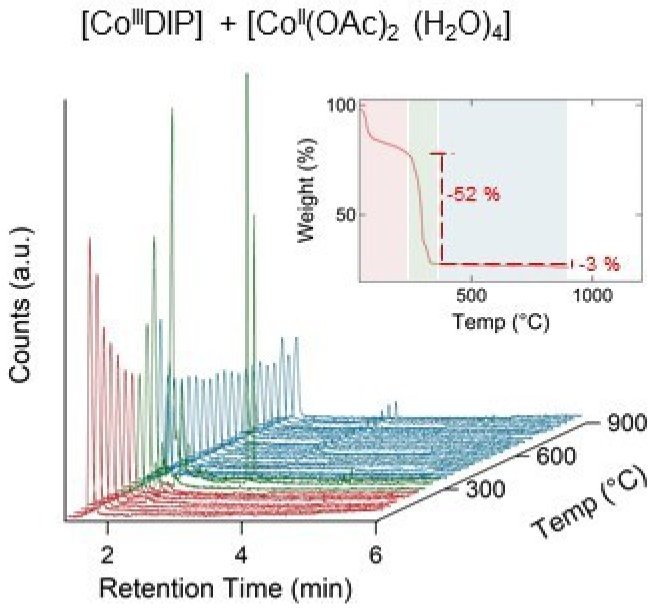

FIGURE 4.24: (Inset) TG analysis of [Co^{III}DIP] + [Co^{II}(OAc)$_2$(H$_2$O)$_4$] precursor compounds. Ion chromatograms sampled every 30 °C of precursor compounds.

Characterization of cobalt(III) dithiocarbamate by TGA-GC-MS is shown in Figure 4.24. Decomposition of the ligand species is first shown to occur at ∼ 279 °C which results in a rapid ∼ 52 % mass loss step. This is highlighted in green in the TG curve (Figure 4.24 inset) as well as the corresponding total ion chromatographs. Following this event steady mass loss of carbon dioxide CO_2, sulfur dioxide (SO_2) and isopropyl isothiocyanate (C_4H_7NS) is observed in the temperature range 300 - 900 °C. Sulfur dioxide and isopropyl isothiocyanate are attributed to ligand decomposition and carbon dioxide the acetate anion. Whilst the generation of SO_2 over the same temperature range is observed in the TGA-GC-MS characterization of the cobalt(III) bis-cysteinate/cobalt(II) acetate precursor compound mixture (Figure 4.25) the presence of C_4H_7NS is not. The results suggest the slow formation of monomer owing to the additional decomposition step which involves the volatilization of isopropyl isothiocyanate.

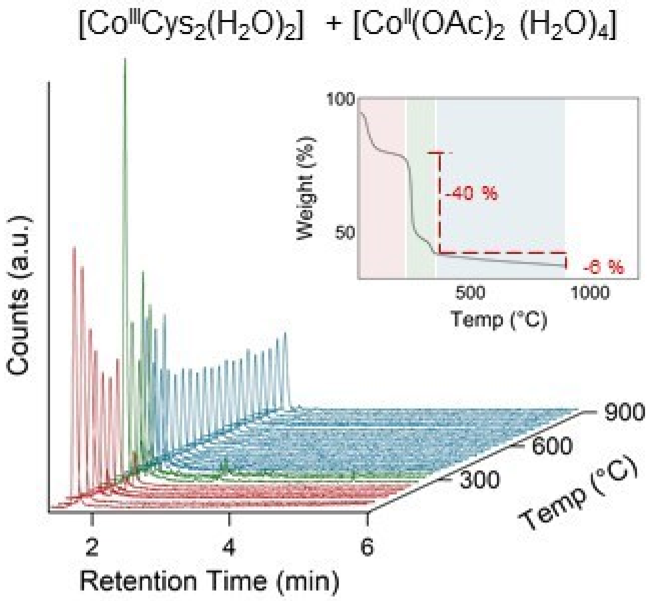

FIGURE 4.25: (Inset) TG analysis of [Co^{III}Cys$_2$(H_2O)$_2$] + [Co^{II}(OAc)$_2$(H_2O)$_4$] precursor compounds. Ion chromatograms sampled every 30°C of precursor compounds.

The extracted ion chromatagraphs for water (m/z = 18), carbon dioxide (m/z = 44), sulfur dioxide (m/z = 64) and isopropyl isothiocyanate (m/z = 101) for both precursor compound mixtures (cobalt(III) dithiocarbamate/cobalt(II) acetate and cobalt(III) bis-cysteinate/cobalt(II) acetate) are shown in Figure 4.26. The extracted ion chromatographs evidence similarities in the thermal properties of the precursors as well as the volatile ligand fragments upon decomposition. The important difference is observed in the extracted ion chromatographs for isopropyl isothiocyanate (Figures 4.26g and h). Volatilization of isopropyl isothiocyanate is shown to produce a peak mass loss at 270 - 300 °C followed by the slow generation up to 900 °C in the [Co^{III}DIP] precursor mixture and is negligible in the [Co^{III}Cys$_2$(H_2O)$_2$] ion chromatograph.

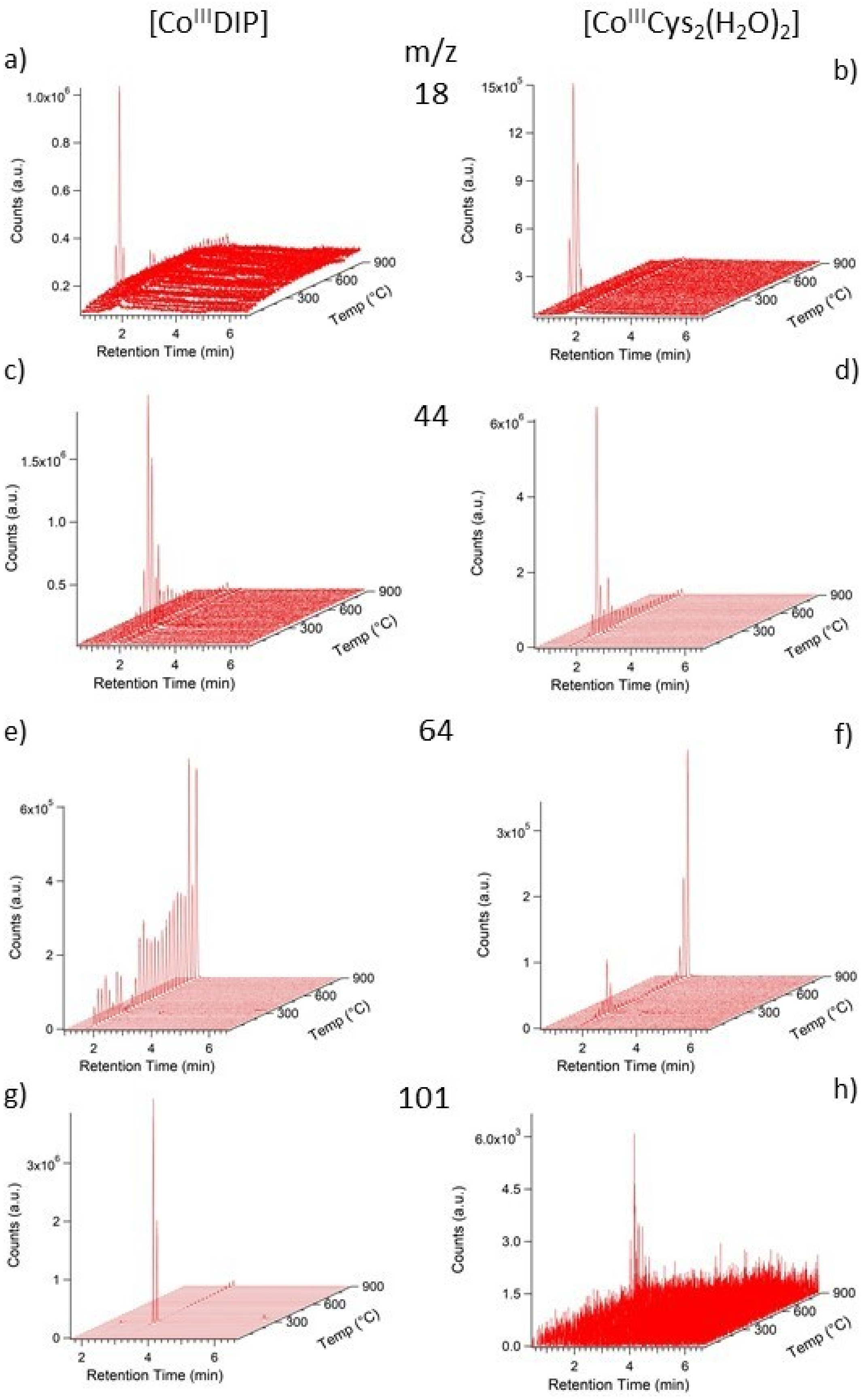

FIGURE 4.26: (Extracted ion chromatographs for $[Co^{III}DIP]/[Co^{II}(OAc)_2(H_2O)_4]$ and $[Co^{III}Cys_2(H_2O)_2]/[Co^{II}(OAc)_2(H_2O)_4]$ for m/z = 18 (a and b), 44 (c and d), 64 (e and f) and 101 (g and h).

4.4 Conclusion

The versatility of cysteine-based precursors is demonstrated in phase-controlled nanowire synthesis by solventless thermolysis. Co_9S_8 and Co nanowires were realized by heat-up synthesis using the precursors cobalt(III) bis-cysteinate and cobalt(II) acetate, the phase was determined by the mole ratio. A similar strategy was successful in the Ni_3S_2/Ni system. Characterization of the nanowire phase, morphology, growth direction and composition is provided showing the nanowires to be high-quality structures with the presence of a capping layer. Understanding of the conversion reactions from precursor to nanowire is elucidated through detailed characterization of the precursors and reaction steps during thermolysis. Real-time characterization using FESEM confirms nanowire growth does in fact occur at the stabilized temperature (and not during cool down) and provides evidence for a base driven mechanism. The results are used to support analysis by TGA-GC-MS of the precursors. Analysis by TGA-GC-MS shows the cysteine ligands are thermally stable to 220 ^{o}C before undergoing decomposition. At temperatures greater than 300 ^{o}C the steady generation of CO_2 and SO_2 are the only volatilized species observed. By comparison with cobalt(III) dithiocarbamate TG reveals similar mass loss behavior however the total ion chromatograms the generation of isopropyl isothiocyanate in the temperature range 350 - 900 ^{o}C. The presence of which is hypothesized to act as a barrier to monomer formation leading to the broad nanocrystal size distribution.

Chapter 5

Role of Functional Groups in Nanocrystal Morphology

5.1 Abstract

In this chapter the role of individual functional groups in nanowire formation is examined based on the precursor cobalt(III) bis-cysteinate. This is achieved by substitution of precursor species and annealing precursor compounds under different environments. The results show that a S and N source are critical to nanowire growth and 1D growth can be achieved using different precursor/reagent combinations that satisfy this requirement. The growth of dense Co_9S_8 nanowires is then realized by high temperature CVD, on arbitrary substrates with no addition of a template or seed. The nanowires are evidenced to be high quality, single-crystal structures with a narrow size distribution.

5.2 Introduction

Using surfactants to modify growth kinetics has shown to be a powerful technique for the synthesis of monodispersed nanocrystals with controllable size and shape.[244] New understanding has lead to the synthesis of monodispersed nanostructures with richer architectures and greater complexity.[268,97] The high affinity for cations has seen the extensive use of sulfur and thiol containing ligands to support finely tuned size distributions and multitudes of shapes in metal and semiconducting nanocrystals.[96,208,49] Stabilization of Au nanocrystals with thiols was first reported by Mulvaney and Giersig in 1993. Soon after, the Brust-Schiffin method was developed which enabled narrow size distributions and control over diameter for the first time.[69,20,21]

Since this work, thiol-based ligands have been used extensively in stabilization of monodispersed nanocrystals of varying sizes and shapes in different material systems including compound semiconductors such as CdE (E = S, Te, Se) and metals including Au, Ag and beyond.[226,178,186,41,190,235] In addition to modifying growth kinetics, termination of semiconductor nanocrystals with thiols has shown to improve luminescence stability.[62]

The complex cobalt(III) bis-cysteinate contains both S and N donors to the cobalt(III) center. Amines are also known capping ligands, however their role appears to be far more complex and perplexing. They have been reported to act as a ligand, shape controlling agent, proton donor, precursor conversion inhibitor and growth activator.[63] Studies have reported conflicting behaviour even within a single crystal system. Amines have been used in the anisotropic growth in Au nanowires and hcp-Co nanodisks, as well as Au and metal-sulfide nanocrystals, InP quantum dots and numerous other material systems.[259,119,169,261,106,148] Few mechanistic studies have been able to isolate their role in nanocrystal synthesis. Studies of note include the synthesis of ultrathin Au nanowires upon reduction of Au^+ following the formation of polymeric strands with alkyl ligands and the use of pulsed field gradient NMR to characterized intermediate species during metal sulfide nanocrystal synthesis.[136,211]

Much of the work on symmetry breaking growth by capping reagents has been centered on co-precipitation techniques. Numerous studies have also highlighted the role of capping ligands in nanowire growth using vapor phase reactants. Direct observation of surface absorbates using operando IR analysis during the VLS growth of Ge nanowires shows hydrogen atoms and methyl groups act to suppress radial growth and eliminate tapering in nanowires.[196] A narrower diameter distribution and elimination of NW tapering was achieved by the introduction of elemental sulfur during the Au catalyzed growth of GaSb nanowires.[257] Cu nanowire growth was demonstrated by CVD of $Cu(etac)[P(OEt)_3]_3$ in the absence of a seed, catalyst or template.[36] Here anisotropic growth is supported by strain in the five-fold twinned crystal habit and the *in situ* generation of phosphite molecules which are known to passivate {100} side planes.[105] Free-standing, high aspect ratio Au nanowire growth supported by the *in situ* generation of capping ligand species has been demonstrated using the precursor $AuN(SiMe_3)_2NHC]$ where NHC = 1,3-diisopropyl-imidazolidin-2-ylidene.[71] Nanowire growth by chemical vapor deposition offers a powerful and scalable approach to substrate independent nanowire synthesis with no template, seed or catalyst.

Insight into the active role of functional groups can be achieved by substitution of starting reagents/precursors. Capping ligands can either be added to the reaction vessel in addition to growth precursor compounds or can be generated *in situ* upon decomposition (single-source precursors). In Chapter 3 it is shown that the thermal decomposition of metal(II/III) bis-cysteinate produces volatile sulfur species at the growth temperature. Whilst sulfur species are known capping ligands, evidence was still lacking for their direct involvement in 1D growth in this study.

In this chapter the role of thiol in the bis-cysteinate precursor and its influence on 1D growth is elucidated. In the first section thermolysis products from starting precursor solutions containing only cobalt(II) acetate, serine/cobalt(II) acetate and cysteine/cobalt(II) acetate (as previously shown) are compared. Cysteine is the only thiol containing amino acid, an important functional group that can undergo oxidation/reduction reactions. This makes it important in biology based on its role in protein structure and in protein-folding.[19] Serine is an amino acid with an identical chemical make-up which only differs in the substitution of an oxygen for the sulfur (Figure 5.1).

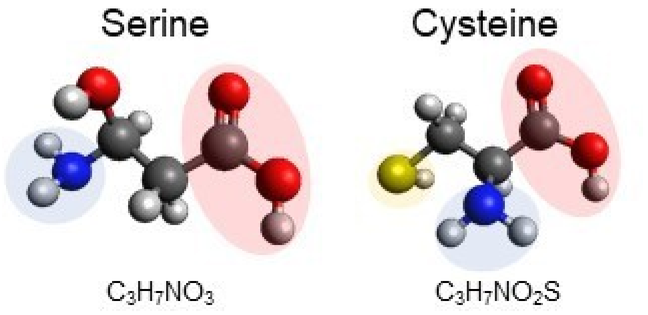

FIGURE 5.1: Schematic illustrating serine and cysteine molecules.

The results show that nanowire growth only occurs from the thiol containing (cysteine) precursor compounds. Nanowire growth can be initiated by annealing the dried serine/cobalt(II) acetate precursor solution in a butanethiol ($CH_3(CH_2)_3SH$) environment. The resulting nanowires show reduced diameter distributions when compared to nanowires synthesized from cysteine under high vacuum annealing. Nanowire growth is not able to be achieved by annealing in an alternative reducing environment (NH_3) suggesting the role of thiol as an essential capping ligand (and not simply a reducing agent). Nanowire growth in the complete absence of an amino acid is demonstrated by a two-step annealing process. The growth procedure involves decomposition of the metal(II) salt in an ammonia environment before annealing in a butanethiol environment. Nanowire growth from cobalt(II) acetate is not observed in the absence of one (or both) of these annealing steps. The results suggest that a N source is also required for 1D growth.

New insight into the fundamental role of functional groups in the biscysteinate complex is achieved. A single-step synthesis technique for the production of Co_9S_8 nanowires by CVD is then reported. The nanowires are evidenced to be high-quality, single crystal structures with a narrow size distribution. Scalable growth can be achieved on arbitrary substrates including Si and carbon cloth for performance testing. The work opens the way for deployment of high-quality Co_9S_8 nanowires into advanced energy storage and conversion applications.

5.3 Experimental

We employ commercially available cobalt(II) acetate tetrahydrate (99.9% Sigma Aldrich), cysteine (≥98.5% Sigma Aldrich), serine (≥99.5% Sigma Aldrich), 1-butanethiol (99% Sigma Aldrich), cobalt tricarbonyl nitrosyl (STREM), and ammonia vapor with no further purification in the following growth experiments. Experimental work performed in this chapter was conducted using 3 different annealing systems. A schematic and discussion of the respective systems can be found in Chapter 3. High vacuum annealing work was performed on the same system used for growth experiments in Chapter 4. Aqueous precursor solutions using the chemical reagents: cobalt(II) acetate, serine and cysteine were prepared in air. In a typical growth procedure, a solution containing the precursor compounds was dropcast and dried onto a clean silicon substrate (with a native oxide layer). After air-drying, the specimen was loaded into the annealing chamber and then evacuated to a base pressure of 2×10^{-7} mbar. After the annealing period the substrate was cooled in high vacuum and removed for characterization.

The two-step annealing process using ammonia and butanethiol vapor was performed on a cold-wall CVD chamber. An aqueous solution of cobalt(II) acetate was dropcast and dried onto a Si substrate. The substrate was loaded into the chamber and both the CVD chamber and gas lines connecting the ammonia and butanethiol supply were pumped to base pressure. Ammonia vapor was introduced at 0.5 sccm, the chamber pressure was stabilized at 0.4 mbar and the substrate was heated to 350 °C. Annealing was performed for 1 hour, a needle valve to throttle the pump was continually adjusted to maintain pressure. The chamber was then evacuated and butanethiol was introduced. The chamber was heated to 600 °C the pressure was stabilized at 0.4 mbar and annealing was performed for 1 hour. The substrate was cooled in a butanethiol environment to room temperature, evacuated, and then vented using N_2 for characterization of the substrate.

The third system used in experimental work discussed in this chapter is a hot-wall CVD chamber. Before each experiment the CVD and gas delivery systems (both the quartz tube and the gas lines leading to the shutoff valve isolating the precursor crucible) were purged with 1000 sccm Ar and the quartz tube was heated to 1000 ^{o}C by the furnace for 30 minutes. After cooling the substrates were loaded into the quartz tube and evacuated to base pressure (2×10^{-2} Torr). Pressure was regulated using manual needle valves to control the precursor flow rate as well as a needle valve to throttle pumping. Gas independent pressure gauges (capacitance manometers) are positioned to measure the pressure of the gas lines going into the furnace and immediately after. This enables the pressure drop across the furnace to be measured. CVD precursors (butanethiol and cobalt tricarbonyl) were loaded into dedicated crucibles under inert (N_2) atmosphere. After loading onto the gas lines the precursors underwent freeze-pump-thaw cycles to remove excess N_2. Both butanethiol and cobalt tricarbonyl have dedicated gas lines that lead into a mixing zone before the furnace. Isolation valves on the lines are used to reduce cross contamination.

5.4 Results and Discussion

5.4.1 Role of Amino Acids: Cysteine versus Serine

To understand the role of functional groups in shaping nanocrystal morphology, thermolysis products from three starting aqueous precursor solutions containing: (1) cobalt(II) acetate ($[[Co^{II}(OAc)_2(H_2O)_4]]$), (2) serine/cobalt(II) acetate ($[C_3H_7NO_3]/[[Co^{II}(OAc)_2(H_2O)_4]]$) and (3) cysteine/cobalt(II) acetate ($[C_3H_7NO_2S]/[[Co^{II}(OAc)_2(H_2O)_4]]$) were compared. The chemical structure of serine is compared to cysteine in the schematic shown in Figure 5.1. The various functional groups are highlighted, the major difference being the hydroxyl group in the serine replaces the thiol group in the cysteine molecule. In each precursor solution the cobalt(II) acetate concentration was 8.0 mM and the amino acid to cobalt(II) acetate mole ratios for the serine (Co^{II}:Ser) and cysteine (Co^{II}:Cys) precursor solutions were 0.8 and 0.9 respectively. Following evaporation of the solvent after dropcasting, substrates were loaded, pumped to high vacuum and annealed at 575 °C for 1 hour. Substrates were then removed for characterization of the thermolysis product.

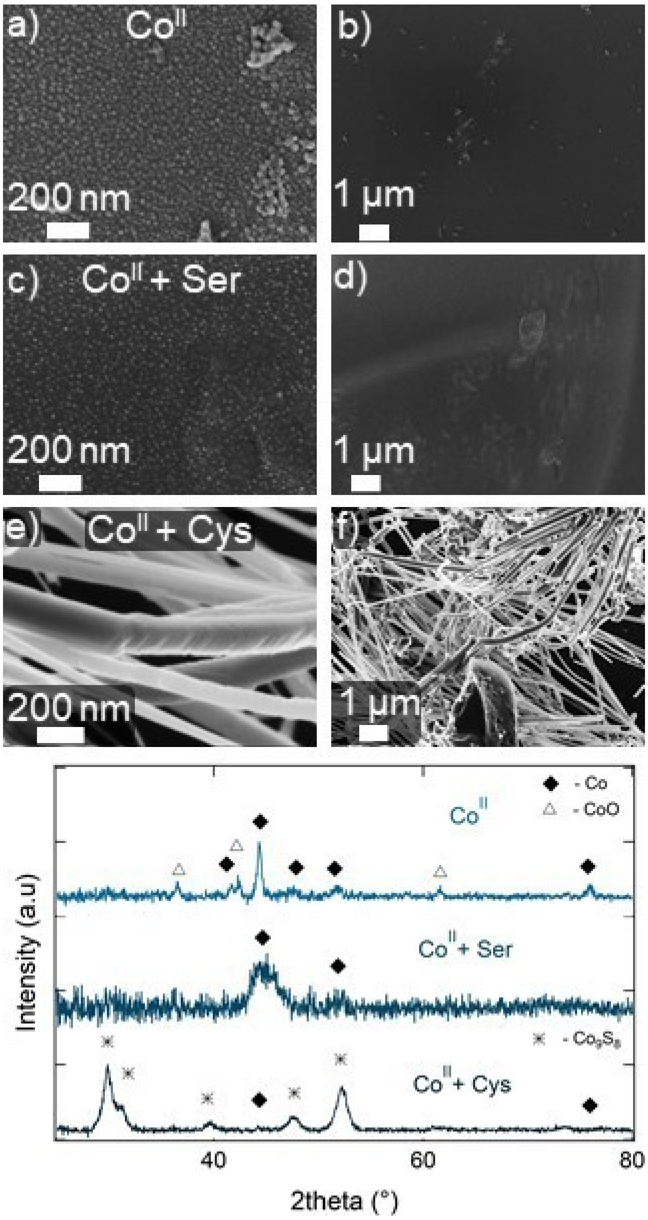

FIGURE 5.2: Thermolysis product of precursor solutions containing cobalt(II) acetate (a and b), cobalt(II) acetate and serine (c and d), and cobalt(II) acetate and cysteine (e and f). g) XRD characterization of each product.

Thermolysis products of the dropcast and dried precursor solutions are shown in Figure 5.2. SEM characterization of the precursor compound cobalt(II) acetate (Co^{II}) showed irregular shaped nanoparticles following thermolysis. XRD characterization of the substrate showed the dominant phase to be FCC Co, with minor peak intensities matching HCP Co and CoO (Figure 5.2g). The mean nanoparticle size was 23 nm. A histogram of the nanoparticle size distribution is shown in Appendix B Figure B.1. Thermolysis of the serine/cobalt(II) acetate (Co^{II} + Ser) precursor solution is shown in Figures 5.2c and d. XRD characterization could not unambiguously identify the phase(s) present and peaks were tentatively assigned to FCC cobalt. Analysis of the nanoparticle size distribution for the serine/cobalt(II) acetate precursor solutions is shown in Appendix B Figure B.1. The mean nanoparticle size was measured to be 16 nm. The Figures 5.2e and f show resulting nanowire growth from a starting cysteine/cobalt(II) acetate precursor solution and XRD characterization (Figure 5.2g) confirms the dominant phase is Co_9S_8. The results shown in Figure 5.2 show the nanocrystal phase and morphology from different starting precursor solutions under identical annealing treatments. The growth of 1D nanowires is only present in the thiol containing cysteine/cobalt acetate precursor solution.

5.4.2 Annealing Precursor Compounds in a Butanethiol Environment

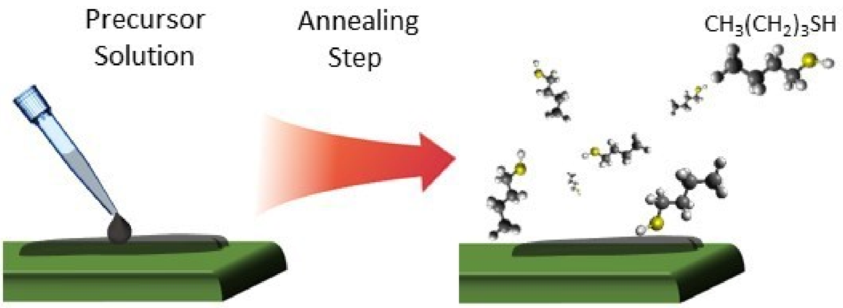

FIGURE 5.3: Schematic illustrate substrate preparation and annealing procedure for precursor solutions in a butanethiol ($CH_3(CH_2)_3SH$) environment.

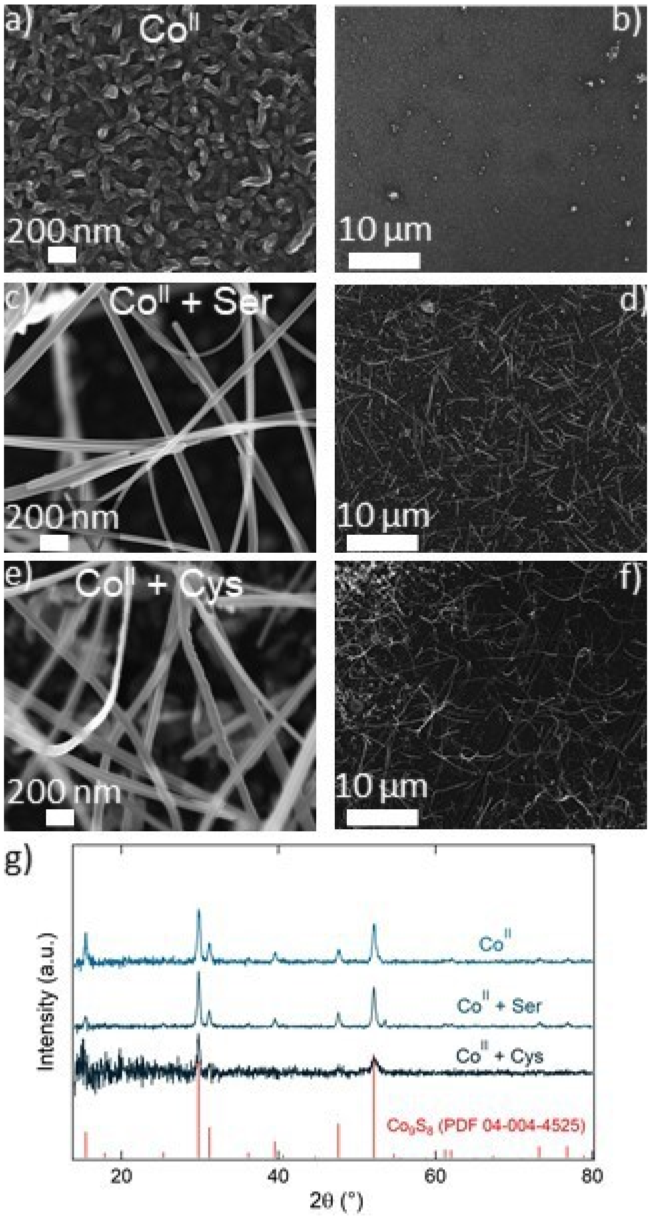

FIGURE 5.4: Thermolysis product of precursor solutions containing cobalt(II) acetate (a and b), cobalt(II) acetate and serine (c and d), and cobalt(II) acetate and cysteine (e and f) annealed in a butanethiol ($SH(CH_2)_2CH_3$) atmosphere. g) XRD diffractogram of each product.

Figure 5.4 shows the result of annealing the same precursor mixtures (following dropcasting and drying) in a butanethiol ($CH_3(CH_2)_3SH$) environment at 1.0 Torr pressure for one hour. The heating rate was 1 - 2 °C/sec. The pressure during heat-up and at the stabilized growth temperature is shown in Appendix B Figure B.2. SEM characterization following the annealing from the starting cobalt(II) acetate solution shows the formation of irregular crystallites (Figures 5.4a and b). XRD characterization confirms that the phase is Co_9S_8. Dense nanowire growth is shown from the starting serine/cobalt(II) acetate (Co^{II} + Ser) and cysteine/cobalt(II) acetate (Co^{II} + Cys) precursor solutions (Figures 5.4c and d, and Figures 5.4e and f respectively). XRD characterization confirms the phase is Co_9S_8 for both. In each experiment the phase was shown to be Co_9S_8 and no other phases were present in the diffractograms.

The nanowire diameter distribution for annealing experiments shown in Figure 5.2e and Figures 5.4c and e is presented in Figure 5.5. The results show that a narrower diameter distribution is achieved by annealing precursor compounds in a butanethiol environment than when compared with high vacuum annealing. The mean nanowire diameter for the cysteine/cobalt (II) acetate and serine/cobalt(II) acetate precursor solutions annealed in a butanethiol environment are 57 nm and 49 nm respectively (compared with 125 nm for the cysteine/cobalt(II) acetate precursor solution annealed in high vacuum). The results also show that 1D growth can be 'turned on' in the precursor solution containing cobalt(II) acetate and serine but not in the precursor solution containing just cobalt acetate. This suggests that the amine group is essential to 1D growth, or that the molecular film formed by the amino acid acts as a template to support 1D growth.

Resulting purification of a Si substrate with dispersed Co_9S_8 nanowires is shown in Figure 5.6. The Co_9S_8 nanowires were grown from a precursor solution containing cobalt(II) acetate and serine. Following dropcasting and drying the precursor residue was annealed in a butanethiol environment as described above. Figures 5.6a and b show SEM characterization of a Si substrate containing high concentrations of nanowires and nanoparticles directly after transfer. Transfer was achieved by gentle rubbing of the growth substrate to clean Si. Purification was achieved by pipetting toluene over the transfer substrate before brief sonication (< 1 sec). Evidence of purification by SEM characterization is shown in Figures 5.6c and d. The red circles indicate the presence of nanoparticles in the high magnification SEM images (Figures 5.6a and c). Following the two-step purification procedure fewer particles were found on the substrate and the remaining particles were much smaller in diameter. It is believed that the high surface area of the nanowires results in stronger van der Waals interaction with the substrate therefore during toluene purging and sonication particles are selectively ejected. The method is suitable for the transfer and purification of nanowires for spatial averaging characterization techniques including vibrating sample magnetometry (VSM) limiting contributions from nanoparticles and other contaminants. The results may also lead to an important means of transferring and purifying metallic

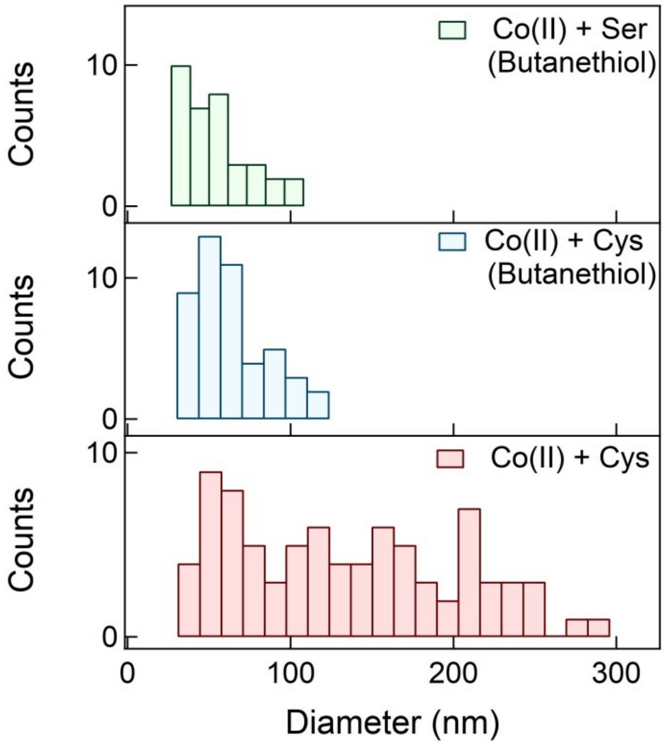

FIGURE 5.5: Histogram comparing nanowire diameter distributions from precursor solutions containing (top) serine/cobalt(II) acetate and (middle) cysteine/cobalt(II) acetate annealed in a butanethiol environment and cysteine/cobalt(II) acetate annealed in high vacuum.

nanowires for applications as transparent conductors.[122]

Whilst the results suggest that a thiol source facilitates 1D growth based on the capping reagent mechanism, 1D growth has also been demonstrated in which molecular films act as templates for nanowire growth.[40] Here the thiol could simply be acting as a reducing agent to supply monomer for growth. To test this theory precursor compounds were annealed in an alternative environment with an efficient reducing agent: ammonia vapor. A precursor solution containing cobalt(II) acetate and serine was dropcast and dried onto a Si substrate and annealed in ammonia vapor (0.4 mbar) for 1 hour at 600 °C. The results are shown in Appendix B Figure B.3, only nanoparticle growth was observed. The annealing experiments presented here are in agreement with the theory that thiol promotes 1D growth and it is not the reduction of cobalt(II) and the precipitation through pores in a molecular template that drives 1D growth.

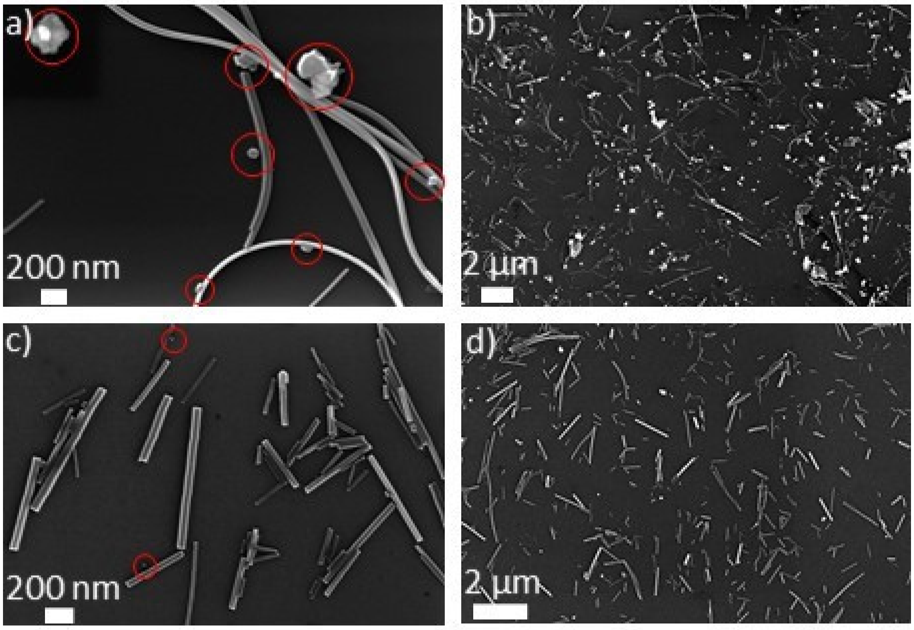

FIGURE 5.6: (a) High magnification and (b) and low magnification SEM images of Co_9S_8 nanowires transferred onto a Si substrate. (c) High and (d) low magnification SEM images of the substrate following purging with toluene and sonication. Red circles in high magnification SEM images indicate the presence of a nanoparticle.

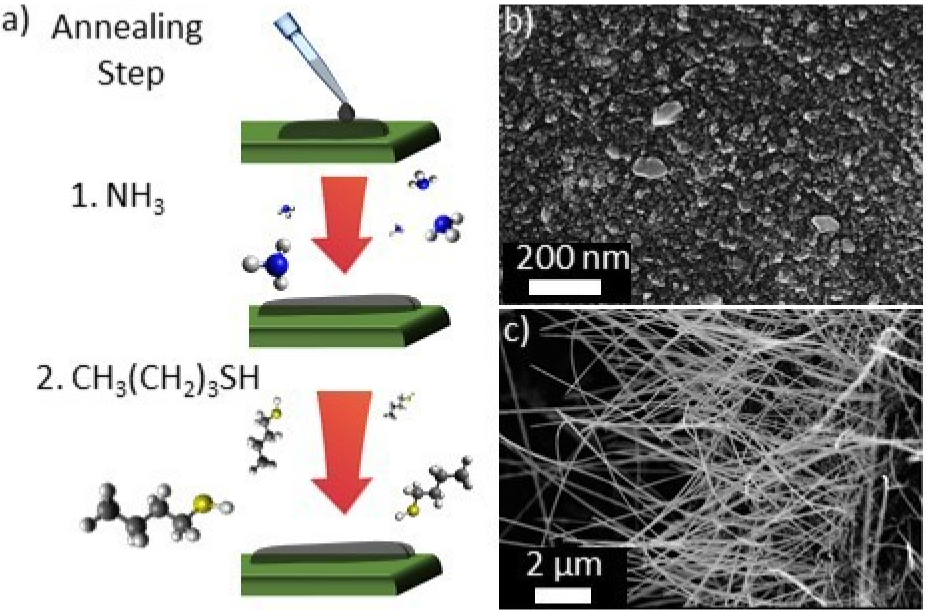

FIGURE 5.7: a) Schematic illustrating 2-step annealing process for nanowire synthesis. b) SEM image of thermolysis product following annealing in an NH_3 environment. c) Thermolysis product following annealing an a butanethiol ($CH_3(CH_2)_3SH$) environment.

Co_9S_8 nanowire growth can be achieved in the absence of an amino acid by a two-step annealing process. The synthesis process involves dropcast and drying of an aqueous cobalt(II) acetate precursor solution onto a clean Si substrate. In the first annealing step, the substrate is heated to 350 °C in an ammonia environment (0.4 mbar) for 1 hour. After which the ammonia vapor was exhausted and butanethiol was introduced. The pressure was increased to (0.4 mbar) and the temperature was increased to 600 °C. The annealing duration was 1 hour. A schematic illustrating the substrate preparation procedure and annealing steps is shown in Figure 5.7a. SEM characterization following annealing in NH_3 is shown in Figure 5.7b and after both annealing steps in Figure 5.7c. The results show nanowire growth can be achieved using readily available and easy-to-handle metal acetate salt as a starting reagent and nanowire growth requires the presence of a N source (ammonia) and thiol source.

5.4.3 Co_9S_8 Nanowire Growth Using Vapor Phase Surfactants

The growth of free-standing Co_9S_8 nanowires is achieved by high temperature CVD using the precursors cobalt tricarbonyl nitrosyl ($Co(CO)_3NO$) and butanethiol ($CH_3(CH_2)_3SH$). Nanowire growth is demonstrated on arbitrary substrates, with no hard-template, binder, or additional seed particles. Research into binder-free assembly is motivated by fewer processing steps, reduced weight, uncertainty of the carrier diffusion path and inhomogeneities in the active material/binder blend as well as limitations associated with binders under different chemical environments.[76] Initial work was performed on the cold-wall CVD system. Optimization of nanowire growth conditions involved testing different precursor partial pressures and temperatures. Pressure and temperature parameters were optimized for carbon paper to directly enable performance testing. In a typical growth procedure a clean substrate was loaded into the system and both the chamber and the gas delivery lines required for growth were pumped to high vacuum. The substrate was heated to growth temperature (under high vacuum), once temperature was stabilized the TMP was isolated and spun down. Butanethiol was introduced and the chamber was stabilized at the desired pressure, after which cobalt tricarbonyl was introduced.

Figure 5.8 shows Co_9S_8 nanowire growth resulting from high temperature CVD using the precursors cobalt tricarbonyl nitrosyl and butanethiol. SEM images show straight, high aspect ratio nanowires with smooth surfaces, characteristic of single-crystal structures and dense coverage over a

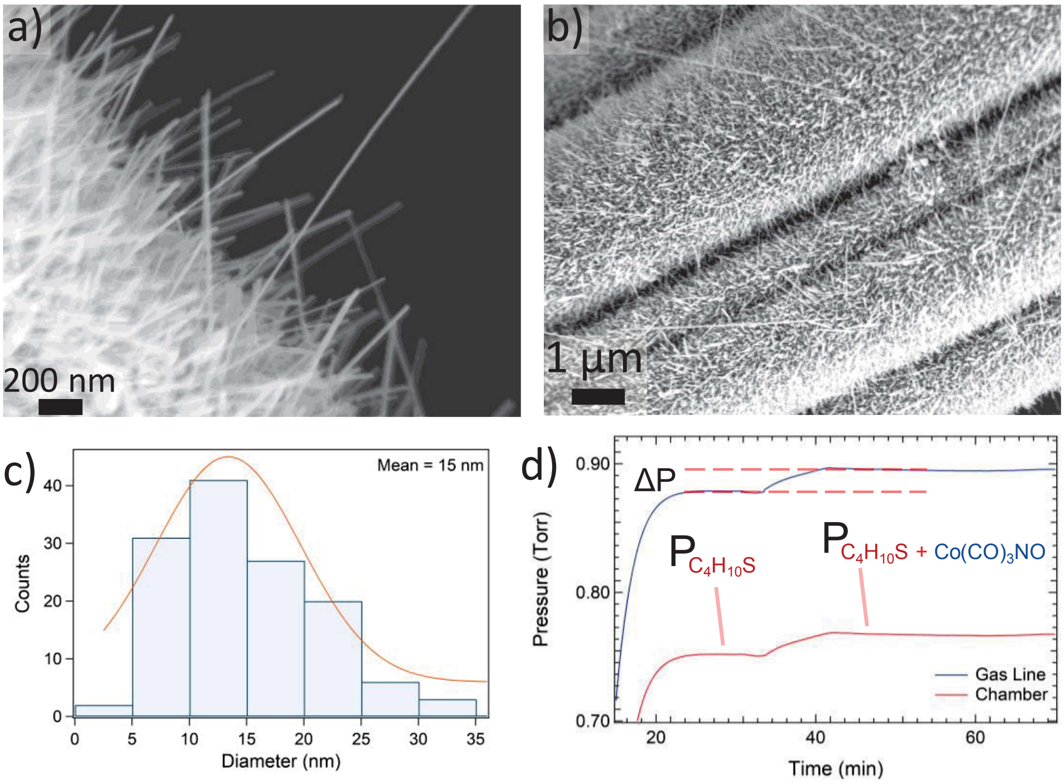

FIGURE 5.8: a) High magnification and b) low magnification SEM image of Co_9S_8 nanowire growth on carbon paper by high temperature CVD. c) Histogram showing nanowire diameter distribution. d) Plot showing pressure recorded using capacitance manometers during growth.

carbon fiber substrate. The average diameter was measured to be 15 nm based on the analysis of 132 nanowires with a narrow diameter distribution (Figure 5.8c). Pressure was measured using two capacitance manometers; the first measuring pressure in the gas lines in the 'mixing region' before entering the chamber and the other in the chamber. The recorded pressure clearly shows changes upon introduction of both precursor species (Figure 5.8d). After heating to 650 °C butanethiol is introduced and the chamber pressure is stabilized at ~0.752 Torr. The total pressure increase associated with the introduction of $Co(CO)_3NO$ is ~0.767 Torr shown at ~30 minutes. Based on the change in pressure, the $Co(CO)_3NO$ partial pressure is calculated to be ~0.015 Torr, the precursor ratio ($CH_3(CH_2)_3SH$:$Co(CO)_3NO$) is thus determined to be ~50. SEM characterization of the substrate showed nanowire coverage varied, the edges showed most dense nanowire growth whilst the center regions showed sparse coverage of nanowires and the dominant morphology was irregular, asymmetric nanocrystals (Appendix B Figure B.4).

A precursor delivery and exhaust system was built and attached onto a standard tube furnace for the purpose of nanowire growth in a hot wall system. CVD work in a quartz tube with the heating element on the outside offered numerous benefits. For nanowire growth studies, this enabled examination of a wider parameter space, as the deposition of metal in the chamber demonstrated the potential to short-out the resistance heating element and sulfur related corrosion was significant at elevated temperatures. Using a tube furnace experimental work could be conducted at higher temperatures for longer durations with greater thiol and Co precursor pressures. A schematic of the furnace and gas delivery system is shown in Chapter 3 Figure 3.19.

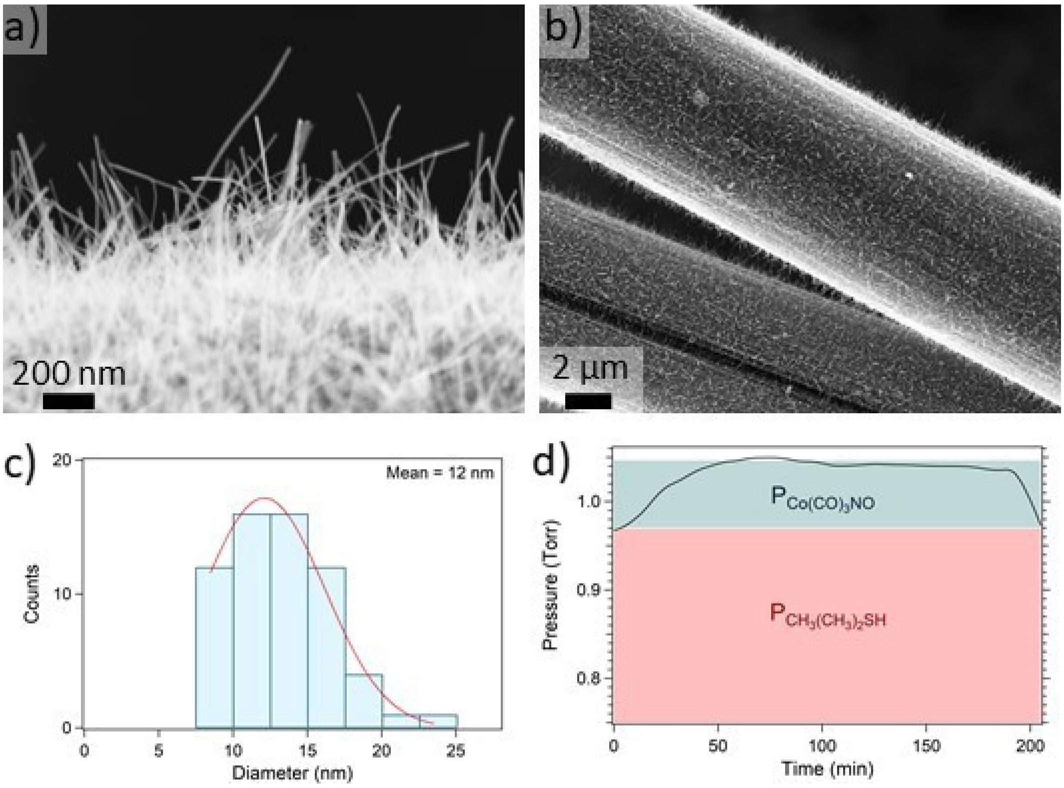

FIGURE 5.9: a) High magnification and b) low magnification SEM image of Co$_9$S$_8$ nanowire growth on carbon paper by high temperature CVD. c) Histogram showing nanowire diameter distribution. d) Plot showing pressure recorded during growth. The partial pressures of the precursor species (CH$_3$(CH$_2$)$_3$SH and Co(CO)$_3$NO) are denoted by the red and blue shaded regions (respectively).

Figure 5.9 shows nanowire growth following annealing in a mixed butanethiol and cobalt tricarbonyl nitrosyl environment at 700 °C. The system was heated to growth temperature in a CH$_3$(CH$_2$)$_3$SH environment. The pressure was stabilized at $\sim$0.97 Torr CH$_3$(CH$_2$)$_3$SH, before the introduction of $Co(CO)_3NO$. The change in the total pressure of the system can be attributed to the $Co(CO)_3NO$ partial pressure (~0.0445 Torr) the precursor ratio ($CH_3(CH_2)_3SH$:$Co(CO)_3NO$) is thus determined to be ~22. The growth time was measured from when the chamber pressure was approximately stable after the introduction of $Co(CO)_3NO$ and was approximately 2 hours. High magnification and low magnification SEM images (Figure 5.9a and b) show dense nanowire growth over the carbon paper substrate. The nanowires have a narrow size distribution. Based on the analysis of 62 nanowires the mean diameter was 12 nm (Figure 5.9c). The pressure change upon introduction of $Co(CO)_3NO$ measured by the capacitance manometer on the gas lines and is shown in Figure 5.9d. The precursor partial pressure is denoted by the red and blue colored regions for $CH_3(CH_2)_3SH$ and $Co(CO)_3NO$ respectively.

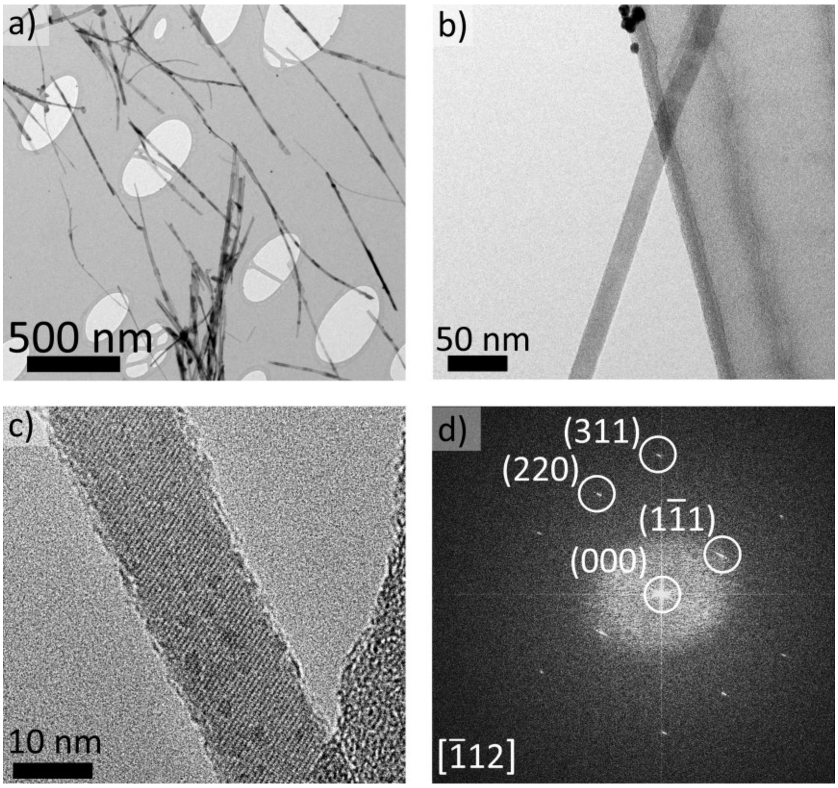

FIGURE 5.10: a) Low magnification TEM image of Co_9S_8 nanowires dispersed on a holy carbon TEM grid. b) TEM image of an isolated Co_9S_8 nanowire. c) HRTEM image of a Co_9S_8 nanowire. d) FFT of nanowire in c.

A TEM image of Co_9S_8 nanowires transfered onto a holy carbon TEM grid is shown in Figure 5.10a. The nanowires were transfered by gently touching the TEM grid to the growth shown in Figure 5.9. TEM characterization revealed the growth of both nanowires and nanobelts (Appendix B Figure B.5). In a similar study the formation of Au nanobelts with $< 110 >$ growth direction has been reported using co-surfactant mixtures.[268] The TEM image in Figure 5.10b shows a high-aspect ratio nanowire (diameter = 19 nm) with smooth and well defined surfaces and no evidence of tapering. HRTEM characterization of an isolated 14 nm nanowire and the corresponding FFT is shown in Figures 5.10c and d, respectively. The nanowire is single-crystal and the zone axis was indexed to the $[\bar{1}12]$ plane of the FCC cubic crystal structure. The nanowire growth direction could be directly identified and was determined to be along the $< 110 >$ direction. The $\{111\}$ plane spacing was measured to be 6.15 Å in good agreement with the sulfide phase Co_9S_8 (5.907 Å). Artifacts in the lattice spacing measurements can be caused by numerous factors including tilt and defocus as well as strain and chemical or structural changes due to beam irradiation.[14]

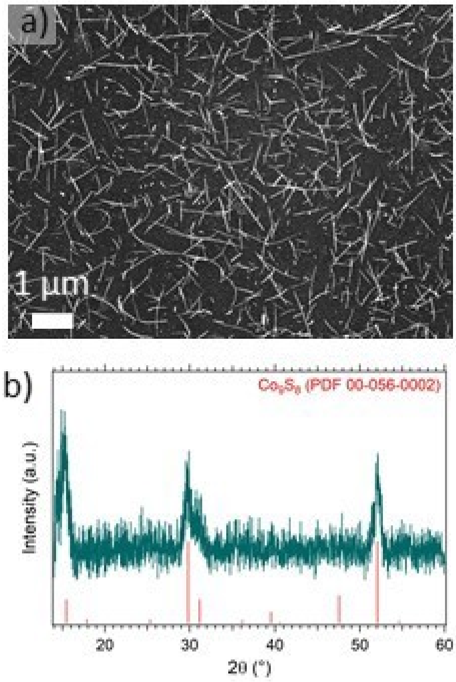

FIGURE 5.11: a) SEM image of Co_9S_8 nanowire growth on a Si substrate. b) XRD characterization of the substrate shown in a.

Figure 5.11 shows Co_9S_8 nanowire growth on a Si substrate and X-ray diffraction characterization of the substrate. The diffractogram (Figure 5.11b) was a good fit for FCC Co_9S_8. Both HRTEM and XRD characterization of the as-grown nanowires are in agreement and support the nanowire phase assignment of FCC Co_9S_8. These results support the claim that nanowire growth can be achieved on arbitrary substrates by high temperature CVD using the precursors butanethiol and cobalt tricarbonyl nitrosyl.

5.5 Conclusion

In this chapter I provide a detailed experimental investigation into the role of functional groups in shaping nanocrystal morphology based on nanowire growth from the precursor cobalt(III) bis-cysteinate. This is achieved by the substitution of chemical reagents or precursors in annealing experiments. The results show that (1) anisotropic growth requires both the presence of a N and thiol source, (2) 1D growth is supported by the capping reagent mechanism in which the anion SH^- is the likely ligand (3) the role of N is critical to achieving 1D growth however its exact function is unknown. Further, it can be concluded that 1D growth is not driven by the precipitation of crystalline Co_9S_8 from pores in a molecular film and that annealing in environments containing alternative reducing agents (i.e. NH_3) does not elicit nanowire growth. A recipe to achieve high yield Co_9S_8 nanowire growth with a narrow diameter distribution is demonstrated as well as a method for nanowire transfer and purification. A precursor system and reaction conditions are presented for growth of free-standing Co_9S_8 nanowires by high-temperature CVD. The nanowires are high-quality, single-crystal structures with smooth surfaces and can be grown on arbitrary substrates in the absence of a seed or template. In summary, Co_9S_8 nanowire growth is initiated with different starting reagents and precursors. Through elimination, essential functional groups are identified and different reaction schemes are demonstrated. New understanding of the chemistry involved in nanowire synthesis is achieved and a high-yield, synthesis method is demonstrated.

Chapter 6

Conclusions and Outlook

Here, I provide a summary of my results, and discuss the broader significance of this work. Finally, I will provide an outline of the future directions of this project.

In this work, a novel precursor system is reported for the controlled growth of metal (Co and Ni) and metal sulfide (Co_9S_8 and Ni_3S_2) nanowires, and the precursor conversion reactions are studied. The nanowire phase is modulated by tuning the relative concentration of metal(II/III) bis-cysteinate to metal(II) acetate. A detailed study of the precursors, the reaction pathways and the role of function groups in synthesis is then presented. Nanowire growth is demonstrated by solventless thermolysis (a subset of coprecipitation synthesis methods) which enables unique insight into the precursor conversion chemistry in symmetry breaking nanocrystal growth. *In situ* characterization during precursor thermolysis is performed using thermogravimetric analysis with gas chromatography-mass spectrometry (TGA-GC-MS) and field-emission scanning electron microscopy (FESEM). Time-dependent FESEM characterization unambiguously confirms the nanowire growth temperature and suggests that growth occurs by a base-driven mechanism. Dynamic characterization of the morphological changes are then correlated with chemical analysis techniques to provide further insight into the precursor conversion chemistry. Studying the reaction steps using TGA-GC-MS enables highly sensitive characterization of precursor decomposition during thermolysis. Here, intermediate states preceding nanocrystal nucleation, as well as decomposition behavior at the nanowire growth temperature can be probed. The results show that the cysteine ligands are thermally stable to 180 °C, before a major mass loss event which produces unknown Co_xS_y species. Following this, the slow generation of CO_2 and SO_2 is observed in the temperature range 300 - 900 °C, encompassing the nanowire growth temperature. Importantly, the slow generation of S species is shown to promote 1D growth and substituting the acetate anion (in the metal salt) for Cl^- inhibits nanowire growth. This proves that both S and acetate species play a role in 1D growth.

In Chapter 5, the active functional groups in the cobalt(III) bis-cysteinate precursor were identified, and their role in shaping nanocrystal composition, morphology and concentration was studied. This was achieved by substituting chemical reagents or precursors. The results show that a thiol and N source are essential to 1D growth, that growth can be achieved using different combinations of precursors and/or chemical reagents, and that annealing in a butanethiol environment produces nanowires with a narrower diameter distribution. Further, the growth of dense single-crystal Co_9S_8 nanowires is demonstrated by high temperature CVD using vapor-phase precursors on arbitrary substrates in the absence of a seed or template.

Understanding of precursor conversion chemistry in nanocrystal synthesis is an active area of research. Currently, conflicting results exist and general theory is still lacking. Even greater complexity exists in symmetry breaking growth of nanocrystals. Mechanistic studies that utilize *in situ* characterization during nanocrystal synthesis have proven invaluable to furthering understanding. However these studies remain extremely challenging owing to the speed of reactions, the reaction environment, high temperatures required for growth, and limitations of characterization techniques. In particular dynamic characterization studies under 'wet' environments are hindered by a lack of sensitivity, the presence of optically invisible species and can neglect the role the solvent plays in synthesis. By utilizing precursors that demonstrate nanowire synthesis in the absence of a solvent, the reaction steps that precede crystal nucleation and 1D growth can be studied using non-traditional, highly-sensitive techniques. TGA-GC-MS enables insight into intermediate species formed during synthesis and the chemical pathway from precursor to nanowire.

Dynamic characterization during precursor thermolysis is shown to be an important tool in understanding precursor to nanocrystal conversion, in particular how the *in situ* generation of capping ligands alters crystal growth kinetics. Numerous studies exist on solventless thermolysis of nanocrystals with different morphologies, including the synthesis of monodispersed 1D materials.[194,115,66,193] Common behavior in the reaction steps and generation rates of volatilized ligand fragments by TGA-GC-MS and FESEM would provide important information on how precursor chemistry leads to anisotropic crystal growth.

Transition metal sulfides in particular Co_9S_8 and Ni_3S_2 hold high potential in applications including catalysis, batteries and dye-sensitized solar cells.

The significance of oxygen evolution reaction as well as the theoretical performance of nanostructured Co_9S_8 strongly support performance testing for this reaction. By demonstrating growth of Co_9S_8 nanowires on carbon fibre paper, the performance can be directly tested with no binder required.

General agreement is held on the intimate relationship between the precursor reactivity and the resulting nanocrystal morphology; understanding the exact nature of this relationship requires more rigorous *in situ* characterization studies which target intermediate chemical species, reaction byproducts and rates of decomposition. The result will enable precursors-by-design for nanocrystals with tailored shapes and compositions. Here, we are able to show the decomposition behavior of simple-molecular precursors that support symmetry breaking growth in a number of material systems. Moreover, my findings provide new insights into the precursor conversion rates and reaction byproducts that support symmetry breaking growth in nanocrystals. This has been demonstrated in high symmetry FCC crystals which do not intrinsically favor anisotropic growth. In addition, 1D growth is not supported by the presence of a twin-defect in the nucleated crystal habit, and therefore suggest anisotropic growth is supported by direct interaction of chemical species with the growth interface and sidewalls. Beyond mechanistic studies, performance testing of Co_9S_8 nanowires is enabled by demonstrating a simple, single-step annealing technique for the growth of dense, free-standing nanowires on arbitrary substrates. The nanowires are shown to be high-quality single-crystal structures with smooth surfaces.

Appendix A

Appendix A

A.0.1 Experimental

Precursor solutions for the growth of Co_9S_8 and Co nanowires: Solutions suitable for thermolysis were prepared by dissolving a mixture of cobalt(II) acetate tetrahydrate and L-cysteine in millipore water (18.4 MΩ cm^{-1}). The cysteine mass was kept standard to achieve 9.0 ± 0.5 mM solutions whilst appropriate amounts of cobalt(II) acetate were added to obtain solutions with Co^{II}:Cys mole ratios ranging from 0.5 to 9.7.

Precursor solutions for the growth of Ni_3S_2 and Ni nanowires: Solutions suitable for thermolysis were prepared by dissolving a mixture of nickel(II) tetrahydrate and L-cysteine in millipore water (18.4 MΩ cm^{-1}). The cysteine mass was kept standard to achieve 9.0 ± 0.5 mM solutions whilst appropriate amounts of nickel(II) acetate were added to obtain solutions with Ni^{II}:Cys mole ratios ranging from 1.0 to 4.9. To achieve Ni_3S_2 nanowire growth a 5 mL aliquot was taken from the 1.0 Ni^{II}:Cys mole ratio solution. To this approximately 3 mL of hydrogen peroxide solution (30 % w/w in water) was added. The solution appeared to turn clear.

Cobalt(III) bis-cysteinate characterization: UV-visible (UV-vis) absorbance characterization of the cobalt(III) bis-cysteinate complex was done on both stock solutions prepared by mixing the reagents as described above and also by isolating the cobalt(III) bis-cysteinate complex through filtration of the crude reaction mixture. The crude reaction mixture was clarified by filtration through a 0.45 m syringe filter, and the resultant filtrate was collected. Purification of the crude filtrate was achieved by addition of chloroform, followed by a sufficient volume of methanol to achieve a uniform solution. Upon cooling, a dark green material was precipitated and collected by vacuum filtration, resulting in a pale pink filtrate and an oily green-brown filter cake. The latter was repeatedly triturated using cold methanol and then dried in vacuum. A similar process was performed for the isolation of the nickel(II) biscysteinate precursor.

Degassed aqueous solutions of cobalt acetate (40 mM) and cysteine (8.6 mM) were prepared by dissolving into separate already degassed (0.1% acetic acid v/v) aqueous solutions. Degassing was done by purging N_2 through each solution for 30 minutes before adding cysteine and cobalt(II) acetate to the respective solutions. Degassing was continued for a further 10 minutes before the cobalt(II) acetate solution was mixed into the cysteine solution whilst stirring. Upon air exposure, the resulting orange solutions gradually changed to a dark brown colour.

Nanowire growth: 30 μL of the precursor solution was dropcast onto clean Si substrates (with a thermal oxide) held at 100°C. Following solvent evaporation, the substrate was loaded into the vacuum chamber, pumped to high vacuum (1 x 10^{-7} mbar) and heated to the desired growth temperature. The temperature was measured using a single thermocouple placed directly onto a mock Si substrate located adjacent to the growth substrate (on the heater). The heating rate was 2 - 3 °C / sec. Annealing temperature for Co_9S_8/Co nanowire growth was 470 - 590 ± 20 °C, the total time at this temperature was 1 hour. For Ni_3S_2 nanowire growth the annealing conditions were 415 ± 10°C for 5 hours. The substrates were cooled under high vacuum before removal for characterization.

Mass spectrometry, UV-Vis and FTIR spectroscopy: High resolution mass spectrometry (HRMS) was performed using an Agilent 6510 Q-TOF with a mobile phase of 70% acetonitrile, 30% water and a flow rate of 0.5 mL/minute. FTIR spectra were acquired using a Nicolet 6700 FTIR spectrometer fitted with a diamond smart iTX ATR accessory. Each spectrum was collected using 64 scans, with a resolution of 2 cm^{-1} over the range of 5000 - 600 cm^{-1}. UV-Vis spectra of aqueous solutions were acquired using a Cary 60 spectrometer from 190 to 800 nm at 0.5 nm resolution. HRMS (M^+) for $[CoC_6H_{12}N_2O_4S_2]^+$ Calculated: 298.9565; Observed: 298.9580.

Thermogravimetric analysis and gas chromatography (TGA-GC-MS) were performed using a Netzsch STA 449 F5 Jupiter thermal analyser coupled with a heated transfer line to an Agilent 7890/5977 GC/MS. Samples were placed in a 90 μL alumina crucible, and experiments were conducted using an atmosphere of helium (100 mL min^{-1}) and a heating rate of 3 °C min^{-1} from 30 to 900 °C. A 150 μL aliquot of furnace gas was subjected to a 1:5 dilution with helium, and a small quantity injected every 8 minutes through an Agilent

HP-5MS column, with separation achieved using a temperature ramp from 50 to 200 °C with a heating rate of 2 °C / min.

SEM, EDS, XRD, HRTEM and SAED characterization: The growth products were imaged using a Zeiss Supra 55VP scanning electron microscope (SEM), using an Oxford Instruments INCA X-Sight 7558 for energy dispersive X-ray spectroscopy (EDS) microanalysis. Transmission electron microscope (TEM), high resolution TEM (HRTEM) imaging and selected area electron diffraction were performed on a FEI Tecnai T20 TWIN microscope (LaB_6) operating under an accelerating voltage of 200 kV. Selected area electron diffraction (SAED) characterization of a gold standard was used for calibration of plane spacing measurements. A Bruker Discover D8 Powder X-ray diffractometer with Cu Kα (λ = 1.54060) was used to acquire diffractograms. Nanowire growth substrates were characterized using grazing-angle incidence X-ray diffraction, the scanning range (2θ) was 20 - 80^o with a step size of 0.02^o. The TGA-GC-MS powder residue X-ray diffraction data was acquired using a coupled scan. For the cobalt(III) bis-cysteinate residue the scan range was 14 - 70^o and nickel(II) bis-cysteinate 20 - 60, step sizes were 0.02^o for both. Characterization of nanowires during growth was performed using a Nova nanoSEM Sirion column. A homemade heating stage was used to heat the sample to growth temperature (540 ^{o}C) under high vacuum (9 x 10^{-6} mbar). Temperature was measured by a thermocouple on a replica Si substrate clipped to the heating stage.

A.0.2 Heating Rate

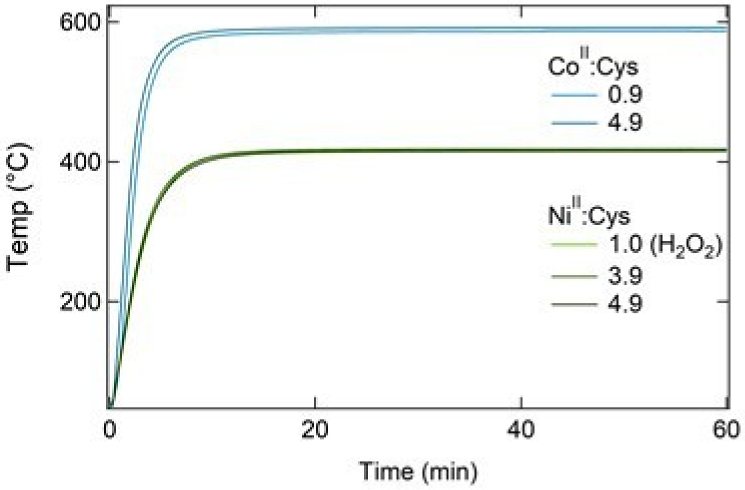

FIGURE A.1: The heating rate and annealing profile for nanowire growths.

The recorded heating rate and annealing temperature profiles for Co_9S_8, Co, Ni_3S_2 and Ni nanowire growths resulting from the starting 0.9 and 4.9 Co^{II}:Cys and 1.0, 3.9 and 4.9 Ni^{II}:Cys mole ratio solutions is shown in Figure A.1.

A.0.3 Diameter and Length Characterization

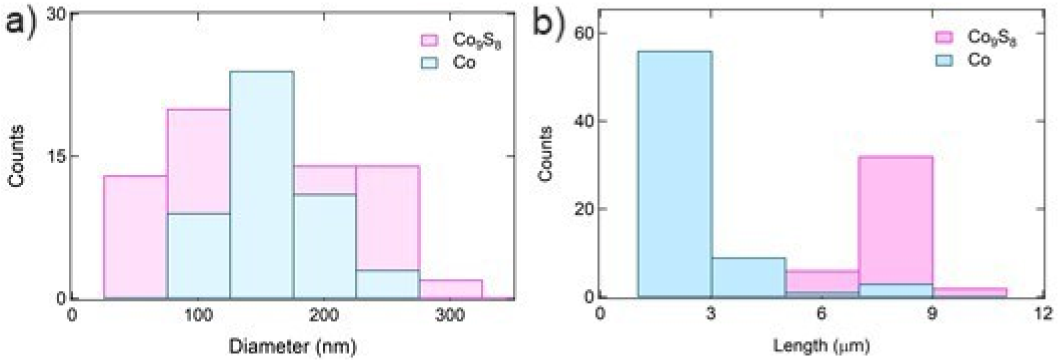

FIGURE A.2: Histograms showing Co_9S_8 and Co nanowire a) diameter distribution and b) length distribution from a starting 0.9 and 4.9 (Co^{II}:Cys) mole ratio solution, respectively.

The diameter and length distributions for Co_9S_8 and Co nanowires from the 0.9 and 4.9 (Co^{II}:Cys) precursor solutions are shown in Figures A.2a and b (respectively).

A.0.4 Thermolysis Product of Cobalt(III) Bis-Cysteinate and Cobalt(II) Chloride.

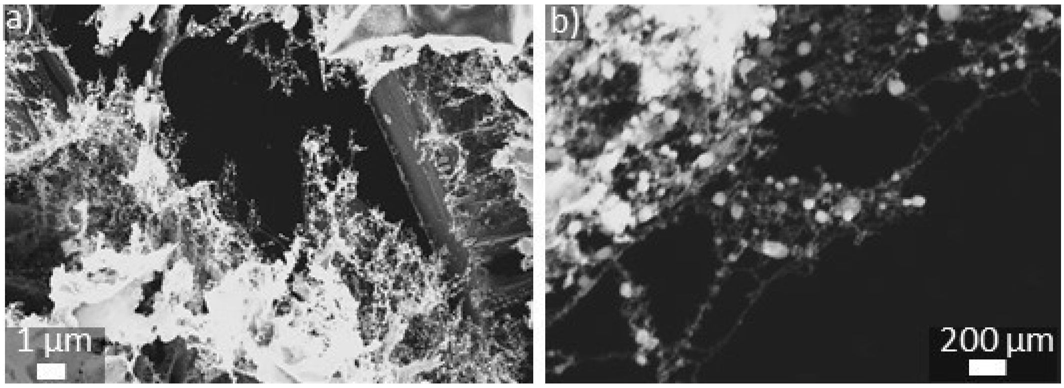

FIGURE A.3: a) SEM image of thermolysis product from a 4.9 (Co^{II}:Cys) mole ratio solution annealed at 490 ^{o}C using the cobalt(II) salt [$Co^{II}Cl_2(H_2O)_6$]

To examine the role of the acetate counter anion in nanowire formation a precursor solution was prepared by mixing cobalt(II) chloride ($[Co^{II}Cl_2(H_2O)_6]$) with cobalt(III) bis-cysteinate. The mole ratio of the cobalt(III) complex to cobalt salt was equivalent to that of a 4.9 (Co^{II}:Cys) mole ratio solution. Substrate preparation follows the same procedure outlined and annealing conditions were 575 °C in high vacuum for 1 hour. Analysis of the thermolysis product by SEM suggests the formation of nanocrystals (Figure A.3). No nanowires were present and no further characterization was performed.

A.0.5 Co_9S_8 and Co Nanowire Characterization at Upper and Lower Temperature Thresholds

Characterization of the thermolysis product of a 0.5 (Co^{II}:Cys) mole ratio solution annealed at 490 °C and 590 °C is shown in Figure A.4. At the lowest examined temperature (470 °C) the nanowire concentration was too low to successfully transfer onto a TEM grid, therefore characterization was performed on the thermolysis product following annealing at 490 °C. TEM and SAED characterization of a transferred nanowire is shown in Figures A.4b and c (respectively). SAED pattern of the nanowire in Figure A.4b was resolved along the [011] zone axis. The {111} plane spacing ($d_{\{111\}}$ = 5.51 Å) was in agreement with FCC Co_9S_8 ($d_{\{111\}}$ = 5.729 Å).

SEM characterization of the thermolysis product following annealing at 590 °C is shown in Figure A.4d. TEM characterization of an isolated nanowire with the corresponding SAED is shown in Figures A.4e and f. The zone axis was determined to be [001] with the measured plane spacing ($d_{\{200\}}$ = 4.83 Å) in agreement with FCC Co_9S_8 ($d_{\{200\}}$ = 4.962 Å). The nanowire is evidenced to be single-crystal, cubic structures with lattice calculations consistent with Co_9S_8 for the examined annealing temperature window.

Composition and phase analysis by SEM, TEM and SAED of the 1-dimensional materials grown at the upper and lower annealing temperatures was done for the 9.0 (Co^{II}:Cys) solution in which Co_9S_8 nanowire growth was completely absent or negligible for all annealing temperatures. Characterization of the thermolysis product of a 9.0 (Co^{II}:Cys) mole ratio solution annealed at 470 °C and 590 °C is shown in Figure A.5. TEM and SAED characterization of a transferred nanorod is shown in Figures A.5b and c (respectively). SAED pattern of the nanorod in Figure A.5b was resolved along the [001] zone axis. The {200} plane spacing ($d_{\{200\}}$ = 1.74 Å) was in agreement with FCC Co ($d_{\{200\}}$ = 1.78 Å).

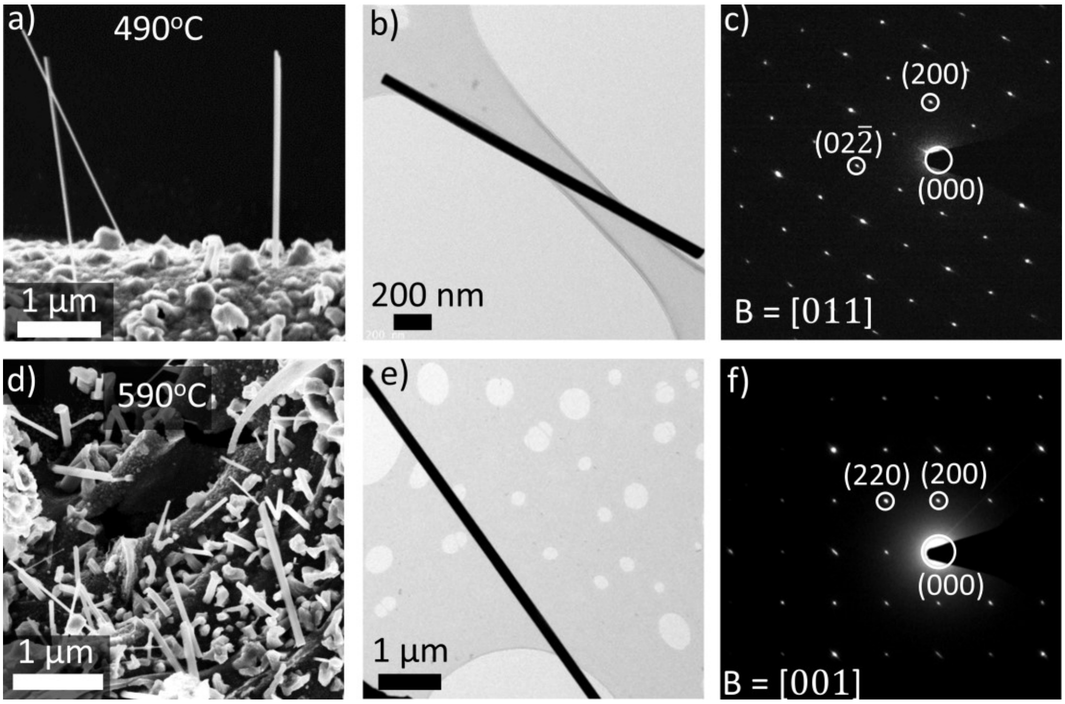

FIGURE A.4: a) Low magnification SEM image of Co_9S_8 nanowire grown at 490°C. b) TEM image of isolated Co_9S_8 nanowiretransferred from a). c) SAED pattern of Co_9S_8 nanowire in b). d) SEM image of growth on substrate annealed at 590°C. e) TEM image of isolated nanowire from the substrate shown in d). f) SAED pattern of nanowire shown in e)

SEM characterization of the thermolysis product following annealing at 590 °C is shown in Figure A.5d. TEM characterization of an isolated nanowire with the corresponding SAED is shown in Figures A.5e and f. The zone axis was determined to be [001] with the measured plane spacing ($d_{\{200\}}$ = 1.74 Å) in agreement with FCC Co ($d_{\{200\}}$ = 1.72 Å). We show that at the temperature extremes the 1D material crystal phase remained constant with lattice constant calculations matching FCC cobalt.

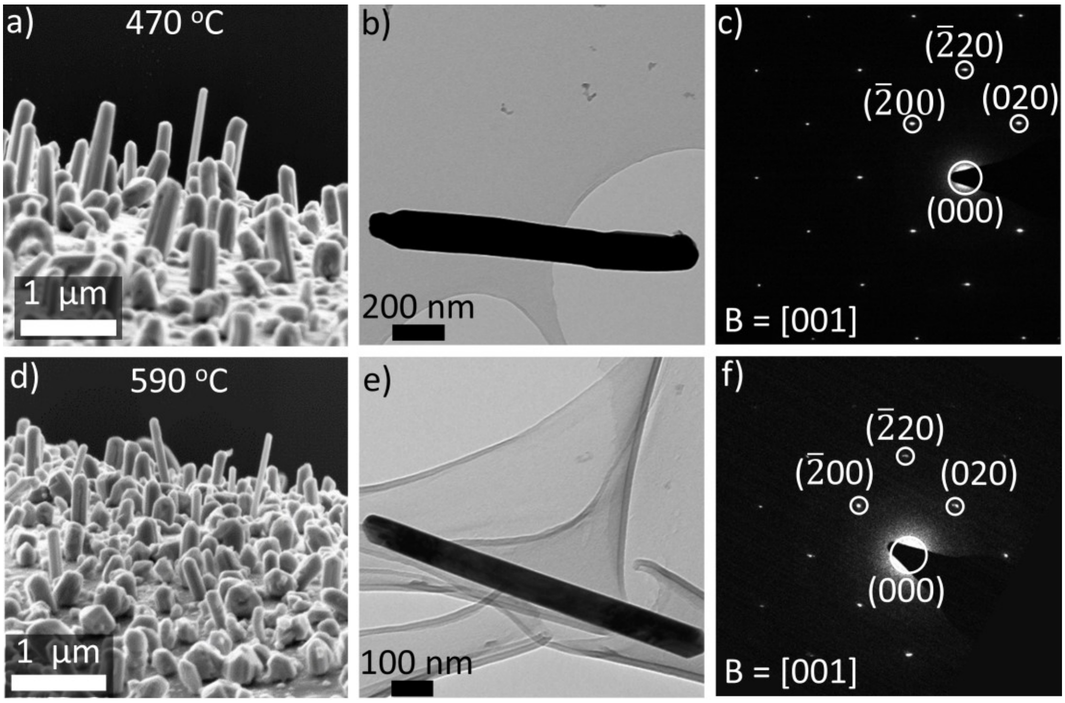

FIGURE A.5: a) Low magnification SEM image of Co nanowire grown at 470°C. b) TEM image of isolated Co nanorod transferred from a). c) SAED pattern of Co nanorod in b). d) SEM image of growth on substrate annealed at 590°C. e) TEM image of isolated nanowire from the substrate shown in d). f) SAED pattern of nanowire shown in e)

A.0.6 Nanowire Evolution Using Time-Dependent FESEM Characterization

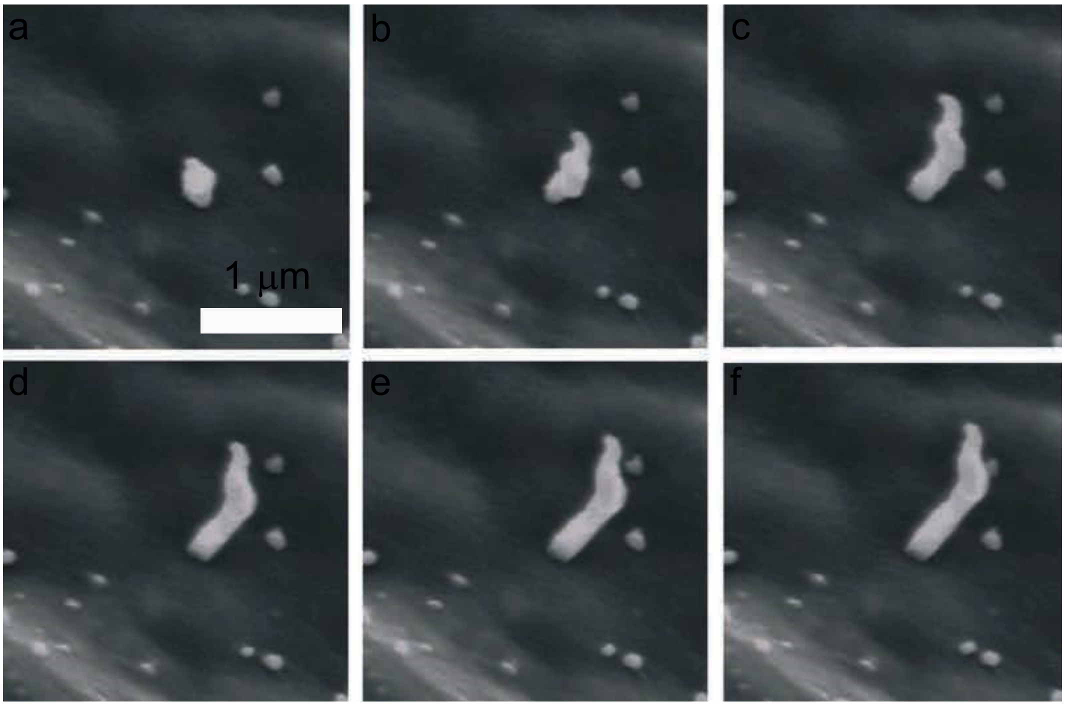

FIGURE A.6: In situ characterization during structure growth at a 540 °C.

Time-dependent SEM characterization during growth of a nanowire is shown in Figure A.6. The nanowire is shown to grow from the film with growth material incorporated at the based of the structure.

A.0.7 Ni_3S_2 and Ni Nanowire Diameter Histograms

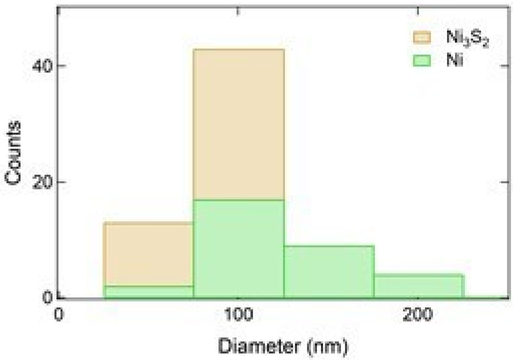

FIGURE A.7: Histograms showing Ni_3S_2 and Ni nanowire diameter distribution.

The diameter histograms for the Ni_3S_2 and Ni nanowire growths are shown in Figure A.7.

A.0.8 Characterization of the Cobalt-Complex

UV-vis absorbance spectra of the isolated cobalt(III) bis-cysteinate ($[Co^{III}Cys_2(H_2O)_2]$) (Figure A.8a) and both the 0.9 and 4.9 Co^{II}:Cys precursor solutions exhibit a low intensity band at 579 nm (ϵ = 406 $M^{-1}cm^{-1}$) and three medium intensity bands at 440 (ϵ = 1302 $M^{-1}cm^{-1}$), 350 (ϵ = 3476 $M^{-1}cm^{-1}$) and 280 nm (ϵ = 4600 $M^{-1}cm^{-1}$). The presence of four bands is characteristic of six coordinate Co^{III} complexes in an octahedral sphere which gives rise to the spin allowed ($^1A_{1g} \rightarrow {}^1T_{2g}$ and $^1A_{1g} \rightarrow {}^1T_{1g}$) and two spin forbidden ($^1A_{1g} \rightarrow {}^3T_{2g}$ and $^1A_{1g} \rightarrow {}^3T_{1g}$) transitions.[121] The multiple band at 515 nm due to the $^4T_{1g} \rightarrow {}^4T_{1g}(P)$ transition from $Co(H_2O)_6{}^{2+}$ in the cobalt(II) acetate solution is not observed as it is of low intensity (ϵ = 4.6 $M^{-1}cm^{-1}$) and obscured by the precursor complex.

The three broad d-d absorption bands at 680 nm, 460 and 375 nm for the 1.0, 3.9 and 4.9 (Ni^{II}:Cys) precursor solutions are assigned as the $^1A_{1g} \rightarrow {}^1A_{2g}$, $^1A_{1g} \rightarrow {}^1B_{1g}$ and $^1A_{1g} \rightarrow {}^1E_g$ transitions respectively.[120,45,8] These three bands are characteristic of square planar d8 nickel(II) complexes, and in agreement with the solid state structure of $Ni^{II}Cys_2$.[215] A band at 270 nm is attributed to intraligand transitions. The nickel(II) acetate bands expected at 395 (ϵ = 5.0 $M^{-1}cm^{-1}$), and 724 nm (ϵ = 2.0 $M^{-1}cm^{-1}$) due to the $^3A_{2g} \rightarrow {}^3T_{1g}(P)$ and $^3A_{2g} \rightarrow {}^3T_{1g}$ transition from $Ni(H_2O)_6{}^{2+}$ were not observed in the nanowire precursor solutions due to their low intensity.

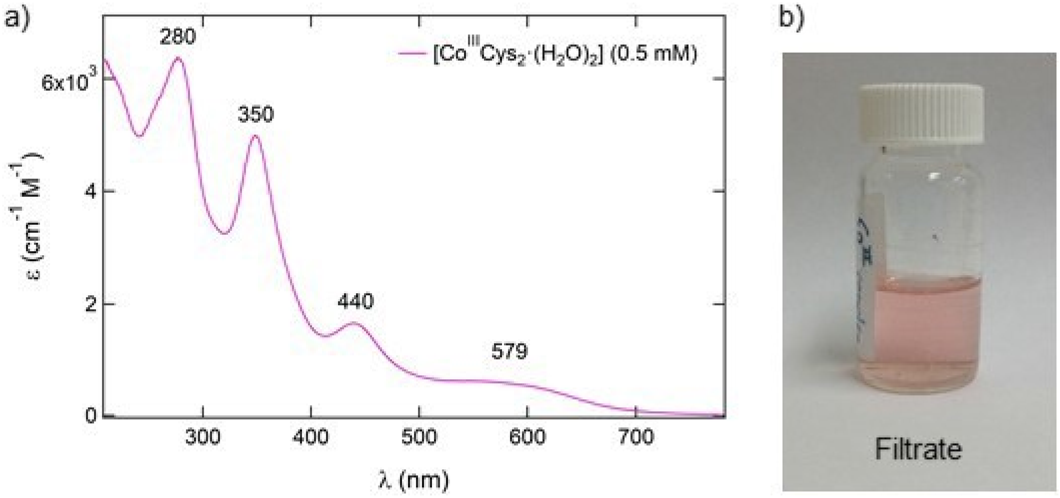

FIGURE A.8: a) UV-vis absorbance spectrum of the isolated Co^{III} bis-cysteinate complex in aqueous solution. b) Filtrate collected after isolating the Co^{III} bis-cysteinate from solution.

Appendix B

Appendix B

B.0.1 Nanoparticle Size Distribution Following Thermolysis of Different Precursor Mixtures

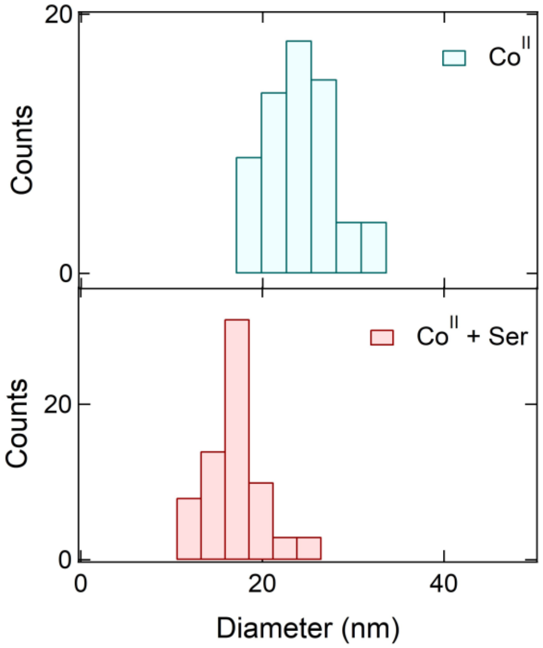

FIGURE B.1: Nanoparticle size distribution histogram following thermolysis experiments from a starting cobalt(II) acetate (blue) and serine/cobalt(II) acetate (red) precursor solutions.

B.0.2 System Pressure During Annealing in Butanethiol Environment

Figure B.2 shows the system pressure during annealing of samples in a butane thiol environment. Samples were loaded into the reaction chamber and purged with Ar for 30 min (500 sccm). Following purging the system was pumped to base pressure (3 x 10^{-2}) and butane thiol was introduced. Once

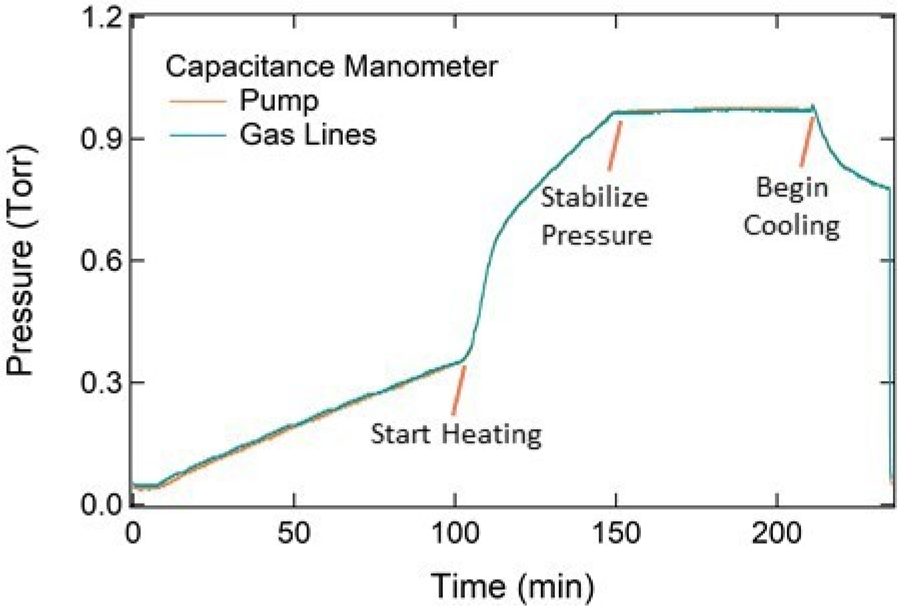

FIGURE B.2: Pressure recorded as a function of time during annealing in a butanethiol environment.

the pressure was greater than 0.3 Torr, the substrates were heated at a rate of 1 - 2 °C / sec to 600 °C. The temperature rise caused an increase in pressure. The annealing time was 1 hour at a stable temperature and pressure of 600 °C and ≈ 1 Torr, respectively. Following annealing the substrates were moved out from the furnace and cooled in a butane thiol environment. Once achieving room temperature residual butane thiol was pumped out, the system was purged with Ar then atmosphere at 1000 sccm for approximately 10 minutes each. Then the substrates were removed for characterization.

B.0.3 Butanethiol Versus Ammonium Vapor

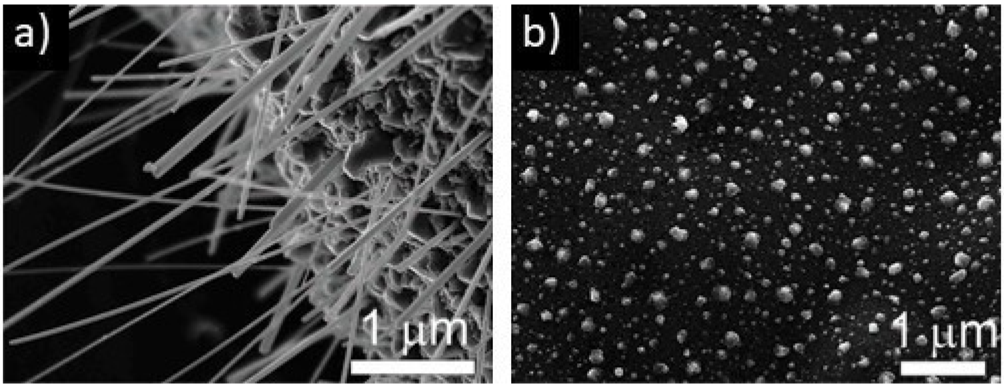

FIGURE B.3: SEM characterization of nanostructure morphology following annealing of a serine/cobalt(II) acetate precursor solution in a a) butanethiol and b) ammonia environment.

B.0.4 High Temperature CVD

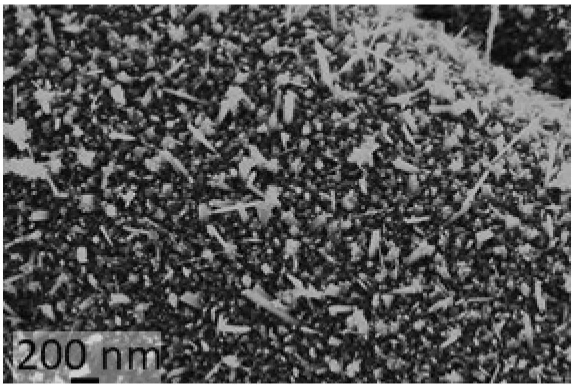

FIGURE B.4: SEM characterization of nanostructure morphology at the center of the carbon fiber substrate following high temperature CVD

B.0.5 Nanobelts

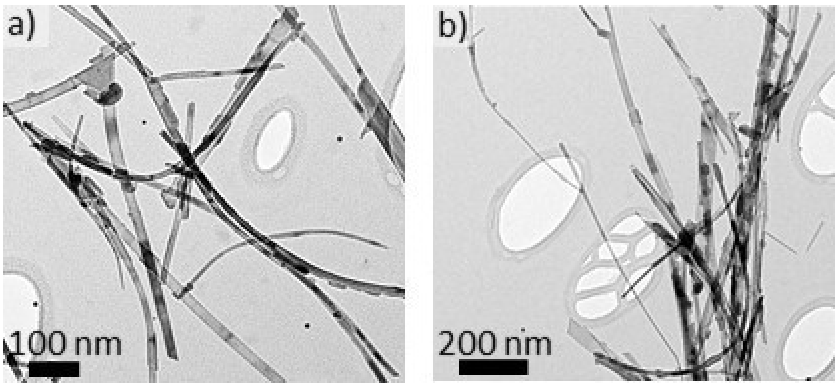

FIGURE B.5: TEM images of Co_9S_8 nanobelts.

Bibliography

[1] Mohammad Afzaal, Mohammad Azad Malik, and Paul O'Brien. "Chemical routes to chalcogenide materials as thin films or particles with critical dimensions with the order of nanometres". In: *Journal of Materials Chemistry* 20.20 (2010), pp. 4031–4040.

[2] PM Ajayan and LD Marks. "Quasimelting and phases of small particles". In: *Physical review letters* 60.7 (1988), p. 585.

[3] A Paul Alivisatos. "Semiconductor clusters, nanocrystals, and quantum dots". In: *science* 271.5251 (1996), pp. 933–937.

[4] Sengeni Anantharaj, Kannimuthu Karthick, and Subrata Kundu. "NiTe2 Nanowire Outperforms Pt/C in High-Rate Hydrogen Evolution at Extreme pH Conditions". In: *Inorganic chemistry* (2018).

[5] Thomas Audichon et al. "IrO2 coated on RuO2 as efficient and stable electroactive nanocatalysts for electrochemical water splitting". In: *The Journal of Physical Chemistry C* 120.5 (2016), pp. 2562–2573.

[6] Jinman Bai et al. "Co9S8@ MoS2 Core–Shell Heterostructures as Trifunctional Electrocatalysts for Overall Water Splitting and Zn–Air Batteries". In: *ACS applied materials & interfaces* 10.2 (2018), pp. 1678–1689.

[7] Narayan Baidya et al. "Synthesis, structure, and properties of potassium bis (L-cysteinato-N, S) nickelate (II) sesquihydrate". In: *Inorganic chemistry* 30.10 (1991), pp. 2448–2451.

[8] Subhash C Bajia and Anurag Mishra. "Synthesis and spectroscopic characterization of bis (N-alkyldithiocarbamato) nickel (II) complexes: crystal structures of [Ni (S2CNH (n-Pr)) 2] and [Ni (S2CNH (i-Pr)) 2]". In: *Journal of Coordination Chemistry* 64.15 (2011), pp. 2727–2734.

[9] Francesca Baletto and Riccardo Ferrando. "Structural properties of nanoclusters: Energetic, thermodynamic, and kinetic effects". In: *Reviews of modern physics* 77.1 (2005), p. 371.

[10] Amanda S Barnard. "Direct comparison of kinetic and thermodynamic influences on gold nanomorphology". In: *Accounts of chemical research* 45.10 (2012), pp. 1688–1697.

[11] Amanda S Barnard. "Using theory and modelling to investigate shape at the nanoscale". In: *Journal of Materials Chemistry* 16.9 (2006), pp. 813–815.

[12] Sven Barth et al. "Synthesis and applications of one-dimensional semiconductors". In: *Progress in Materials Science* 55.6 (2010), pp. 563–627.

[13] Clive R Bealing et al. "Predicting nanocrystal shape through consideration of surface-ligand interactions". In: *ACS nano* 6.3 (2012), pp. 2118–2127.

[14] David C Bell et al. "Imaging and analysis of nanowires". In: *Microscopy research and technique* 64.5-6 (2004), pp. 373–389.

[15] Abhijit Biswas et al. "Advances in top–down and bottom–up surface nanofabrication: Techniques, applications & future prospects". In: *Advances in colloid and interface science* 170.1-2 (2012), pp. 2–27.

[16] MT Björk et al. "Nanowire resonant tunneling diodes". In: *Applied Physics Letters* 81.23 (2002), pp. 4458–4460.

[17] MT Björk et al. "Si–InAs heterojunction Esaki tunnel diodes with high current densities". In: *Applied Physics Letters* 97.16 (2010), p. 163501.

[18] Carole Bresson et al. "A combined spectroscopic and theoretical approach to investigate structural properties of Co (II)/Co (III) tris-cysteinato complexes in aqueous medium". In: *New Journal of Chemistry* 31.10 (2007), pp. 1789–1797.

[19] John T Brosnan and Margaret E Brosnan. "The sulfur-containing amino acids: an overview". In: *The Journal of nutrition* 136.6 (2006), 1636S–1640S.

[20] M Brust, M Walker, and D Bethell. "DJ: Schiffrin and R. Whyman". In: *J. Chem. Soc. Chem. Commun* 801.3 (1994).

[21] Mathias Brust et al. "Synthesis of thiol-derivatised gold nanoparticles in a two-phase liquid–liquid system". In: *Journal of the Chemical Society, Chemical Communications* 7 (1994), pp. 801–802.

[22] W-K_ Burton, N Cabrera, and FC Frank. "The growth of crystals and the equilibrium structure of their surfaces". In: *Phil. Trans. R. Soc. Lond. A* 243.866 (1951), pp. 299–358.

[23] Pingqiang Cai et al. "Programmable Nano–Bio Interfaces for Functional Biointegrated Devices". In: *Advanced Materials* (2017).

[24] Huaqiang Cao. *Synthesis and Applications of Inorganic Nanostructures*. John Wiley & Sons, 2017.

[25] Keith T Chan et al. "Oriented growth of single-crystal Ni nanowires onto amorphous SiO2". In: *Nano letters* 10.12 (2010), pp. 5070–5075.

[26] Debraj Chandra et al. "Open pore architecture of an ordered mesoporous IrO_2 thin film for highly efficient electrocatalytic water oxidation". In: *ChemSusChem* 8.5 (2015), pp. 795–799.

[27] Shu-Hao Chang et al. "Gram-scale synthesis of catalytic Co9S8 nanocrystal ink as a cathode material for spray-deposited, large-area dye-sensitized solar cells". In: *ACS nano* 7.10 (2013), pp. 9443–9451.

[28] Chang Chen et al. "Preparation of hollow Co 9 S 8 nanoneedle arrays as effective counter electrodes for quantum dot-sensitized solar cells". In: *Journal of Materials Chemistry A* 3.12 (2015), pp. 6311–6314.

[29] Hsin-Wei Chen et al. "Plastic based dye-sensitized solar cells using Co 9 S 8 acicular nanotube arrays as the counter electrode". In: *Journal of Materials Chemistry A* 1.44 (2013), pp. 13759–13768.

[30] Pengzuo Chen et al. "3D Nitrogen-Anion-Decorated Nickel Sulfides for Highly Efficient Overall Water Splitting". In: *Advanced Materials* 29.30 (2017).

[31] Ziliang Chen et al. "General Synthesis of Dual Carbon-Confined Metal Sulfides Quantum Dots Toward High-Performance Anodes for Sodium-Ion Batteries". In: *Advanced Functional Materials* 27.38 (2017).

[32] Fangyi Cheng et al. "Template-directed materials for rechargeable lithium-ion batteries". In: *Chemistry of Materials* 20.3 (2007), pp. 667–681.

[33] A. A. Chernov. "The spiral growth of crystals". In: *Phys. Usp.* 4.1 (1961), pp. 116–148. DOI: `10.1070/PU1961v004n01ABEH003328`. URL: `https://ufn.ru/en/articles/1961/1/f/`.

[34] Kyung-Sang Cho et al. "Designing PbSe nanowires and nanorings through oriented attachment of nanoparticles". In: *Journal of the American Chemical Society* 127.19 (2005), pp. 7140–7147.

[35] Heon-Jin Choi. "Vapor–liquid–solid growth of semiconductor nanowires". In: *Semiconductor Nanostructures for Optoelectronic Devices*. Springer, 2012, pp. 1–36.

[36] Hyungsoo Choi and Sung-Ho Park. "Seedless growth of free-standing copper nanowires by chemical vapor deposition". In: *Journal of the American Chemical Society* 126.20 (2004), pp. 6248–6249.

[37] Phillip Christopher and Suljo Linic. "Engineering selectivity in heterogeneous catalysis: Ag nanowires as selective ethylene epoxidation catalysts". In: *Journal of the American Chemical Society* 130.34 (2008), pp. 11264–11265.

[38] National Research Council et al. *The role of the chemical sciences in finding alternatives to critical resources: A workshop summary*. National Academies Press, 2012.

[39] Yi Cui et al. "Nanowire nanosensors for highly sensitive and selective detection of biological and chemical species". In: *Science* 293.5533 (2001), pp. 1289–1292.

[40] Ronan Daly et al. "Chemical nano-gardens: growth of salt nanowires from supramolecular self-assembly gels". In: *ACS nano* 7.6 (2013), pp. 4838– 4845.

[41] Marie-Christine Daniel and Didier Astruc. "Gold nanoparticles: assembly, supramolecular chemistry, quantum-size-related properties, and applications toward biology, catalysis, and nanotechnology". In: *Chemical reviews* 104.1 (2004), pp. 293–346.

[42] Juan C De Jesus et al. "Thermal decomposition of nickel acetate tetrahydrate: an integrated study by TGA, QMS and XPS techniques". In: *Journal of Molecular Catalysis A: Chemical* 228.1-2 (2005), pp. 283–291.

[43] James J De Yoreo and Peter G Vekilov. "Principles of crystal nucleation and growth". In: *Reviews in mineralogy and geochemistry* 54.1 (2003), pp. 57–93.

[44] Yong Ding and Zhong Lin Wang. "Structure Analysis of Nanowires and Nanobelts by Transmission Electron Microscopy". In: *The Journal of Physical Chemistry B* 108.33 (2004), pp. 12280–12291.

[45] R Dingle. "Electronic spectrum of crystalline bis (diethyldithiocarbamato) nickel (II)". In: *Inorganic Chemistry* 10.6 (1971), pp. 1141–1144.

[46] Harald Ditlbacher et al. "Silver nanowires as surface plasmon resonators". In: *Physical review letters* 95.25 (2005), p. 257403.

[47] Xiaochen Dong et al. "Hybrid structure of zinc oxide nanorods and three dimensional graphene foam for supercapacitor and electrochemical sensor applications". In: *RSC Advances* 2.10 (2012), pp. 4364–4369.

[48] Gaohui Du, Wenzhi Li, and Yanqing Liu. "Filling carbon nanotubes with Co9S8 nanowires through in situ catalyst transition and extrusion". In: *The Journal of Physical Chemistry C* 112.6 (2008), pp. 1890–1895.

[49] Fabien Dubois et al. "A versatile strategy for quantum dot ligand exchange". In: *Journal of the American Chemical Society* 129.3 (2007), pp. 482–483.

[50] Frédéric Dumestre et al. "Shape control of thermodynamically stable cobalt nanorods through organometallic chemistry". In: *Angewandte Chemie International Edition* 41.22 (2002), pp. 4286–4289.

[51] Joel van Embden, Anthony SR Chesman, and Jacek J Jasieniak. "The heat-up synthesis of colloidal nanocrystals". In: *Chemistry of Materials* 27.7 (2015), pp. 2246–2285.

[52] Joel van Embden et al. "Evolution of colloidal nanocrystals: theory and modeling of their nucleation and growth". In: *The Journal of Physical Chemistry C* 113.37 (2009), pp. 16342–16355.

[53] Stephen A Empedocles et al. "Photoluminescence from single semiconductor nanostructures". In: *Advanced materials* 11.15 (1999), pp. 1243–1256.

[54] Deniz Erdemir, Alfred Y Lee, and Allan S Myerson. "Nucleation of crystals from solution: classical and two-step models". In: *Accounts of chemical research* 42.5 (2009), pp. 621–629.

[55] Elif Ertekin et al. "Equilibrium limits of coherency in strained nanowire heterostructures". In: *Journal of Applied Physics* 97.11 (2005), p. 114325.

[56] Bradley Fahlman. *Materials Chemistry*. Springer, 2007.

[57] Haosen Fan et al. "Controllable preparation of square nickel chalcogenide (NiS and NiSe2) nanoplates for superior Li/Na ion storage properties". In: *ACS applied materials & interfaces* 8.38 (2016), pp. 25261–25267.

[58] Yurui Fang and Mengtao Sun. "Nanoplasmonic waveguides: towards applications in integrated nanophotonic circuits". In: *Light: Science & Applications* 4.6 (2015), e294.

[59] Michael Faraday et al. "X. The Bakerian Lecture.—Experimental relations of gold (and other metals) to light". In: *Philosophical Transactions of the Royal Society of London* 147 (1857), pp. 145–181.

[60] Nathaniel J Freymeyer et al. "Influence of solvent reducing ability on copper sulfide crystal phase". In: *Crystal Growth & Design* 13.9 (2013), pp. 4059–4065.

[61] Kinjal Gandha et al. "High energy product developed from cobalt nanowires". In: *Scientific reports* 4 (2014), p. 5345.

[62] Mingyuan Gao et al. "Strongly photoluminescent CdTe nanocrystals by proper surface modification". In: *The Journal of Physical Chemistry B* 102.43 (1998), pp. 8360–8363.

[63] Dylan C Gary et al. "Investigating the role of amine in InP nanocrystal synthesis: destabilizing cluster intermediates by Z-type ligand displacement". In: *Chemical Communications* 53.1 (2017), pp. 161–164.

[64] Ehud Gazit. "Use of biomolecular templates for the fabrication of metal nanowires". In: *The FEBS journal* 274.2 (2007), pp. 317–322.

[65] V Germain et al. "Stacking faults in formation of silver nanodisks". In: *The Journal of Physical Chemistry B* 107.34 (2003), pp. 8717–8720.

[66] Ali Ghezelbash, Michael B Sigman, and Brian A Korgel. "Solventless synthesis of nickel sulfide nanorods and triangular nanoprisms". In: *Nano Letters* 4.4 (2004), pp. 537–542.

[67] J W Gibbs. "On the equilibrium of heterogeneous substances". In: *Transactions of the Connecticut Academy of Arts and Sciences* 3 (2009), pp. 108–248.

[68] Josiah Willard Gibbs. *On the equilibrium of heterogeneous substances*. Connecticut Academy, 1878.

[69] Michael Giersig and Paul Mulvaney. "Preparation of ordered colloid monolayers by electrophoretic deposition". In: *Langmuir* 9.12 (1993), pp. 3408–3413.

[70] Kyle D Gilroy et al. "Symmetry breaking during nanocrystal growth". In: *Chemical Communications* 53.33 (2017), pp. 4530–4541.

[71] Matthew BE Griffiths et al. "Surfactant directed growth of gold metal nanoplates by chemical vapor deposition". In: *Chemistry of Materials* 27.17 (2015), pp. 6116–6124.

[72] Robin W Grimes and Andrew N Fitch. "Thermal decomposition of cobalt (II) acetate tetrahydrate studied with time-resolved neutron diffraction and thermogravimetric analysis". In: *Journal of Materials Chemistry* 1.3 (1991), pp. 461–468.

[73] N Grobert et al. “Enhanced magnetic coercivities in Fe nanowires”. In: *Applied Physics Letters* 75.21 (1999), pp. 3363–3365.

[74] Yijun Guo et al. “Shape-programmed nanofabrication: Understanding the reactivity of dichalcogenide precursors”. In: *ACS nano* 7.4 (2013), p. 3616.

[75] Ajay Kumar Gupta and Mona Gupta. “Synthesis and surface engineering of iron oxide nanoparticles for biomedical applications”. In: *Biomaterials* 26.18 (2005), pp. 3995–4021.

[76] Don-Hyung Ha, Mohammad A Islam, and Richard D Robinson. “Binder-free and carbon-free nanoparticle batteries: a method for nanoparticle electrodes without polymeric binders or carbon black”. In: *Nano letters* 12.10 (2012), pp. 5122–5130.

[77] Leslie S Hamachi et al. “Kinetic Control over CdS Nanocrystal Nucleation Using a Library of Thiocarbonates, Thiocarbamates, and Thioureas”. In: *Chemistry of Materials* 29.20 (2017), pp. 8711–8719.

[78] JB Hannon et al. “The influence of the surface migration of gold on the growth of silicon nanowires”. In: *nature* 440.7080 (2006), p. 69.

[79] Gordon B Haxel et al. *Rare earth elements: critical resources for high technology*. Tech. rep. 2002.

[80] Weidong He et al. “Ultrathin and Porous Ni_3S_2/$CoNi_2S_4$ 3D-Network Structure for Superhigh Energy Density Asymmetric Supercapacitors”. In: *Advanced Energy Materials* 7.21 (2017).

[81] PC Healy et al. “Alkyl substituent effects in diamagnetic dithiocarbamate cobalt (III) and nickel (II) complexes”. In: *Australian Journal of Chemistry* 43.6 (1990), pp. 1083–1095.

[82] Mark P Hendricks et al. “A tunable library of substituted thiourea precursors to metal sulfide nanocrystals”. In: *Science* 348.6240 (2015), pp. 1226–1230.

[83] A Henglein. “Photochemistry of colloidal cadmium sulfide. 2. Effects of adsorbed methyl viologen and of colloidal platinum”. In: *The Journal of Physical Chemistry* 86.13 (1982), pp. 2291–2293.

[84] Conyers Herring. “Some theorems on the free energies of crystal surfaces”. In: *Physical review* 82.1 (1951), p. 87.

[85] Philip G Hill. “Condensation of water vapour during supersonic expansion in nozzles”. In: *Journal of Fluid Mechanics* 25.3 (1966), pp. 593–620.

[86] Rasmus Himstedt et al. “Localized Surface Plasmon Resonances of Various Nickel Sulfide Nanostructures and Au–Ni_3S_2 Core–Shell Nanoparticles”. In: *Chemistry of Materials* 29.17 (2017), pp. 7371–7377.

[87] Richard G Hobbs, Nikolay Petkov, and Justin D Holmes. “Semiconductor nanowire fabrication by bottom-up and top-down paradigms”. In: *Chemistry of Materials* 24.11 (2012), pp. 1975–1991.

[88] Yang Hou et al. “Integrated Hierarchical Cobalt Sulfide/Nickel Selenide Hybrid Nanosheets as an Efficient Three-dimensional Electrode for Electrochemical and Photoelectrochemical Water Splitting”. In: *Nano letters* 17.7 (2017), pp. 4202–4209.

[89] Michael H Huang et al. “Room-temperature ultraviolet nanowire nanolasers”. In: *science* 292.5523 (2001), pp. 1897–1899.

[90] Senchuan Huang et al. “N-, O-, and S-Tridoped Carbon-Encapsulated Co9S8 Nanomaterials: Efficient Bifunctional Electrocatalysts for Overall Water Splitting”. In: *Advanced Functional Materials* 27.17 (2017).

[91] Xing Huang et al. “In Situ Scanning Electron Microscopy Observation of Growth Kinetics and Catalyst Splitting in Vapor–Liquid–Solid Growth of Nanowires”. In: *Advanced Functional Materials* 25.37 (2015), pp. 5979–5987.

[92] Jerome K Hyun, Shixiong Zhang, and Lincoln J Lauhon. “Nanowire heterostructures”. In: *Annual Review of Materials Research* 43 (2013), pp. 451–479.

[93] E Ingier-Stocka and A Grabowska. “Thermal analysis of cobalt (II) salts with some carboxylic acids”. In: *Journal of thermal analysis and calorimetry* 54.1 (1998), pp. 115–123.

[94] United States National Nanotechnology Initiative et al. *What’s so special about the nanoscale?*

[95] Yong Jiang et al. “Solvent influence on the role of thiols in growth of thiols-capped Au nanocrystals”. In: *The Journal of Physical Chemistry C* 118.1 (2013), pp. 714–719.

[96] Lihong Jing et al. “Aqueous based semiconductor nanocrystals”. In: *Chemical reviews* 116.18 (2016), pp. 10623–10730.

[97] Young-wook Jun et al. "Surfactant-assisted elimination of a high energy facet as a means of controlling the shapes of TiO2 nanocrystals". In: *Journal of the American Chemical Society* 125.51 (2003), pp. 15981–15985.

[98] Young-wook Jun et al. *Symmetry-controlled colloidal nanocrystals: nonhydrolytic chemical synthesis and shape determining parameters*. 2005.

[99] Yun Ku Jung, Jae Il Kim, and Jin-Kyu Lee. "Thermal decomposition mechanism of single-molecule precursors forming metal sulfide nanoparticles". In: *Journal of the American Chemical Society* 132.1 (2009), pp. 178–184.

[100] Taejoon Kang et al. "Patterned multiplex pathogen DNA detection by Au particle-on-wire SERS sensor". In: *Nano letters* 10.4 (2010), pp. 1189–1193.

[101] D Kashchiev and GM Van Rosmalen. "Nucleation in solutions revisited". In: *Crystal Research and Technology* 38.7-8 (2003), pp. 555–574.

[102] Ladan Khaksar and John Shirokoff. "Effect of elemental sulfur and sulfide on the corrosion behavior of Cr-Mo low alloy steel for tubing and tubular components in oil and gas industry". In: *Materials* 10.4 (2017), p. 430.

[103] Dmitri S Kilin, Oleg V Prezhdo, and Younan Xia. "Shape-controlled synthesis of silver nanoparticles: Ab initio study of preferential surface coordination with citric acid". In: *Chemical Physics Letters* 458.1-3 (2008), pp. 113–116.

[104] BJ Kim et al. "Kinetics of individual nucleation events observed in nanoscale vapor-liquid-solid growth". In: *Science* 322.5904 (2008), pp. 1070–1073.

[105] Changwook Kim et al. "Copper Nanowires with a Five-Twinned Structure Grown by Chemical Vapor Deposition". In: *Advanced Materials* 20.10 (2008), pp. 1859–1863.

[106] Kyungnam Kim et al. "Halide–Amine Co-Passivated Indium Phosphide Colloidal Quantum Dots in Tetrahedral Shape". In: *Angewandte Chemie International Edition* 55.11 (2016), pp. 3714–3718.

[107] Myung Jun Kim et al. "Ethylenediamine Promotes Cu Nanowire Growth by Inhibiting Oxidation of Cu (111)". In: *Journal of the American Chemical Society* 139.1 (2016), pp. 277–284.

[108] Si-in Kim et al. “Epitaxy-driven vertical growth of single-crystalline cobalt nanowire arrays by chemical vapor deposition”. In: *Journal of Materials Chemistry C* 3.1 (2015), pp. 100–106.

[109] Mato Knez et al. “Biotemplate synthesis of 3-nm nickel and cobalt nanowires”. In: *Nano letters* 3.8 (2003), pp. 1079–1082.

[110] Roshan H Kore, Jaideep S Kulkarni, and Santosh K Haram. “Effect of nonionic surfactants on the kinetics of disproportion of copper sulfide nanoparticles in the aqueous sols”. In: *Chemistry of materials* 13.5 (2001), pp. 1789–1793.

[111] KR Krishnadas, PR Sajanlal, and T Pradeep. “Pristine and hybrid nickel nanowires: Template-, magnetic field-, and surfactant-free wet chemical synthesis and Raman studies”. In: *The Journal of Physical Chemistry C* 115.11 (2011), pp. 4483–4490.

[112] Satyanarayana VNT Kuchibhatla et al. “One dimensional nanostructured materials”. In: *Progress in materials science* 52.5 (2007), pp. 699–913.

[113] Chen-Ho Lai, Ming-Yen Lu, and Lih-Juann Chen. “Metal sulfide nanostructures: synthesis, properties and applications in energy conversion and storage”. In: *Journal of Materials Chemistry* 22.1 (2012), pp. 19–30.

[114] Adrian KY Lam, Victor Ryzhov, and AJ Richard. “Mobile protons versus mobile radicals: Gas-phase unimolecular chemistry of radical cations of cysteine-containing peptides”. In: *Journal of the American Society for Mass Spectrometry* 21.8 (2010), pp. 1296–1312.

[115] Travis H Larsen et al. “Solventless synthesis of copper sulfide nanorods by thermolysis of a single source thiolate-derived precursor”. In: *Journal of the American Chemical Society* 125.19 (2003), pp. 5638–5639.

[116] Matt Law, Joshua Goldberger, and Peidong Yang. “Semiconductor nanowires and nanotubes”. In: *Annu. Rev. Mater. Res.* 34 (2004), pp. 83–122.

[117] Matt Law et al. “Nanowire dye-sensitized solar cells”. In: *Nature materials* 4.6 (2005), p. 455.

[118] Jia Le Xie, Chun Xian Guo, and Chang Ming Li. “Construction of one-dimensional nanostructures on graphene for efficient energy conversion and storage”. In: *Energy & Environmental Science* 7.8 (2014), pp. 2559–2579.

[119] Daniel V Leff, Lutz Brandt, and James R Heath. “Synthesis and characterization of hydrophobic, organically-soluble gold nanocrystals functionalized with primary amines”. In: *Langmuir* 12.20 (1996), pp. 4723–4730.

[120] ABP Lever et al. “Electronic spectra of dn ions”. In: *Inorganic electronic spectroscopy* 2 (1984).

[121] Alfred Beverley Philip Lever. *Inorganic electronic spectroscopy*. Elsevier, 1968.

[122] Bo Li et al. “Synthesis and purification of silver nanowires to make conducting films with a transmittance of 99%”. In: *Nano letters* 15.10 (2015), pp. 6722–6726.

[123] Hao Li et al. “Carbon Nanotubes Rooted in Porous Ternary Metal Sulfide@N/S-Doped Carbon Dodecahedron: Bimetal-Organic-Frameworks Derivation and Electrochemical Application for High-Capacity and Long-Life Lithium-Ion Batteries”. In: *Advanced Functional Materials* 26.45 (2016), pp. 8345–8353.

[124] Hao Li et al. “Vapor-phase atomic layer deposition of Co9S8 and its application for supercapacitors”. In: *Nano letters* 15.10 (2015), pp. 6689–6695.

[125] Hongbo Li et al. “Size-and shape-controlled synthesis of PbSe and PbS nanocrystals via a facile method”. In: *CrystEngComm* 12.4 (2010), pp. 1127–1133.

[126] Tingkai Li, Michael Mastro, and Armin Dadgar. *III–V compound semiconductors: integration with silicon-based microelectronics*. CRC press, 2010.

[127] Nikolaos Liakakos et al. “Solution epitaxial growth of cobalt nanowires on crystalline substrates for data storage densities beyond 1 Tbit/in2”. In: *Nano letters* 14.6 (2014), pp. 3481–3486.

[128] Chia-Cheng Lin, Shannon J Tan, and Javier Vela. “Chalcogenide and pnictide nanocrystals from the silylative deoxygenation of metal oxides”. In: *Journal of Materials Chemistry A* 5.38 (2017), pp. 20351–20358.

[129] Stephan Link, MB Mohamed, and MA El-Sayed. “Simulation of the optical absorption spectra of gold nanorods as a function of their aspect ratio and the effect of the medium dielectric constant”. In: *The Journal of Physical Chemistry B* 103.16 (1999), pp. 3073–3077.

[130] Haitao Liu, Jonathan S Owen, and A Paul Alivisatos. "Mechanistic study of precursor evolution in colloidal group II- VI semiconductor nanocrystal synthesis". In: *Journal of the American Chemical Society* 129.2 (2007), pp. 305–312.

[131] Mingyang Liu et al. "Probing intermediates of the induction period prior to nucleation and growth of semiconductor quantum dots". In: *Nature communications* 8 (2017), p. 15467.

[132] Siqi Liu et al. "One-dimension-based spatially ordered architectures for solar energy conversion". In: *Chemical Society Reviews* 44.15 (2015), pp. 5053–5075.

[133] YQ Liu et al. "Facile microwave-assisted synthesis of uniform single-crystal copper nanowires with excellent electrical conductivity". In: *Chem Commun* 46 (2012), pp. 2277–2279.

[134] N Duane Loh et al. "Multistep nucleation of nanocrystals in aqueous solution". In: *Nature chemistry* 9.1 (2017), p. 77.

[135] Wei Lu and Charles M Lieber. "Nanoelectronics from the bottom up". In: *Nature materials* 6.11 (2007), p. 841.

[136] Xianmao Lu et al. "Ultrathin gold nanowires can be obtained by reducing polymeric strands of oleylamine- AuCl complexes formed via aurophilic interaction". In: *Journal of the American Chemical Society* 130.28 (2008), pp. 8900–8901.

[137] Yanyun Ma et al. "Synthesis of Trisoctahedral Gold Nanocrystals with Exposed High-Index Facets by a Facile Chemical Method". In: *Angewandte Chemie International Edition* 47.46 (2008), pp. 8901–8904.

[138] Liqiang Mai et al. "Nanowire electrodes for electrochemical energy storage devices". In: *Chemical reviews* 114.23 (2014), pp. 11828–11862.

[139] Max N Mankin et al. "Facet-selective epitaxy of compound semiconductors on faceted silicon nanowires". In: *Nano letters* 15.7 (2015), pp. 4776–4782.

[140] Maria Jose Martinez-Perez et al. "NanoSQUID magnetometry on individual as-grown and annealed Co nanowires at variable temperature". In: *Nano letters* 18.12 (2018), pp. 7674–7682.

[141] BGYYYXB Mayers et al. "Large-Scale Synthesis of Monodisperse Nanorods of Se/Te Alloys Through a Homogeneous Nucleation and Solution Growth Process". In: *Advanced materials* 13.18 (2001), pp. 1380–1384.

[142] JP McCaffrey and J-M Baribeau. "A transmission electron microscope (TEM) calibration standard sample for all magnification, camera constant, and image/diffraction pattern rotation calibrations". In: *Microscopy research and technique* 32.5 (1995), pp. 449–454.

[143] Xinghua Meng and Da Deng. "Trash to treasure: waste eggshells used as reactor and template for synthesis of Co9S8 nanorod arrays on carbon fibers for energy storage". In: *Chemistry of Materials* 28.11 (2016), pp. 3897–3904.

[144] Michael Mertig et al. "DNA as a selective metallization template". In: *Nano Letters* 2.8 (2002), pp. 841–844.

[145] M Mohamed, S Halawy, and M Ebrahim. "The non-isothermal decomposition of cobalt acetate tetrahydrate: a kinetic and thermodynamic study". In: *Journal of Thermal Analysis and Calorimetry* 41.2-3 (1994), pp. 387–404.

[146] Melinda Mohl et al. "Low-temperature large-scale synthesis and electrical testing of ultralong copper nanowires". In: *Langmuir* 26.21 (2010), pp. 16496–16502.

[147] Christopher F Monson and Adam T Woolley. "DNA-templated construction of copper nanowires". In: *Nano letters* 3.3 (2003), pp. 359–363.

[148] Stefanos Mourdikoudis and Luis M Liz-Marzán. "Oleylamine in nanoparticle synthesis". In: *Chemistry of Materials* 25.9 (2013), pp. 1465–1476.

[149] Aiman Mukhtar et al. "Effect of Co2+ concentration on the crystal structure of electrodeposited Co nanowires". In: *Journal of Crystal Growth* 441 (2016), pp. 26–32.

[150] CBea Murray, David J Norris, and Moungi G Bawendi. "Synthesis and characterization of nearly monodisperse CdE (E= sulfur, selenium, tellurium) semiconductor nanocrystallites". In: *Journal of the American Chemical Society* 115.19 (1993), pp. 8706–8715.

[151] Christopher B Murray, CR Kagan, and MG Bawendi. "Synthesis and characterization of monodisperse nanocrystals and close-packed nanocrystal assemblies". In: *Annual Review of Materials Science* 30.1 (2000), pp. 545–610.

[152] Tashi Nautiyal, TH Rho, and Kwang S Kim. "Nanowires for spintronics: A study of transition-metal elements of groups 8–10". In: *Physical Review B* 69.19 (2004), p. 193404.

[153] Sebastian Neusser and Dirk Grundler. “Magnonics: spin waves on the nanoscale”. In: *Advanced Materials* 21.28 (2009), pp. 2927–2932.

[154] Roy G Neville and George Gorin. “Cysteine Complexes with the Cobalt(III) Ion. II. Spectrophotometric Study of the Nature of Coordination in the Complexes of Cysteine with the Cobalt(III) Ion”. In: *Journal of the American Chemical Society* 78.19 (1956), pp. 4893–4896.

[155] Yao Nie, Li Li, and Zidong Wei. “Recent advancements in Pt and Pt-free catalysts for oxygen reduction reaction”. In: *Chemical Society Reviews* 44.8 (2015), pp. 2168–2201.

[156] Wilhelm Ostwald. “Studien über die Bildung und Umwandlung fester Körper”. In: *Zeitschrift für physikalische Chemie* 22.1 (1897), pp. 289–330.

[157] Jonathan S Owen et al. “Precursor conversion kinetics and the nucleation of cadmium selenide nanocrystals”. In: *Journal of the American Chemical Society* 132.51 (2010), pp. 18206–18213.

[158] United Kingdom Oxford. *Nucleation: Basic Theory with Applications*. Butterworth Heinemann, 1999.

[159] David W Oxtoby. “Nucleation of first-order phase transitions”. In: *Accounts of chemical research* 31.2 (1998), pp. 91–97.

[160] Geoffrey A Ozin et al. “Nanofabrication by self-assembly”. In: *Materials Today* 12.5 (2009), pp. 12–23.

[161] Jongnam Park et al. “Synthesis of monodisperse spherical nanocrystals”. In: *Angewandte Chemie International Edition* 46.25 (2007), pp. 4630–4660.

[162] Stewart F Parker. “Assignment of the vibrational spectrum of L-cysteine”. In: *Chemical Physics* 424 (2013), pp. 75–79.

[163] Stuart Parkin et al. “Magnetically engineered spintronic sensors and memory”. In: *Proceedings of the IEEE* 91.5 (2003), pp. 661–680.

[164] Stuart SP Parkin, Masamitsu Hayashi, and Luc Thomas. “Magnetic domain-wall racetrack memory”. In: *Science* 320.5873 (2008), pp. 190–194.

[165] SN Piramanayagam. “Perpendicular recording media for hard disk drives”. In: *Journal of Applied Physics* 102.1 (2007), p. 2.

[166] Jarryd J Pla et al. “A single-atom electron spin qubit in silicon”. In: *Nature* 489.7417 (2012), p. 541.

[167] Narayan Pradhan et al. "Surface ligand dynamics in growth of nanocrystals". In: *Journal of the American Chemical Society* 129.30 (2007), pp. 9500–9509.

[168] Jun Pu et al. "Co_9S_8 nanotube arrays supported on nickel foam for high-performance supercapacitors". In: *Physical Chemistry Chemical Physics* 16.2 (2014), pp. 785–791.

[169] Victor F Puntes et al. "Synthesis of hcp-Co nanodisks". In: *Journal of the American Chemical Society* 124.43 (2002), pp. 12874–12880.

[170] Lianhua Qu, W William Yu, and Xiaogang Peng. "In situ observation of the nucleation and growth of CdSe nanocrystals". In: *Nano Letters* 4.3 (2004), pp. 465–469.

[171] Zewei Quan, Yuxuan Wang, and Jiye Fang. "High-index faceted noble metal nanocrystals". In: *Accounts of chemical research* 46.2 (2012), pp. 191–202.

[172] CNR Rao and KPR Pisharody. "Transition metal sulfides". In: *Progress in Solid State Chemistry* 10 (1976), pp. 207–270.

[173] Aaron R Rathmell et al. "The growth mechanism of copper nanowires and their properties in flexible, transparent conducting films". In: *Advanced materials* 22.32 (2010), pp. 3558–3563.

[174] Reality Bytes. *Intel breaks another record is CPU size with 14nm process*. `https://realitybytesinc.com/blog/entry/intel-breaks-another-record-is-cpu-size-with-14nm-process`, Last accessed on 2018-02-30. 2017.

[175] Franz X Redl et al. "Three-dimensional binary superlattices of magnetic nanocrystals and semiconductor quantum dots". In: *Nature* 423.6943 (2003), p. 968.

[176] Peter Reiss et al. "Synthesis of semiconductor nanocrystals, focusing on nontoxic and earth-abundant materials". In: *Chemical reviews* 116.18 (2016), pp. 10731–10819.

[177] Jordan M Rhodes et al. "Phase-Controlled Colloidal Syntheses of Iron Sulfide Nanocrystals via Sulfur Precursor Reactivity and Direct Pyrite Precipitation". In: *Chemistry of Materials* 29.19 (2017), pp. 8521–8530.

[178] AL Rogach et al. "Synthesis and characterization of thiol-stabilized CdTe nanocrystals". In: *Berichte der Bunsengesellschaft für physikalische Chemie* 100.11 (1996), pp. 1772–1778.

[179] Andres La Rosa et al. "Top-down and Bottom-up approaches to nanotechnology An overview in the context of developing Proton-fountain Electric-field-assisted Nanolithography (PEN) : Fabrication of polymer nanostructures that respond to chemical and electrical stimuli". In: 2013.

[180] R Rossetti and L Brus. "Electron-hole recombination emission as a probe of surface chemistry in aqueous cadmium sulfide colloids". In: *The Journal of Physical Chemistry* 86.23 (1982), pp. 4470–4472.

[181] T Purnima A Ruberu et al. "Molecular control of the nanoscale: effect of phosphine–chalcogenide reactivity on CdS–CdSe nanocrystal composition and morphology". In: *ACS nano* 6.6 (2012), pp. 5348–5359.

[182] Xianhong Rui, Huiteng Tan, and Qingyu Yan. "Nanostructured metal sulfides for energy storage". In: *Nanoscale* 6.17 (2014), pp. 9889–9924.

[183] Matthew Rycenga et al. "Controlling the synthesis and assembly of silver nanostructures for plasmonic applications". In: *Chemical reviews* 111.6 (2011), pp. 3669–3712.

[184] Victor Ryzhov, Adrian KY Lam, and AJ Richard. "Gas-phase fragmentation of long-lived cysteine radical cations formed via NO loss from protonated S-nitrosocysteine". In: *Journal of the American Society for Mass Spectrometry* 20.6 (2009), pp. 985–995.

[185] E Sanz et al. "Homogeneous ice nucleation at moderate supercooling from molecular simulation". In: *Journal of the American Chemical Society* 135.40 (2013), pp. 15008–15017.

[186] Tapan K Sau and Catherine J Murphy. "Room temperature, high-yield synthesis of multiple shapes of gold nanoparticles in aqueous solution". In: *Journal of the American Chemical Society* 126.28 (2004), pp. 8648–8649.

[187] H Schmid et al. "Fabrication of vertical InAs-Si heterojunction tunnel field effect transistors". In: *Device Research Conference (DRC), 2011 69th Annual*. IEEE. 2011, pp. 181–182.

[188] Roy E Schreiber et al. "Real-time molecular scale observation of crystal formation". In: *Nature chemistry* 9.4 (2017), p. 369.

[189] Maxwell P Schubert. "Cobalt complexes of cysteine". In: *J. amer. chem. Soc* 53 (1931), pp. 3851–3861.

[190] Parag S Shah et al. “Role of steric stabilization on the arrested growth of silver nanocrystals in supercritical carbon dioxide”. In: *The Journal of Physical Chemistry B* 106.47 (2002), pp. 12178–12185.

[191] Cheng Shang and Zhi-Pan Liu. “Stochastic surface walking method for structure prediction and pathway searching”. In: *Journal of chemical theory and computation* 9.3 (2013), pp. 1838–1845.

[192] Reyimjan A Sidik and Alfred B Anderson. “Co9S8 as a catalyst for electroreduction of O2: quantum chemistry predictions”. In: *The Journal of Physical Chemistry B* 110.2 (2006), pp. 936–941.

[193] Michael B Sigman and Brian A Korgel. “Solventless synthesis of Bi2S3 (bismuthinite) nanorods, nanowires, and nanofabric”. In: *Chemistry of materials* 17.7 (2005), pp. 1655–1660.

[194] Michael B Sigman et al. “Solventless synthesis of monodisperse Cu2S nanorods, nanodisks, and nanoplatelets”. In: *Journal of the American Chemical Society* 125.51 (2003), pp. 16050–16057.

[195] Srikanth Singamaneni et al. “Magnetic nanoparticles: recent advances in synthesis, self-assembly and applications”. In: *Journal of Materials Chemistry* 21.42 (2011), pp. 16819–16845.

[196] Saujan V Sivaram et al. “Direct observation of transient surface species during Ge nanowire growth and their influence on growth stability”. In: *Journal of the American Chemical Society* 137.31 (2015), pp. 9861–9869.

[197] Andrew M Smith and Shuming Nie. “Semiconductor nanocrystals: structure, properties, and band gap engineering”. In: *Accounts of chemical research* 43.2 (2009), pp. 190–200.

[198] Nathan J Sniadecki et al. “Magnetic microposts as an approach to apply forces to living cells”. In: *Proceedings of the National Academy of Sciences* 104.37 (2007), pp. 14553–14558.

[199] Jae Hee Song et al. “MMo3Se3 (M= Li+, Na+, Rb+, Cs+, NMe4+) nanowire formation via cation exchange in organic solution”. In: *Journal of the American Chemical Society* 123.39 (2001), pp. 9714–9715.

[200] Yaghoub Soumare et al. “Kinetically Controlled Synthesis of Hexagonally Close-Packed Cobalt Nanorods with High Magnetic Coercivity”. In: *Advanced Functional Materials* 19.12 (2009), pp. 1971–1977.

[201] Jonathan S Steckel et al. “On the mechanism of lead chalcogenide nanocrystal formation”. In: *Journal of the American Chemical Society* 128.40 (2006), pp. 13032–13033.

[202] J Stejny, RW Trinder, and J Dlugosz. “Preparation and structure of poly (sulphur nitride) whiskers”. In: *Journal of Materials Science* 16.11 (1981), pp. 3161–3170.

[203] Kristian Storm et al. “Realizing lateral wrap-gated nanowire FETs: controlling gate length with chemistry rather than lithography”. In: *Nano letters* 12.1 (2011), pp. 1–6.

[204] Qingmei Su et al. “In situ transmission electron microscopy investiga- tion of the electrochemical lithiation–delithiation of individual Co9S8/Co-filled carbon nanotubes”. In: *ACS nano* 7.12 (2013), pp. 11379–11387.

[205] Yugang Sun and Younan Xia. “Mechanistic study on the replacement reaction between silver nanostructures and chloroauric acid in aqueous medium”. In: *Journal of the American Chemical Society* 126.12 (2004), pp. 3892–3901.

[206] Yugang Sun et al. “Polyol synthesis of uniform silver nanowires: a plausible growth mechanism and the supporting evidence”. In: *Nano letters* 3.7 (2003), pp. 955–960.

[207] Senthilarasu Sundaram, David Benson, and Tapas K Mallick. *Solar Photovoltaic Technology Production: Potential Environmental Impacts and Implications for Governance*. Academic Press, 2016.

[208] Andrea R Tao, Susan Habas, and Peidong Yang. “Shape control of colloidal metal nanocrystals”. In: *small* 4.3 (2008), pp. 310–325.

[209] Nguyen TK Thanh, N Maclean, and S Mahiddine. “Mechanisms of nucleation and growth of nanoparticles in solution”. In: *Chemical reviews* 114.15 (2014), pp. 7610–7630.

[210] Claes Thelander et al. “Single-electron transistors in heterostructure nanowires”. In: *Applied Physics Letters* 83.10 (2003), pp. 2052–2054.

[211] Jordan W Thomson et al. “From sulfur- amine solutions to metal sulfide nanocrystals: peering into the oleylamine- sulfur black box”. In: *Journal of the American Chemical Society* 133.13 (2011), pp. 5036–5041.

[212] GD THORN, RA LUDWIG, et al. “The dithiocarbamates and related compounds.” In: *The dithiocarbamates and related compounds.* (1962).

[213] T Thurn-Albrecht et al. “Ultrahigh-density nanowire arrays grown in self-assembled diblock copolymer templates”. In: *Science* 290.5499 (2000), pp. 2126–2129.

[214] Yuan Tian et al. "Ultrahigh-density sub-10 nm nanowire array formation via surface-controlled phase separation". In: *Nano letters* 14.8 (2014), pp. 4328–4333.

[215] Michael T Tiedemann. *Heme Binding and Transfer in the Isd Heme Scavenging Pathway of Staphylococcus aureus*. 2012.

[216] Jitendra N Tiwari, Rajanish N Tiwari, and Kwang S Kim. "Zero-dimensional, one-dimensional, two-dimensional and three-dimensional nanostructured materials for advanced electrochemical energy devices". In: *Progress in Materials Science* 57.4 (2012), pp. 724–803.

[217] WJ Tomlinson and DM Meades. "Elemental sulfur and the corrosion and cracking of type 304 stainless steel". In: *Corrosion* 47.4 (1991), pp. 269–271.

[218] James M Tour. "Top-down versus bottom-up fabrication of graphene-based electronics". In: *Chemistry of Materials* 26.1 (2013), pp. 163–171.

[219] David Tsivion and Ernesto Joselevich. "Guided growth of epitaxially coherent GaN nanowires on SiC". In: *Nano letters* 13.11 (2013), pp. 5491–5496.

[220] Chia-Kuang Tsung et al. "Selective shortening of single-crystalline gold nanorods by mild oxidation". In: *Journal of the American Chemical Society* 128.16 (2006), pp. 5352–5353.

[221] Rutger A Van Santen. "Complementary structure sensitive and insensitive catalytic relationships". In: *Accounts of chemical research* 42.1 (2008), pp. 57–66.

[222] Peter G Vekilov. "Dense liquid precursor for the nucleation of ordered solid phases from solution". In: *Crystal Growth & Design* 4.4 (2004), pp. 671–685.

[223] Peter G Vekilov. "Nucleation". In: *Crystal growth & design* 10.12 (2010), pp. 5007–5019.

[224] Peter G Vekilov. "The two-step mechanism of nucleation of crystals in solution". In: *Nanoscale* 2.11 (2010), pp. 2346–2357.

[225] B Viswanath et al. "Mechanistic aspects of shape selection and symmetry breaking during nanostructure growth by wet chemical methods". In: *The Journal of Physical Chemistry C* 113.39 (2009), pp. 16866–16883.

[226] T Vossmeyer et al. “CdS nanoclusters: synthesis, characterization, size dependent oscillator strength, temperature shift of the excitonic transition energy, and reversible absorbance shift”. In: *The Journal of Physical Chemistry* 98.31 (1994), pp. 7665–7673.

[227] RS Wagner and WC Ellis. “Vapor-liquid-solid mechanism of single crystal growth”. In: *Applied Physics Letters* 4.5 (1964), pp. 89–90.

[228] Jesper Wallentin and Magnus T Borgström. “Doping of semiconductor nanowires”. In: *Journal of Materials Research* 26.17 (2011), pp. 2142–2156.

[229] Michael J Walsh et al. “Symmetry breaking and silver in gold nanorod growth”. In: *ACS nano* 9.1 (2015), pp. 715–724.

[230] Qing Wan et al. “Fabrication and ethanol sensing characteristics of ZnO nanowire gas sensors”. In: *Applied Physics Letters* 84.18 (2004), pp. 3654–3656.

[231] Dong Wang and Didier Astruc. “The recent development of efficient Earth-abundant transition-metal nanocatalysts”. In: *Chemical Society Reviews* 46.3 (2017), pp. 816–854.

[232] Hailong Wang et al. “Atomistics of vapour–liquid–solid nanowire growth”. In: *Nature communications* 4 (2013), p. 1956.

[233] Jianfang Wang et al. “Highly polarized photoluminescence and photodetection from single indium phosphide nanowires”. In: *Science* 293.5534 (2001), pp. 1455–1457.

[234] Mingliang Wang et al. “Growth Orientation Control of Co Nanowires Fabricated by Electrochemical Deposition Using Porous Alumina Templates”. In: *Crystal Growth & Design* 18.1 (2017), pp. 479–487.

[235] Y Andrew Wang et al. “Stabilization of inorganic nanocrystals by organic dendrons”. In: *Journal of the American Chemical Society* 124.10 (2002), pp. 2293–2298.

[236] Yawen Wang et al. “Thermodynamics versus kinetics in nanosynthesis”. In: *Angewandte Chemie International Edition* 54.7 (2015), pp. 2022–2051.

[237] ZL Wang. *Transmission electron microscopy of shape-controlled nanocrystals and their assemblies*. 2000.

[238] T Wanjun and C Donghua. "Mechanism of thermal decomposition of cobalt acetate tetrahydrate". In: *Chemical Papers* 61.4 (2007), pp. 329–332.

[239] C-Y Wen et al. "Formation of compositionally abrupt axial heterojunctions in silicon-germanium nanowires". In: *Science* 326.5957 (2009), pp. 1247–1250.

[240] TM Whitney et al. "Fabrication and magnetic properties of arrays of metallic nanowires". In: *Science* 261.5126 (1993), pp. 1316–1319.

[241] Pieter Rein ten Wolde and Daan Frenkel. "Enhancement of protein crystal nucleation by critical density fluctuations". In: *Science* 277.5334 (1997), pp. 1975–1978.

[242] SA Wolf et al. "Spintronics: a spin-based electronics vision for the future". In: *Science* 294.5546 (2001), pp. 1488–1495.

[243] Yiying Wu and Peidong Yang. "Direct observation of vapor- liquid-solid nanowire growth". In: *Journal of the American Chemical Society* 123.13 (2001), pp. 3165–3166.

[244] Younan Xia et al. "One-dimensional nanostructures: synthesis, characterization, and applications". In: *Advanced materials* 15.5 (2003), pp. 353–389.

[245] Younan Xia et al. "Seed-Mediated Growth of Colloidal Metal Nanocrystals". In: *Angewandte Chemie International Edition* 56.1 (2017), pp. 60–95.

[246] Younan Xia et al. "Shape-controlled synthesis of metal nanocrystals: Simple chemistry meets complex physics?" In: *Angewandte Chemie International Edition* 48.1 (2009), pp. 60–103.

[247] Yujie Xiong and Younan Xia. "Shape-controlled synthesis of metal nanostructures: the case of palladium". In: *Advanced Materials* 19.20 (2007), pp. 3385–3391.

[248] Yujie Xiong et al. "Corrosion-Based Synthesis of Single-Crystal Pd Nanoboxes and Nanocages and Their Surface Plasmon Properties". In: *Angewandte Chemie International Edition* 44.48 (2005), pp. 7913–7917.

[249] Yujie Xiong et al. "Synthesis and characterization of fivefold twinned nanorods and right bipyramids of palladium". In: *Chemical Physics Letters* 440.4-6 (2007), pp. 273–278.

[250] Yujie Xiong et al. "Synthesis and mechanistic study of palladium nanobars and nanorods". In: *Journal of the American Chemical Society* 129.12 (2007), pp. 3665–3675.

[251] Yujie Xiong et al. "Synthesis of palladium icosahedra with twinned structure by blocking oxidative etching with citric acid or citrate ions". In: *Angewandte Chemie* 119.5 (2007), pp. 804–808.

[252] Dan Xu et al. "Solvothermal synthesis of CdS nanowires in a mixed solvent of ethylenediamine and dodecanethiol". In: *The Journal of Physical Chemistry B* 109.30 (2005), pp. 14344–14349.

[253] Jing Xu et al. "Flexible asymmetric supercapacitors based upon Co9S8 nanorod//Co3O4@ RuO2 nanosheet arrays on carbon cloth". In: *ACS nano* 7.6 (2013), pp. 5453–5462.

[254] Wei-Hong Xu et al. "Copper nanowires as nanoscale interconnects: Their stability, electrical transport, and mechanical properties". In: *ACS nano* 9.1 (2014), pp. 241–250.

[255] VA Yablokov et al. "Kinetics of thermal decomposition of sulfur-containing amino acids". In: *Russian Journal of General Chemistry* 79.6 (2009), pp. 1141–1145.

[256] Ruoxue Yan, Daniel Gargas, and Peidong Yang. "Nanowire photonics". In: *Nature photonics* 3.10 (2009), p. 569.

[257] Zai-xing Yang et al. "Surfactant-assisted chemical vapour deposition of high-performance small-diameter GaSb nanowires". In: *Nature communications* 5 (2014), p. 5249.

[258] Yadong Yin et al. "Colloidal synthesis of hollow cobalt sulfide nanocrystals". In: *Advanced Functional Materials* 16.11 (2006), pp. 1389–1399.

[259] Hongjun You et al. "Theoretical description of the role of amine surfactant on the anisotropic growth of gold nanocrystals". In: *CrystEngComm* 18.21 (2016), pp. 3934–3941.

[260] Kui Yu et al. "General low-temperature reaction pathway from precursors to monomers before nucleation of compound semiconductor nanocrystals". In: *Nature communications* 7 (2016), p. 12223.

[261] Kui Yu et al. "Mechanistic study of the role of primary amines in precursor conversions to semiconductor nanocrystals at low temperature". In: *Angewandte Chemie International Edition* 53.27 (2014), pp. 6898–6904.

[262] Clarence Zener. “Interaction between the d shells in the transition metals”. In: *Physical Review* 81.3 (1951), p. 440.

[263] You Zhai and Moonsub Shim. “Effects of Copper Precursor Reactivity on the Shape and Phase of Copper Sulfide Nanocrystals”. In: *Chemistry of Materials* 29.5 (2017), pp. 2390–2397.

[264] Jian-Min Zhang, Fei Ma, and Ke-Wei Xu. “Calculation of the surface energy of FCC metals with modified embedded-atom method”. In: *Applied Surface Science* 229.1-4 (2004), pp. 34–42.

[265] Ming-Liang Zhang et al. “Preparation of large-area uniform silicon nanowires arrays through metal-assisted chemical etching”. In: *The Journal of Physical Chemistry C* 112.12 (2008), pp. 4444–4450.

[266] Yu Zhang et al. “Nanostructured Metal Chalcogenides for Energy Storage and Electrocatalysis”. In: *Advanced Functional Materials* 27.35 (2017).

[267] Yu Zhang et al. “One-Pot Synthesis of Tunable Crystalline Ni3S4@ Amorphous MoS2 Core/Shell Nanospheres for High-Performance Supercapacitors”. In: *Small* 11.30 (2015), pp. 3694–3702.

[268] Nana Zhao et al. “Controlled synthesis of gold nanobelts and nanocombs in aqueous mixed surfactant solutions”. In: *Langmuir* 24.3 (2008), pp. 991–998.

[269] Weijia Zhou et al. “Ni 3 S 2 nanorods/Ni foam composite electrode with low overpotential for electrocatalytic oxygen evolution”. In: *Energy & Environmental Science* 6.10 (2013), pp. 2921–2924.

[270] Yongsheng Zhou et al. “Single-Step Synthesis of Cobalt Sulfide Nanowires Encapsulated in Carbon Nanotubes”. In: *J. Nanosci. Nanotechnol* 13 (2013), pp. 6934–6939.

[271] Zetao Zhu et al. “Rational Concept for Reducing Growth Temperature in Vapor–Liquid–Solid Process of Metal Oxide Nanowires”. In: *Nano letters* 16.12 (2016), pp. 7495–7502.

[272] Ulrich Ziener. “Self-Assembled Nanostructures of Oligopyridine Molecules”. In: *The Journal of Physical Chemistry B* 112.47 (2008), pp. 14698–14717.